NUMERICAL INVESTIGATION OF HIGH KNUDSEN NUMBER FLOW IN RECTANGULAR ENCLOSURES

by

Mehmet Orhan

B.S., M.E., Fırat University, 1992

M.S., M.E., Pamukkale University, 1998

Submitted to the Institute for Graduate Studies in
Science and Engineering in partial fulfillment of
the requirements for the degree of
Doctor of Philosophy

Graduate Program in Mechanical Engineering

Boğaziçi University

2006

NUMERICAL INVESTIGATION OF HIGH KNUDSEN NUMBER FLOW IN RECTANGULAR ENCLOSURES

APPROVED BY:

Assist. Pof. Dr. Ali Ecder (Thesis Supervisor)	.....
Prof. Dr. Akın Tezel (Thesis Co-supervisor)	.....
Assist. Prof. Dr. Kunt Atalık	.....
Assoc. Prof. Dr. Osman Börekçi	.....
Assoc. Prof. Dr. Ali Serpengüzel	.....

DATE OF APPROVAL:

ACKNOWLEDGEMENTS

I acknowledge my gratitude Dr. Ali Ecder, my supervisor, and Dr. Akın Tezel, my co-supervisor, for their encouragements, patience, and helpful advices. I would also like to thank Dr. Kunt Atalık, Dr. Osman Börekçi and Dr. Ali Serpengüzel for their invaluable contributions to this thesis. I'm also so grateful to Mr. Erhan Turan and Mr. Yalın Kaptan for their helps and moral supports.

Special thanks go to my wife Mrs. Nazan Ünsal Orhan and my little son Kaan Orhan for their sacrifices and supports in all stages of the study. I still remember my son's passionate entreaties like "Please do not go to office, please." and "When will your thesis finish ?". After all, it is a great pleasure to write last words of this thesis.

This study is dedicated to Nazan and Kaan
who are the meaning of my life.

ABSTRACT

NUMERICAL INVESTIGATION OF HIGH KNUDSEN NUMBER FLOW IN RECTANGULAR ENCLOSURES

Nowadays, enlightening unknown aspects of rarefied gas flow is one of the critical issues of fluid dynamic research to ensure correct and proper operations of many **M**icro-**E**lectro-**M**echanical-**S**ystems (MEMS). Thermally driven motion of rarefied gases is gaining in importance to develop Knudsen compressors having better performance or to improve single crystal growth processes. Therefore, accurate prediction of the physics lying behind the thermal creep in the transition regime as well as slip flow regime is one of the main motivations of this study. The other emphasis is possible flow instability of the rarefied gases in enclosures. For this purpose, an asymptotic approximation has been performed in the first part of the study to find analytical solutions. In the second one, linear disturbance theory of hydrodynamic stability has been applied to the problem to determine bounds of instabilities. Analytical solutions of two-dimensional stability analysis have been introduced. Critical states have been identified for different models and for varying Knudsen numbers. More generally, eigen-spectrum of the perturbation equations has been identified in three-dimensions. At the last part, by applications of an artificial viscosity scheme, a computer program has been constructed to solve Burnett and also Navier-Stokes equations. Mechanisms of the thermal creep flow have also been verified by inspecting stress tensors of Burnett equations. Most importantly, the insufficiency and the failure of Navier-Stokes equations for the creeping flows have been proved. Moreover, it has been shown that Burnett equations can correctly model such creeping flows.

ÖZET

DİKDÖRTGENSEL KAPALI HACİMLERDE YÜKSEK KNUDSEN SAYI AKIMININ SAYISAL İNCELEMESİ

Son zamanlarda, birçok Mikro Elektro Mekanik Sistemin (MEMS) doğru ve güvenilir çalışabilmesi amacıyla düşük yoğunluklu gazların bilinmeyen yönleri akışkanlar mekaniğinin önemli araştırma konularından biri haline gelmiştir. Termal terleme tahrikli düşük yoğunluklu gazların akışıhem daha iyi performanslı Knudsen kompresörlerinin geliştirilmesinde hem de tek kristal üretiminin geliştirilmesinde oldukça önem kazanmaktadır. Belirtilen nedenlerle; bu çalışmanın amacı, hem kayma hem de geçiş rejimlerinde termal terleme akışlarının altında yatan temel fiziğin anlaşılmasıdır. Diğer bir hedef ise; düşük yoğunluklu gazların kapalıgeometrilerde muhtemel kararsızlıklarının incelenmesidir. Bu tez çalışmasının ilk bölümünde; kapalı geometrilerdeki termal terleme akışlarına ait analitik çözümler asimptotik analiz yardımıyla elde edilmiş ve sunulmuştur. İkinci bölümde ise; lineer kararlılık teorisi önerilen probleme uygulanarak karasızlıkların sınırlarıtesbit edilmeye çalışılmıştır. İki boyutlu stabilite analizine ait analitik çözümler de sunulmuş olup; karasızlığın oluştugu haller, degişen kayma modelleri ve Knudsen sayılarına bağlı olarak belirlenmiştir. Daha da genelde, üç boyutlu pertürbasyon denklemlerinin öz değer spektrumu incelenmiştir. Son bölümde ise; bir yapay viskozite algoritması kullanılarak, Burnett ve Navier-Stokes denklemlerinin benzeşimlerini gerçekleştirebilen bir bilgisayar programı oluşturulmuştur. Aynı zamanda; termal terleme akışının temel mekanizması Burnett denklemi gerilme tensorleri incelenerek açıklanmıştır. Daha önemlisi; Navier-Stokes denklemlerinin bu tip akışlar için yetersizliği ve Burnett denklemlerinin termal terleme akışlarını doğru modelleyebileceği gösterilmiştir.

TABLE OF CONTENTS

LIST OF FIGURES

LIST OF TABLES

LIST OF SYMBOLS/ABBREVIATIONS

$\mathfrak{A}$	Amplitudes of characteristic waves
A_1, A_2	First and second coefficients of the slip models
A_m^i	Surface vector normal to m^{th} face of i^{th} cell $i = e, w, n, s$
b	Constant temperature gradient applied on horizontal walls
$\bar{C}$	Average velocity of an molecule
$\tilde{c}$	Artificial speed of sound
c_{p0}	Constant pressure specific heat evaluated at temperature T_0
c_p	Constant pressure specific heat capacity of a gas
c_R	Phase speed of disturbance waves
d	Diameter of a molecule in Chapter 1, height of an enclosure in the rest of the thesis
D	Differential operator, $\frac{d}{dy}$
$\mathbf{D}$	Artificial diffusion vector
dA	Infinitesimally small area element on the surface of a control volume
E	Total energy of a gas
e	Internal energy of a gas
E_i	Total energy of incoming molecules
E_r	Total energy of reflected molecules
E_w	Total energy of molecules at wall temperature
Ec	Eckert number
$\mathbf{f}$	Body force vector
F_c	Vector of convective fluxes
F_v	Vector of diffusive fluxes
Fr	Froude number
H	Hilbert space
$\Im$	Imaginary part of a complex number/function
k	Coefficient of heat conduction
K	Time rate change of mean energy of perturbations

k_x, k_y, k_z	Wave numbers in x, y, z directions
$(k_z)_{cr}$	Critical wave number in z direction
Kn	Knudsen number, ratio of mean free path λ to characteristic length scale of a flow geometry
Kn_d	Knudsen number based on half channel height, $d/2$
l	Length of an enclosure
m	Molecular weight of a gas
Ma	Mach number u/c where c is the speed of sound
$\tilde{Ma}$	Artificial Mach number
n	Number of molecules in a per unit volume of a gas
$\mathbf{n}, \mathbf{t}$	Surface unit normal and tangent vectors
p	Thermodynamic pressure of a fluid
p'	Pressure disturbances
p'_0	Pressure disturbances in normal mode form
Pr	Prandtl number, $c_p\mu/k$
$\dot{q}$	Heat production rate in a per unit volume of a gas
$\mathbf{q}$	Heat conduction vector
$\mathbf{q}^{(0)}, \mathbf{q}^{(1)}, \mathbf{q}^{(2)}, \mathbf{q}^{(3)}$	Euler, Navier-Stokes, Burnett and Super-Burnett orders of heat conduction vector
R	Gas constant
$\mathbf{R}$	Residual vector of conservative variables
$\mathbf{r}$	Position vector
$\Re$	Real part of a complex number/fuction
$\mathbf{R}_i$	Initial residual vector of conservative variables
r_T	Overheat ratio, $\frac{\Delta T}{T_0}$
Re	Reynolds number
Re_d	Reynolds number based on half channel height, $d/2$
$(Re_d)_{cr}$	Critical Reynolds number
$\mathbf{S}$	Vector of source terms
s	Properties evaluated on a control surface just over a wall
t	Time

T	Temperature
T_{bottom}	Bottom wall temperature
T_{top}	Top wall temperature
T_0	Mean temperature $T_0 = (T_h + T_c)/2$
T_c, T_h	Temperatures of left and right side walls, $T_h > T_c$
T_g	Real temperature of molecules
T_i	Temperature of incoming molecules
T_k	Extrapolated gas temperature
T_r	Temperature of reflected molecules
T_s	Temperature of gas on a wall
T_w	Wall temperature
tr	Transpose of a matrix
$\mathbf{u}$	Velocity vector
u, v, w	Components of a velocity vector in cartesian coordinates, $\mathbf{u} = u\mathbf{e_x} + v\mathbf{e_y} + w\mathbf{e_z}$
$\mathbf{u}'$	Vector of velocity disturbances
u_λ	Velocity of a gas one mean free path away from a wall
u_0	Reference velocity calculated from the thermal creep velocity
$\mathbf{u_0'}$	Vector of velocity disturbances in normal mode form
u_c	Creep velocity
u_t	Velocity component of the velocity vector tangential to a wall
u_w	Wall velocity
$\bar{\mathbf{u}}$	Basic flow velocity vector
V_{max}	Maximum velocity in the flow domain
$\mathbf{W}$	Vector of conservative variables
α	Horizontal coordinate axis used in asymptotic approach for the right section
α_i	Coefficients appeared in second- and third-order stress tensors of Burnett equations, $i = 1 \cdots 17$
β	Vertical coordinate axis used in asymptotic approach for the right section

β_i	coefficients appeared in second- and third-order stress tensors of Burnett equations, $i = 1 \cdots 8$
δ	Artificial compressibility factor
Δ	Small length parameter used for coordinate transformation
Δt	Time step
ΔT	Temperature difference
ϵ	Aspect ratio
$\epsilon^{(2)}$	Coefficient of second order artificial diffusion in JST scheme
$\epsilon^{(4)}$	Coefficient of fourth order artificial diffusion in JST scheme
$\mathbf{\Phi}$	Vector of flow disturbance variables in normal mode form
γ	Ratio of specific heats, c_p/c_v
γ_i	Coefficients appeared in second- and third-order stress tensors of Burnett equations, $i = 1 \cdots 13$
η	Vertical coordinate axis used in asymptotic approach for the left section
λ	Mean free path
λ_i	Characteristic wave velocities, $i = 1 \cdots 5$
μ	Dynamic viscosity
μ_r	Reference dynamic viscosity for Power-Law viscosity model
ν	Complex frequency of the oscillations with respect to thermal-diffusion time scale, $\nu = Re_d Kn_d \sigma$
θ	Dimensionless temperature
θ'	Temperature disturbances
$\theta_0^o, \theta_1^o, \theta_2^o$	Zeroth, first and third order outer approximations to temperature
$\theta_0^i, \theta_1^i, \theta_2^i$	Zeroth, first and third order inner approximations to temperature
θ_0'	Temperature disturbances in normal mode form
ρ	Density
ρ_0	Density evaluated at mean temperature, T_0
σ	Complex eigenvalue

σ_v	Momentum accommodation coefficient
σ_T	Energy accommodation coefficient
$\boldsymbol{\tau}^{(0)}\boldsymbol{\tau}^{(1)}, \boldsymbol{\tau}^{(2)}, \boldsymbol{\tau}^{(3)}$	Euler, Navier-Stokes, Burnett and Super-Burnett orders of stress tensor
Υ	Thermo-physical variables
ω	Relaxation parameter
Ω	Volume of an control volume
$\partial\Omega$	Surface area of an control volume
ξ	Horizontal coordinate axis used in asymptotic approach for the left section
Ψ	Stream function
Ψ_0^o, Ψ_1^o	Zeroth and first orders of outer approximations to stream function
$\tilde{\Psi}_0^i, \tilde{\Psi}_1^i$	Zeroth and first orders of inner approximations to stream function

BC	Boundary condition
BVP	Boundary Value Problem
CVD	Chemical Vapor Deposition
DSMC	Direct Simulation Monte Carlo
GEP	Generalized Eigenvalue Problem
IVP	Initial Value Problem
MEMS	Micro Electro Mechanical Systems
NS	Navier-Stokes equations

1. INTRODUCTION

Nowadays, there is a tremendously increasing interest in rarefied flows of gases due to rapid progress in Micro-Electro-Mechanical Systems (MEMS). Better understanding of operation and performance of many micro-devices requires a closer look into flow of liquids and gases inside/over them. Thermo-molecular compressors (Hobson *et al.*, 2000), hydrodynamic and hydrostatic air thrust bearings in micro-turbines (Elrich *et al.*, 2003), gas damping in surface-micro-machined inertial sensors and resonating filter structures (Veijola *et al.*, 2001), squeeze film damping in MEMS torsion mirror (Pan *et al.*, 1998) and micro propulsion systems including micro-nozzles (Ayon *et al.*, 2001), and -rockets (Teasdale *et al.*, 2001) are some examples of such devices. Rarefied gas flows are observed not only in minituarized instruments but also in macroscopic systems in reduced pressures i.e. evacuated devices and in atmospheric entry problem of space shuttles. Since, better design, operation and functionality of many micro-machines and macroscopic devices necessitate to predict behavior of gases under consideration, it is important to explore and demonstrate the physics of rarefied flow inside them.

A gas becomes rarefied when its density is beyond the continuum limit. In other words, unless density and the other local variables such as velocity, temperature and pressure of the gas can be expressed as continuous functions then the gas would be rarefied. Mean free path is defined as the average distance that a molecule travels between successive collisions. Let's assume that a gas composes of hard spheres with diameters of d. When molecule p comes into contact with another molecule, the distance between the centers of these two molecules creates a volume so called *sphere of influence* (Figure 1.1). If molecule p has an average velocity of $\bar{C}$, then volume of $\pi d^2 \bar{C} n$ is swept by molecule p in a per unit time, where n designates number of molecules in per unit volume of the gas (see Figure 1.2). Note that $\pi d^2 \bar{C} n$ also corresponds to number of collisions in a per unit time. Since the distance traveled by the molecule p in a per unit time is $\bar{C}$, then the average distance traveled per collision is calculated as $\lambda = \bar{C}/\pi d^2 \bar{C} n = 1/\pi d^2 n$. This expression can be written in terms of physical properties of the gas: $\lambda = m/\sqrt{2}\pi d^2 \rho$, where m and ρ corresponds to

molecular weight and density of the gas, respectively (Vincenti, 1965). Ratio of mean free path λ to characteristic length scale of the flow geometry is known as Knudsen number (Kn) which is a measure of rarefaction[1] effects. It is possible to initialize

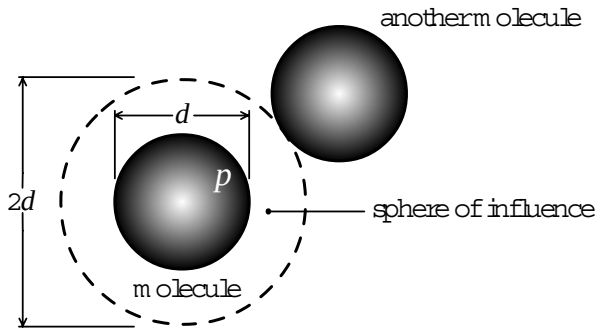

Figure 1.1. An illustration of molecular collision and sphere of influence

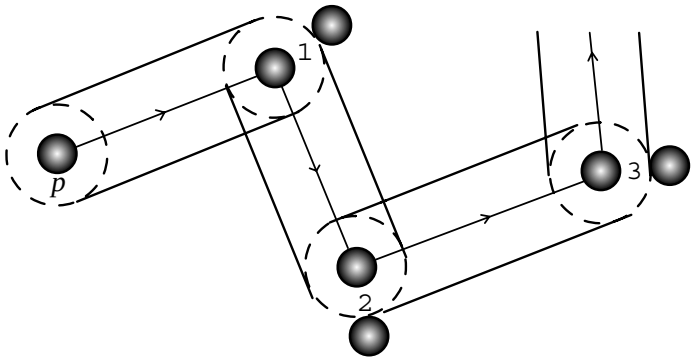

Figure 1.2. A path created by actual collisions of molecule p

rarefied gas flows due to tangential temperature gradient along walls of a channel or an enclosure, where the fluid starts to move slowly in the direction from cold towards hot. This phenomenon is known as "thermal creep" or "transpiration" of the rarefied gas (Karniadakis *et al.*, 2002). Thermally driven movement of rarefied gases leads to

[1]Physics of a gas flow greatly affected by rarefaction degree depending on the Kn number (Figure 1.3).

- If the gas is a continuous media, then continuum flow takes place for $Kn \leq 0.01$. In this case, the molecules of the continuous fluid stick boundary walls.
- For $Kn \geq 10$ flow of a gas becomes completely random and can not be predicted by continuum models.

In a certain levels of rarefaction, a fluid is considered neither continuous nor free molecular. This region is divided into two sub-flow regimes.

- Slip flow regime ($0.01 \leq Kn \leq 0.1$) in which the gas molecules slip on the wall surface: in this regime models of the continuum hydromechanics can still be used with slip boundary conditions rather than no-slip.
- Transition flow regime ($0.1 < Kn < 10$): either molecular models or higher-order descriptions of continuum hydrodynamics are required for modeling the gas flow (Gad-el-Hak, 1999).

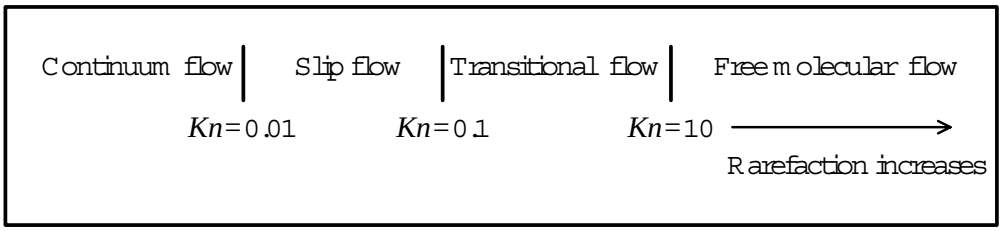

Figure 1.3. Flow regimes as a result of rarefaction effects

a number of technological and scientific interests. Among them, Knudsen compressors with the throughput to atmospheric levels have outstanding features due to absence of non-moving parts (Hobson *et al.*, 2000). Vargo *et al.* (1999) have been performed comprehensive Knudsen compressor experiments in both micro and macro scales. Several compressor characteristics such as pressure rise, pumping volume, energy use and mass flow of both scales have been presented. In addition to Knudsen compressors, suitable operation of Capacitance Diaphragm Gauge transducers and capacitance manometers require better understanding of thermal transpiration at low pressures (Setina, 1999). Another important field of interest is physical vapor crystal growth in reduced pressures. The presence of non-uniform temperature distribution along the walls bounding vapor crystal can lead to convective motion under micro-gravity conditions as reported by (Papadopoulos *et al.*, 1995). They have performed **D**irect **S**imulation **M**onte **C**arlo (DSMC) simulations for Kn about 0.075 in a unit square geometry. They have stressed that observed cellular patterns are created only due to thermal transpiration although buoyancy forces are negligible. The role of rarefied gas transport and profile evolution in non-planar substrate Chemical Vapor Deposition (CVD) is examined by Coronell *et al.* (1994). Use of DSMC method was enabled them the prediction of the profile of deposited film for $0.1 \leq Kn \leq 1$. Unfortunately, thermal gradients are presumed to be negligible in this theoretical investigation. An initiative study about the deposition profile characteristics in semiconductor manufacturing processes has been conducted by Ikegawa *et al.* (1989). They have simulated sputter deposition, plasma CVD and thermal CVD methods with different rarefaction levels. Nevertheless, the effect of variable substrate temperature has not been considered in this study.

Operation of vapor deposition and crystal growth processes in low pressures or small length scales requires better understanding of physics lying behind the flows of rarefied gases as mentioned above. Presence of temperature gradient generates thermal transpiration which may be important for the quality and operation of such systems. Besides technological interests, unresolved issues of the thermally driven rarefied gas have also scientific interest. The main motivation of this study is thermally driven flows of rarefied gases in closed geometries and its possible flow instabilities.

Velocity slip is generated by two significant physical phenomena: due to accommodation of momentum and thermal transpiration in rarefied gases. Moreover, a temperature jump occurs in the gas by accommodation of thermal energy as discussed in Section 2.2.3.

2. GOVERNING EQUATIONS AND BOUNDARY CONDITIONS

Before proceeding with the derivation of slip boundary and temperature jump boundary conditions, Burnett and Navier-Stokes (NS) models will be introduced.

2.1. Governing Equations

Flow of moderately rarefied gases requires high-order description of kinetic theory of gases. One of the high-order approximation of the hydrodynamic flow theory is known as Burnett Equations resulting from power series (Chapman-Enskog expansion) solution of the Boltzmann transport equation. Derivation of Burnett equations and the other details about theory can be found in Chapman *et al.* (1970) and pages 385-394 of Vincenti (1965). In this study, augmented Burnett equations are employed and more information about the mathematical model can be found in Aqarwal *et al.* (2001).
Let's consider a control volume shown in Figure 2.1. Integral form of governing equations can be written
for conservation of mass,

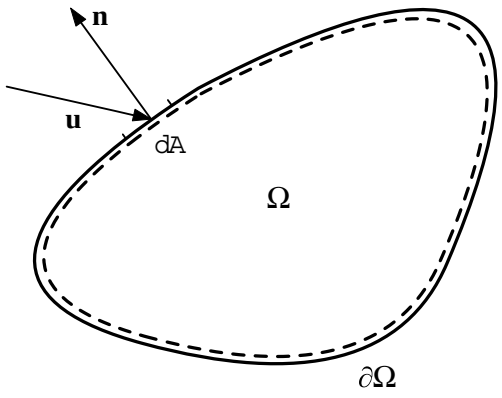

Figure 2.1. Control volume of the flow domain.

$$\frac{\partial}{\partial t}\int_{\Omega}\rho\, d\Omega + \oint_{\partial\Omega}\rho\,(\mathbf{u}\cdot\mathbf{n})\; dA, \tag{2.1}$$

for conservation of momentum,

$$\frac{\partial}{\partial t}\int_{\Omega}\rho\mathbf{u}\,d\Omega+\oint_{\partial\Omega}\rho\mathbf{u}\left(\mathbf{u}\cdot\mathbf{n}\right)\,dA=\int_{\Omega}\rho\mathbf{f}\,d\Omega$$
$$-\oint_{\partial\Omega}p\mathbf{n}\,dA+\oint_{\partial\Omega}\left(\boldsymbol{\tau}\cdot\mathbf{n}\right)\,dA \tag{2.2}$$

and for conservation of energy

$$\frac{\partial}{\partial t}\int_{\Omega}\rho E\,d\Omega+\oint_{\partial\Omega}\rho E\left(\mathbf{u}\cdot\mathbf{n}\right)\,dA=\oint_{\partial\Omega}\mathbf{q}\cdot\mathbf{n}\,dA$$
$$+\int_{\Omega}\left(\rho\mathbf{f}\cdot\mathbf{u}+\dot{q}\right)\,d\Omega-\oint_{\partial\Omega}p\left(\mathbf{u}\cdot\mathbf{n}\right)\,dA+\oint_{\partial\Omega}\left(\boldsymbol{\tau}\cdot\mathbf{u}\right)\cdot\mathbf{n}\,dA \tag{2.3}$$

$$\boldsymbol{\tau}=\boldsymbol{\tau}^{(0)}+\boldsymbol{\tau}^{(1)}+\boldsymbol{\tau}^{(2)}+\boldsymbol{\tau}^{(3)},$$

$$\mathbf{q}=\mathbf{q}^{(0)}+\mathbf{q}^{(1)}+\mathbf{q}^{(2)}+\mathbf{q}^{(3)},$$

$$E=e+\frac{\mathbf{u}\cdot\mathbf{u}}{2},$$

where superscripts 0, 1, 2 and 3 represent orders of Chapman-Enskog expansion of Boltzmann equation. More information about constitutive relations and heat flux vectors of each order are given in (Aqarwal *et al.*, 2001). The Relationship between the pressure and density can be expressed via equation of state;

$$p=\rho RT \tag{2.4}$$

Integral conservation laws can be written in a more compact form by introducing a vector of conservative variables, convective fluxes and diffusive fluxes. In cartesian coordinate system, integral form of conservation laws can be expressed in a compact

form as

$$\frac{\partial}{\partial t}\int_{\Omega}\mathbf{W}\,d\Omega+\oint_{\partial\Omega}\left(\mathbf{F}_c-\mathbf{F}_v\right)\,dA=\int_{\Omega}\mathbf{S}\,d\Omega. \tag{2.5}$$

The vector of conserved quantities is written as

$$\mathbf{W}=\begin{bmatrix}\rho\\ \rho u\\ \rho v\\ \rho w\\ \rho E\end{bmatrix} \tag{2.6}$$

Convective and diffusive flux vectors balancing the time rate the change of the conservative variables can be written for convective fluxes

$$\mathbf{F}_c=\begin{bmatrix}\rho u_n\\ \rho u u_n\\ \rho v u_n\\ \rho w u_n\\ \rho E u_n\end{bmatrix}, \tag{2.7}$$

with

$$u_n=\mathbf{u}\cdot\mathbf{n}=un_x+vn_y+wn_z \tag{2.8}$$

and diffusive fluxes

$$\mathbf{F}_v=\begin{bmatrix}0\\ n_x(\tau_{xx}-p)+n_y\tau_{xy}+n_z\tau_{xz}\\ n_x\tau_{yx}+n_y(\tau_{yy}-p)+n_z\tau_{yz}\\ n_x\tau_{zx}+n_y\tau_{zy}+n_z(\tau_{zz}-p)\\ (n_x\Phi_x-q_xn_x)+(n_y\Phi_y-q_yn_y)+(n_z\Phi_z-q_zn_z)\end{bmatrix}, \tag{2.9}$$

where

$$\Phi_x = -up + u\tau_{xx} + v\tau_{xy} + w\tau_{xz}, \tag{2.10}$$

$$\Phi_y = -vp + u\tau_{yx} + v\tau_{yy} + w\tau_{yz}, \tag{2.11}$$

and

$$\Phi_z = -wp + u\tau_{zx} + v\tau_{zy} + w\tau_{zz} \tag{2.12}$$

compose of work done on the control volume by pressure and viscous stresses. The source term $\mathbf{S}$ includes effects of all forces acting on the fluid and heat production rate in a per unit volume

$$\mathbf{S} = \begin{bmatrix} 0 \\ \rho f_x \\ \rho f_y \\ \rho f_z \\ \rho \left(f_x u + f_y v + f_z w \right) + \dot{q} \end{bmatrix}. \tag{2.13}$$

Viscosity and thermal conductivity approximations of kinetic theory have been well developed and two excellent literatures introduce the derivations and comprehensive details of them (Chapman *et al.*, 1970; Present, 1958). However, application of viscosity and coefficient of thermal conductivity formulas given in these texts is not simple and computationally inefficient. For routine calculations, simpler approximations of viscosity and thermal conductivity are preferred. One of them is Power Law approximation of viscosity which can be read as

$$\frac{\mu}{\mu_r} \approx \left(\frac{T}{T_r} \right)^n \tag{2.14}$$

where n is approximately equal to 0.70 for air and parameters T_r and μ_r are reference

values which are found in White (2005).

Power law which has been derived for viscosity, can also be used for coefficient of thermal conductivity. However, in most cases, Pr number is taken as constant in the whole flow domain. Therefore, thermal conductivity of fluid is computed generally by the following approximation

$$k = \frac{c_p \mu}{Pr}, \tag{2.15}$$

where c_p is specific heat constant. In this study, power law viscosity and constant Pr number model for the coefficient of heat conduction, Equations 2.14 and 2.15 are used in direct simulation of Burnett equations.

2.2. Boundary Conditions

2.2.1. Velocity Slip Due To Momentum Accommodation

The basic and simplest form of the velocity slip was derived by Maxwell (1878).

$$u_t|_s - u_w = \frac{2 - \sigma_v}{\sigma_v} \frac{1}{\rho_s \sqrt{2RT_s/\pi}} \tau_s$$

where τ, ρ, T and R are wall shear stress, density, temperature and gas constant respectively. Here, subscript s denotes quantities evaluated on the wall surface. Additionally, t represent the tangential directions to the wall. σ_v is a coefficient expressing tangential momentum accommodation of the gas and it is a measure of momentum exchange of gas molecules with surfaces. Mostly, it is set to unity. More comprehensive details of accommodation coefficients can be found in Karniadakis *et al.* (2002). To ensure more accurate examination of rarefied gas flow in the slip regime, higher order boundary conditions are required. For this reason, a number of higher order boundary conditions have been proposed. One of the second-order accurate (in terms of Kn number) velocity slip boundary condition which is also known as Beskok's second order slip condition, has been derived by Karniadakis *et al.* (2002). As an example, one of the formulations

of this boundary condition will be summarized in the following paragraph.

According to Beskok, accommodation total tangential momentum flux on control surface (cs) leads to slip velocity that can be expressed as a combination of wall velocity and a velocity evaluated one free path away from the solid wall, as illustrated in Figure 2.2.

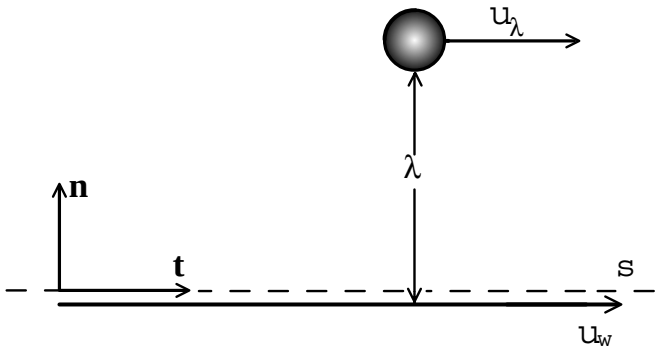

Figure 2.2. Control surface for tangential momentum flux near an isothermal wall moving at velocity of u_w (Karniadakis *et al.*,, 2002)

$$u_t|_s = \frac{1}{2}[u_\lambda + (1-\sigma_v)u_\lambda + \sigma_v u_w]$$

Taylor series expansion of u_λ for small mean free path (λ) can be written as

$$u_t|_s = \frac{1}{2}\left[u_t|_s + \lambda\frac{\partial u_t}{\partial n}\bigg|_s + \frac{\lambda^2}{2}\frac{\partial^2 u_t}{\partial n^2}\bigg|_s + \cdots\right]$$

$$+\frac{1}{2}\left\{(1-\sigma_v)\left[u_t|_s + \lambda\frac{\partial u_t}{\partial n}\bigg|_s + \frac{\lambda^2}{2}\frac{\partial^2 u_t}{\partial n^2}\bigg|_s + \cdots\right] + \sigma_v u_w\right\} \tag{2.16}$$

Arrangement of this expansion gives the higher order velocity slip boundary condition (truncated at $O(\lambda^3)$) as the following

$$u_t|_s - u_w = \frac{2-\sigma_v}{\sigma_v}\left[\lambda\frac{\partial u_t}{\partial n}\bigg|_s + \frac{\lambda^2}{2}\frac{\partial^2 u_t}{\partial n^2}\bigg|_s\right].$$

Generalized form of the higher-order representation by introducing two important coefficients is widely used in the rarefied gas studies and can be represented as

$$u_t|_s - u_w = \frac{2-\sigma_v}{\sigma_v}\left[A_1\lambda\left.\frac{\partial u_t}{\partial n}\right|_s + A_2\lambda^2\left.\frac{\partial^2 u_t}{\partial n^2}\right|_s\right].$$

These coefficients which are also known as slip coefficients determined by different authors are tabulated in Table 2.1.

Table 2.1. Coefficients for the first and second-order slip models.

(Colin,, 2005)

Investigator	A_1	A_2
Cercignani	1.1466	-0.9756
Deissler	1.0	-9/8
Schamberg	1.0	-5π/12
Hsia and Domoto	1.0	-0.5
Maxwell (Kennard,, 1938)	1.0	0.0
Beskok (Beskok, 2002)	1.0	0.5
Chapman and Cowling (1952)	1.0	0.5
Mitsuya	1.0	-2/9

2.2.2. Velocity Slip Due to Thermal Transpiration

As mentioned in the preceding chapter, movements of rarefied gas molecules is possible unless wall temperature is isothermal. A motion of a rarefied gas due to thermal effects is described as

$$u_t|_s = \frac{3}{4}\frac{Pr(\gamma-1)}{\gamma}\frac{1}{\rho_s R T_s}\left.\frac{\partial T}{\partial t}\right|_s, \tag{2.17}$$

where Pr, μ, γ refers to Prandtl number, dynamic viscosity and ratio of specific heats, c_p/c_v. For the sake of brevity, interested readers are referred to the derivation of thermal transpiration velocity slip formula in pages 327-330 of Kennard (1938).

2.2.3. Temperature Jump Boundary Condition

Analogous to velocity slip due to momentum accommodation, there is a discontinuous region of temperature which should be analyzed for the use of continuum mechanics. Temperature jump[2] due to rarefaction level of the gas is given by

$$T_s - T_w = g \left.\frac{\partial T}{\partial n}\right|_s \quad \text{with} \quad g = \frac{2-\sigma_T}{\sigma_T}\left[\frac{2(\gamma-1)}{\gamma}\right]\frac{k}{\rho_s R(2RT_s/\pi)}$$

where σ_T , γ and k are thermal accommodation coefficient, the ratio of specific heats and thermal conductivity of the gas. Introduction of Pr number and the mean free path leads to the following relation

$$T_s - T_w = \frac{2-\sigma_T}{\sigma_T}\left(\frac{2\gamma}{\gamma+1}\right)\frac{1}{Pr}\left[\lambda \left.\frac{\partial T}{\partial n}\right|_s\right].$$

Karniadakis *et al.*, (2002) noticed a close link between the formulas of velocity slip due to momentum accommodation and temperature jump. Due to similarity of them, second-order accurate temperature BC can be written as;

$$T_s - T_w = \frac{(2-\sigma_T)}{\sigma_T}\left(\frac{2\gamma}{\gamma+1}\right)\frac{1}{Pr}\left[A_1\lambda \left.\frac{\partial T}{\partial n}\right|_s + A_2\lambda^2 \left.\frac{\partial^2 T}{\partial n^2}\right|_s\right].$$

After the introduction of the mechanism lying behind the velocity slip, a final version of velocity slip boundary condition is constructed by combining relevant slip effects i.e. slip due to momentum accommodation and slip due to thermal transpiration.

$$u_s - u_w = \frac{2-\sigma_v}{\sigma_v}\left[A_1\lambda \left.\frac{\partial u}{\partial n}\right|_s + A_2\lambda^2 \left.\frac{\partial^2 u}{\partial n^2}\right|_s\right] + \frac{3}{4}Pr\frac{(\gamma-1)}{\gamma}\frac{1}{\rho_s R T_s}\left.\frac{\partial T}{\partial t}\right|_s \qquad (2.18)$$

[2]Let's assume that a gas is heated by a solid surface (Figure 2.3). In this situation, there will be a discontinuity of temperature just near the wall surface. Such a discontinuity becomes intolerable as rarefaction degree of the gas increases. Therefore, temperature of the gas on the wall surface is found by an extrapolation $T_k - T_w = g\frac{\partial T}{\partial n}$ where T_k and T_w designate extrapolated gas and wall temperatures, respectively. Here, g is a parameter to be determined. For this purpose, consider that there are incident and reflected streams over the wall surface. If the incident stream of molecules carries an energy of E_i and so does reflected molecules E_r, efficiency of energy exchange between the molecular stream and the wall is calculated as $\frac{E_i - E_r}{E_i - E_w} = \sigma_T$ which can also be expressed in terms of the temperatures $\frac{T_i - T_r}{T_i - T_w} = \sigma_T$. The coefficient of accommodation σ_T is measured experimentally in general. Determination of the coefficient g can be found in pages 311-315 of Kennard (1938).

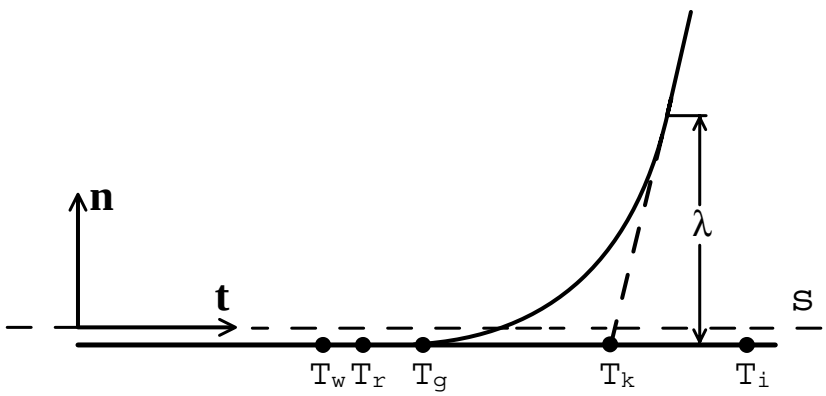

Figure 2.3. Gradient of temperature in a vicinity of wall

Similarly, the higher-order description of temperature jump boundary condition can be written as;

$$T_s - T_w = \frac{2-\sigma_T}{\sigma_T}\left(\frac{2\gamma}{\gamma+1}\right)\frac{1}{Pr}\left[A_1\lambda\frac{\partial T}{\partial n}\bigg|_s + A_2\lambda^2\frac{\partial^2 T}{\partial n^2}\bigg|_s\right]. \tag{2.19}$$

It should be noted that, presence of non-isothermal walls bounding rarefied gas media can initiate a gas movement even absence of any external effect i.e. pressure, body forces. Such an phenomenon which is responsible for the motion of the gas may play an important role beyond the continuum limit ($Kn \geq 0.01$).

3. RAREFIED GAS FLOW IN RECTANGULAR ENCLOSURES: ASYMPTOTIC SOLUTIONS

In this chapter, we will elucidate flow characteristics of rarefied gases in an enclosure. Linear stability analysis of certain kind of flows requires known base flow field in which an instable flow structure initiates; this is the reason why base flow is the point of interest. Asymptotic theory has been used as an analytical tool to analyze many non-linear fluid mechanics problems for a long time. Surface motion due to thermal transpiration is transmitted to core regions by viscous diffusion. An illustrative representation of the possible base flow and the geometrical details of the enclosure are shown in Figure 3.1.

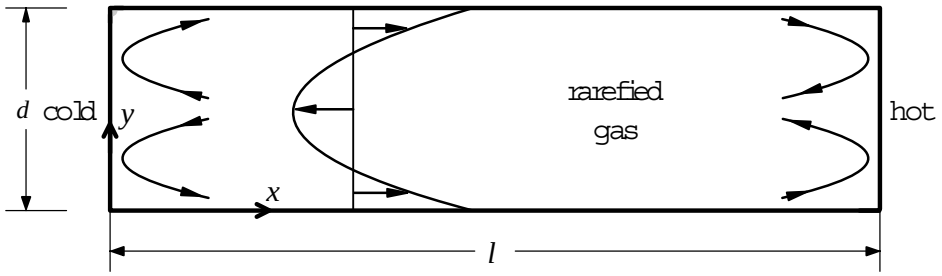

Figure 3.1. Flow of the rarefied gas due to thermal transpiration.

3.1. Definitions and Assumptions

In order to investigate thermally driven flow characteristics of the gas, let's consider an enclosure having depth, d and length l, which is shown in Figure 3.2. The right and left ends are kept at constant temperatures of T_h and T_c where $T_h > T_c$. The upper wall is made of a well conductive material and its temperature varies linearly between T_h and T_c. On the other hand, lower boundary is well insulated so that there is no heat flux across the boundary. The following assumptions have been made for the analysis:

i. steady flow,

ii. incompressible flow,

iii. rarefaction of gas (Kn number is sufficiently high, $0.01 \leq Kn < 1$),

iv. no temperature dependency of thermo-physical properties,

v. Newtonian fluid,

vi. no gravitational or external forces.

Here, incompressibility assumption of the gas should be discussed. For this reason, let's consider Nitrogen gas in the enclosure with $d = 50$ μm and $l = 1$ mm. The gas is subjected to constant horizontal temperature gradient with $T_c = 300$ °K and $T_h = 400$ °K. For $Kn = 0.1$, mean density is calculated as 0.0168 kg/m^3 . In this case, mean slip velocity u_c along the upper surface of the enclosure, as seen in Figure 3.2, can be calculated as;

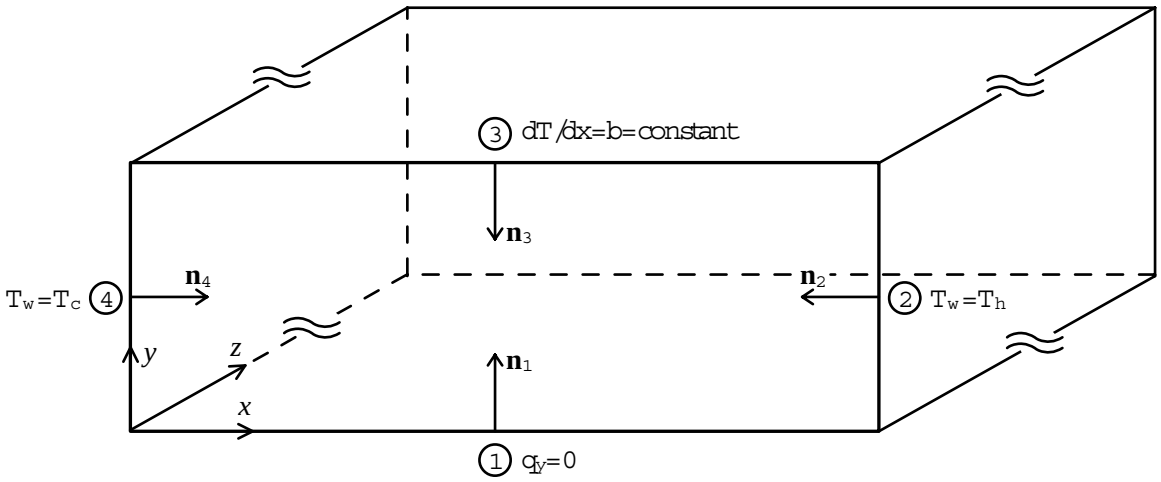

Figure 3.2. An illustrative representation of the three-dimensional enclosure. Width of the enclosure is too large compared with the other dimensions. Therefore, changes of the flow variables in z directions are assumed to be not sharp. While temperatures of the right and left ends at T_h and T_c, respectively, the top wall is subjected to constant temperature gradient and bottom wall is well insulated.

$$u_c = \frac{3}{4}\left(\frac{\gamma-1}{\gamma}\right) Pr \frac{1}{\rho_0 R T_0}\frac{dT}{dx} = \frac{3}{4}\left(\frac{1.4-1}{1.4}\right) 0.768 \frac{1}{1744.536}\frac{400-300}{1\times 10^{-3}} = 9.43 \quad \text{m/s},$$

where subscript "0" denotes properties evaluated at mean temperature. Corresponding Mach number will be;

$$Ma = \frac{9.43}{\sqrt{1.4 \times 296.7 \times 350}} = 0.0247$$

It should be stressed that Ma number computed at the average temperature is very small. Since, Ma number is smaller than 0.3 the flow can be assumed incompressible. In addition to this simple proof, a study reported by Karniadakis *et al.* (2002) supports *incompressibility* assumption. In a Couette flow of rarefied gas analysis of them, while the bottom plate is kept at a temperature of $T_{bottom} = 350$ °K and the upper plate is kept at a temperature $T_{top} = 300$ °K, the validity of incompressibility assumption has been checked. Their results show that significant deviations from incompressible flow are observed for only $Ma_\infty \geq 0.3$ which is calculated at the top plate. Therefore, the proposed flow can be assumed incompressible safely.

3.2. Mathematical Model

Consider an enclosure filled by a rarefied gas of density, ρ_0, dynamic viscosity, μ_0, and thermal conductivity, k_0 which are evaluated at mean temperature, $T_0 = (T_h + T_c)/2$. Equations governing unsteady motion of a rarefied gas, Equations 2.1-2.3, are converted to steady, incompressible Navier-Stokes equations:
continuity,

$$\frac{\partial u}{\partial x} + \frac{\partial v}{\partial y} = 0, \tag{3.1}$$

x-momentum

$$u\frac{\partial u}{\partial x} + v\frac{\partial u}{\partial y} = -\frac{1}{\rho_0}\frac{\partial p}{\partial x} + \frac{\mu_0}{\rho_0}\left[\frac{\partial^2 u}{\partial x^2} + \frac{\partial^2 u}{\partial y^2}\right], \tag{3.2}$$

y-momentum,

$$u\frac{\partial v}{\partial x}+v\frac{\partial v}{\partial y}=-\frac{1}{\rho_0}\frac{\partial p}{\partial y}+\frac{\mu_0}{\rho_0}\left[\frac{\partial^2 v}{\partial x^2}+\frac{\partial^2 v}{\partial y^2}\right], \tag{3.3}$$

and energy equations

$$u\frac{\partial T}{\partial x}+v\frac{\partial T}{\partial y}=\frac{k_0}{\rho_0 c_{p0}}\left[\frac{\partial^2 T}{\partial x^2}+\frac{\partial^2 T}{\partial y^2}\right], \tag{3.4}$$

where p is the thermodynamic pressure of the system. The governing equations form a complete set of the partial differential equations mathematically by introducing appropriate boundary conditions. Boundary conditions of the system Equations 3.1-3.4 given for

the bottom wall;

$$u\left(x,0\right)=\left[A_1\lambda u_y\left(x,0\right)+A_2\lambda^2 u_{yy}\left(x,0\right)\right]+\frac{3}{4}\left(\frac{\gamma-1}{\gamma}\right)\frac{c_{p0}\mu_0}{\rho_0 R T_0}T_x\left(x,0\right), \tag{3.5}$$

$$v\left(x,0\right)=0, \tag{3.6}$$

$$T_y\left(x,0\right)=0, \tag{3.7}$$

for the upper wall;

$$u\left(x,d\right)=\left[-A_1\lambda u_y\left(x,d\right)+A_2\lambda^2 u_{yy}\left(x,d\right)\right]+\frac{3}{4}\left(\frac{\gamma-1}{\gamma}\right)\frac{c_{p0}\mu_0}{\rho_0 R T_0}T_x\left(x,d\right), \tag{3.8}$$

$$v\left(x,d\right)=0, \tag{3.9}$$

$$T\left(x,d\right)=T_{w3}+\left(\frac{2\gamma}{\gamma+1}\right)\frac{k_0}{c_{p0}\mu_0}\left[-A_1\lambda T_y\left(x,d\right)+A_2\lambda^2 T_{yy}\left(x,d\right)\right], \tag{3.10}$$

for the left wall;

$$u\left(0,y\right)=0 \tag{3.11}$$

$$v\left(0,y\right)=\left[A_1\lambda v_x\left(0,y\right)+A_2\lambda^2 v_{xx}\left(0,y\right)\right]+\frac{3}{4}\left(\frac{\gamma-1}{\gamma}\right)\frac{c_{p0}\mu_0}{\rho_0 RT_0}T_y\left(0,y\right) \tag{3.12}$$

$$T\left(0,y\right)=T_{w4}+\left(\frac{2\gamma}{\gamma+1}\right)\frac{k_0}{c_{p0}\mu_0}\left[A_1\lambda T_x\left(0,y\right)+A_2\lambda^2 T_{xx}\left(0,y\right)\right] \tag{3.13}$$

and finally for the right wall;

$$u\left(l,y\right)=0 \tag{3.14}$$

$$v\left(l,y\right)=\left[-A_1\lambda v_x\left(l,y\right)+A_2\lambda^2 v_{xx}\left(l,y\right)\right]+\frac{3}{4}\left(\frac{\gamma-1}{\gamma}\right)\frac{c_{p0}\mu_0}{\rho_0 RT_0}T_y\left(l,y\right) \tag{3.15}$$

$$T\left(l,y\right)=T_{w2}+\left(\frac{2\gamma}{\gamma+1}\right)\frac{k_0}{c_{p0}\mu_0}\left[-A_1\lambda T_x\left(l,y\right)+A_2\lambda^2 T_{xx}\left(l,y\right)\right]. \tag{3.16}$$

Since the temperature jump BCs necessitate wall temperatures, their values are designated as w2, w3 and w4 which are right, top and left walls, respectively. Application of general velocity slip and temperature jump BCs require to account surface normals of each surface as illustrated in Figure 3.2. Thermal transpiration effects are neglected on the left and right side walls due to isothermal wall temperatures.

Some problems of fluid mechanics include a small/large physical parameter which is called *perturbation parameter* in the terminology of asymptotic theory. For example, Re number is very small, $Re \ll 1$, in cases of Stokes and Oseen flows. On the other hand, Re number is high enough, $Re \gg 1$, in some cases of boundary layer flows. In addition to these physical perturbation parameters, *coordinate perturbation*

parameters become effective in flow geometries in which one of the dimensions is much greater than the others. An approximation to these type of problems gets better as the perturbation parameter goes to zero or infinity. It is possible to construct an accurate solution by taking basic solution as the first step and adding successive approximations to the basic solution. In fact, series of basic and successive approximations are known as *asymptotic expansion*. Generally, perturbation expansion converges successfully to reasonable solutions. This types of expansions are called as *regular perturbation*. However, in some cases, asymptotic expansion series are not valid in whole domain and do not convect the correct physics. Therefore, *singular perturbation* techniques should be introduced to find a global solution valid in the entire domain. In most cases, a perturbation solution is uniformly valid in the space and time coordinates unless the perturbation parameter ϵ is the ratio of two dimensions (Van Dyke,, 1964). This study considers ratio of height d to l as the perturbation parameter. The complete picture will become clear in the next paragraphs.

Governing equations of motion are non-dimensionalized by use of the following appropriate scales

$$x^* = \frac{x}{l}, \quad y^* = \frac{y}{d}, \quad \epsilon = \frac{d}{l},$$

$$u^* = \frac{u}{u_0}, \quad v^* = \frac{v}{\epsilon u_0}, \quad \theta = \frac{T - T_c}{T_h - T_c}, \quad p^* = \frac{p}{\mu_0 u_0 l/d^2}$$

where ϵ is the perturbation parameter representing the aspect ratio of the enclosure. Note that properties denoted by subscript "0" are defined at mean temperature T_0. Reference velocity, u_0, represents mean thermal creep velocity acquired on the top wall and derived from Equation 2.17,

$$u_c = \frac{3}{4}\left(\frac{\gamma - 1}{\gamma}\right) c_{p0}\mu_0 \frac{1}{\rho_0 R T_0}\frac{\partial T}{\partial x}\bigg|_s = Kn^2 \frac{3}{2\pi}\left(\frac{\gamma - 1}{\gamma}\right)\frac{c_{p0}\rho_0}{\mu_0} d^2 \frac{\partial T}{\partial x}\bigg|_s,$$

where Kn number is given as

$$Kn = \frac{\mu_0}{\rho_0 d\sqrt{2RT_0/\pi}}. \tag{3.17}$$

Since the enclosure is subjected to constant temperature gradient along the x-direction, reference velocity can be estimated from

$$u_0 = \frac{3}{2\pi}\left(\frac{\gamma-1}{\gamma}\right)\frac{c_{p0}\rho_0{\mu_0}^2}{d}\left.\frac{\partial T}{\partial x}\right|_s = \frac{3}{2\pi}\left(\frac{\gamma-1}{\gamma}\right)\frac{c_{p0}\rho_0}{\mu_0}d^2\frac{\Delta T}{l}, \tag{3.18}$$

where $\Delta T = T_h - T_c$ expresses temperature difference between the hot and cold walls. Employing the scales mentioned, dimensionless NS equations take such forms;
for mass conservation,

$$\frac{\partial u}{\partial x} + \frac{\partial v}{\partial y} = 0, \tag{3.19}$$

conservation of momentum,

$$\epsilon Re\left[u\frac{\partial u}{\partial x} + v\frac{\partial u}{\partial y}\right] = -\frac{\partial p}{\partial x} + \epsilon^2\frac{\partial^2 u}{\partial x^2} + \frac{\partial^2 u}{\partial y^2}, \tag{3.20}$$

$$\epsilon^3 Re\left[u\frac{\partial v}{\partial x} + v\frac{\partial v}{\partial y}\right] = -\frac{\partial p}{\partial y} + \epsilon^4\frac{\partial^2 v}{\partial x^2} + \epsilon^2\frac{\partial^2 u}{\partial y^2}, \tag{3.21}$$

and conservation of energy equation

$$\epsilon\ RePr\left[u\frac{\partial \theta}{\partial x} + v\frac{\partial \theta}{\partial y}\right] = \epsilon^2\frac{\partial^2 \theta}{\partial x^2} + \frac{\partial^2 \theta}{\partial y^2}. \tag{3.22}$$

Here, Re and Pr non-dimensional numbers which are given by

$$Re = \frac{\rho_0 u_0 d}{\mu_0} = \epsilon\frac{3}{2\pi}\left(\frac{\gamma-1}{\gamma}\right)\frac{\rho_0^2 d^2 c_{p0}\Delta T}{\mu_0^2}, \quad Pr = \frac{c_{p0}\mu_0}{k_0}, \tag{3.23}$$

respectively. Non-dimensional slip velocity and temperature jump relations are rearranged in the following forms

on the bottom wall;

$$u\left(x,0\right)=\left[A_1Knu_y\left(x,0\right)+A_2Kn^2u_{yy}\left(x,0\right)\right]+Kn^2\theta_x\left(x,0\right), \tag{3.24}$$

$$v\left(x,0\right)=0, \tag{3.25}$$

$$\theta_y\left(x,0\right)=0, \tag{3.26}$$

on the top wall;

$$u\left(x,1\right)=\left[-A_1Knu_y\left(x,1\right)+A_2Kn^2u_{yy}\left(x,1\right)\right]+Kn^2\theta_x\left(x,1\right), \tag{3.27}$$

$$v\left(x,1\right)=0, \tag{3.28}$$

$$\theta\left(x,1\right)=\theta_{w3}+\left(\frac{2\gamma}{\gamma+1}\right)\frac{1}{Pr}\left[-A_1Kn\theta_y\left(x,1\right)+A_2Kn^2\theta_{yy}\left(x,1\right)\right], \tag{3.29}$$

on the left wall;

$$u\left(0,y\right)=0, \tag{3.30}$$

$$v\left(0,y\right)=\left[A_1Knv_x\left(0,y\right)+A_2Kn^2v_{xx}\left(0,y\right)\right], \tag{3.31}$$

$$\theta\left(0,y\right)=\theta_{w4}+\left(\frac{2\gamma}{\gamma+1}\right)\frac{1}{Pr}\left[A_1Kn\theta_x\left(0,y\right)+A_2Kn^2\theta_{xx}\left(0,y\right)\right] \tag{3.32}$$

and on the right one;

$$u\left(1,y\right)=0, \tag{3.33}$$

$$v\left(1,y\right)=\left[-A_1Knv_x\left(1,y\right)+A_2Kn^2v_{xx}\left(1,y\right)\right] \tag{3.34}$$

$$\theta\left(1,y\right)=\theta_{w2}+\left(\frac{2\gamma}{\gamma+1}\right)\frac{1}{Pr}\left[-A_1Kn\theta_x\left(1,y\right)+A_2Kn^2\theta_{xx}\left(1,y\right)\right]. \tag{3.35}$$

To take advantage of studying with only one dependent variable in governing equations 3.19-3.22 and its BCs, introduction of stream function Ψ formulation may be useful. As is well known, relationship between x-y velocity components and stream function can be written in the following form:

$$u=\frac{\partial\Psi}{\partial y},\quad v=-\frac{\partial\Psi}{\partial x}.$$

Thus, stream function formulation and the energy equation are read as

$$\epsilon Re\left[\Psi_y\Psi_{xyy}-\Psi_x\Psi_{yyy}\right]-\epsilon^3Re\left[\Psi_x\Psi_{xxy}-\Psi_x\Psi_{xxx}\right]=2\epsilon^2\Psi_{yyxx}+\Psi_{yyyy}+\epsilon^4\Psi_{xxxx} \tag{3.36}$$

$$\epsilon RePr\left[\Psi_y\theta_x-\Psi_x\theta_y\right]=\epsilon^2\theta_{xx}+\theta_{yy}. \tag{3.37}$$

It should be noted that subscripts in the formulation designate partial derivatives with respect to spatial coordinates. Substitution of velocity components in terms of stream function into BCs given by Equations 3.24-3.35 results in
slip condition,

$$\Psi_y\left(x,0\right)=\left[A_1Kn\Psi_{yy}\left(x,0\right)+A_2Kn^2\Psi_{yyy}\left(x,0\right)\right]+Kn^2\theta_x\left(x,0\right), \tag{3.38}$$

no-slip condition,

$$\Psi_x(x,0) = 0, \tag{3.39}$$

adiabatic BC for temperature on the bottom wall,

$$\theta_y(x,0) = 0, \tag{3.40}$$

slip on the top wall,

$$\Psi_y(x,1) = \left[-A_1 Kn \Psi_{yy}(x,1) + A_2 Kn^2 \Psi_{yyy}(x,1)\right] + Kn^2 \theta_x(x,1), \tag{3.41}$$

no-slip condition,

$$\Psi_x(x,1) = 0, \tag{3.42}$$

temperature jump,

$$\theta(x,1) = \theta_{w3} + \left(\frac{2\gamma}{\gamma+1}\right)\frac{1}{Pr}\left[-A_1 Kn \theta_y(x,1) + A_2 Kn^2 \theta_{yy}(x,1)\right], \tag{3.43}$$

similarly on the left:
no-slip condition for x-wise velocity,

$$\Psi_y(0,y) = 0, \tag{3.44}$$

for vertical velocity component,

$$\Psi_x(0,y) = \left[A_1 Kn \Psi_{xx}(0,y) + A_2 Kn^2 \Psi_{xxx}(0,y)\right], \tag{3.45}$$

temperature jump due to rarefaction effects,

$$\theta(0,y) = \theta_{w4} + \left(\frac{2\gamma}{\gamma+1}\right)\frac{1}{Pr}\left[A_1 Kn\theta_x(0,y) + A_2 Kn^2\theta_{xx}(0,y)\right], \tag{3.46}$$

stick condition of x-wise velocity component on the other side wall,

$$\Psi_y(1,y) = 0, \tag{3.47}$$

for vertical velocity component,

$$\Psi_x(1,y) = \left[-A_1 Kn\Psi_{xx}(1,y) + A_2 Kn^2\Psi_{xxx}(1,y)\right], \tag{3.48}$$

temperature jump due to rarefaction effects,

$$\theta(1,y) = \theta_{w2} + \left(\frac{2\gamma}{\gamma+1}\right)\frac{1}{Pr}\left[-A_1 Kn\theta_x(1,y) + A_2 Kn^2\theta_{xx}(1,y)\right]. \tag{3.49}$$

It should be noted that, stream function formulation decreases the number of unknowns from four to two. There is no doubt that; this arrangement simplifies the application of asymptotic approximation. In the next section, perturbation theory will be exploited to analyze base flow field in the enclosure.

3.3. Asymptotic Solution Procedure

The present analysis aims to elucidate the flow field in an enclosure with small aspect ratio, $\epsilon \ll 1$. In this situation, two distinct flow structures are identified in the enclosure: outer and inner (boundary layer) flow formations. Flow in the outer flow region is relatively simple and generally gives parallel streamlines to the surface. On the other hand, mathematically speaking, the outer solution does not satisfy the side walls region boundary constraints —a singularity arises due to dissatisfaction of any BC of the problem. Therefore, the other asymptotic solution procedure should be applied at the end regions in which the flow turns around to conserve mass. The end solutions are also called as "*inner*" or "*boundary layer*" solution. The inner and outer expansions

complement each other. Each of them has its own validity region. Fortunately, inner and outer expansions can be joined by "*asymptotic matching procedure*" (Van Dyke, 1964; Nayfeh, 1993).

The asymptotic matching principle can be summarized as

$$\begin{aligned} &\textit{The m-term inner expansion of (the n-term outer expansion)} = \\ &\textit{The n-term outer expansion of (the m-term inner expansion)} \end{aligned} \tag{3.50}$$

In this procedure, m and n are any two integers and generally m is set to n or $n+1$ (Van Dyke, 1964). A schematic representation of the asymptotic matching technique can be seen Figure 3.3 Before proceeding with outer and inner expansions, order of

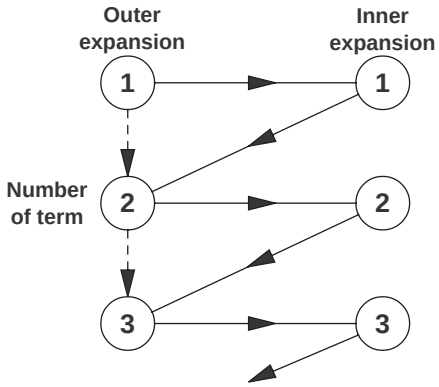

Figure 3.3. Organization of matching order of inner and outer expansions (Solid arrows express step by step progress of matching) (Van Dyke, 1964).

magnitude analysis of dimensionless numbers should be performed. It is clear that Re, Kn and Pr numbers can be represented in terms of asymptotic limits such that

$$Re = Re^{*}\epsilon, \quad Kn = O\left(1\right) \text{ and } \quad Pr = O\left(1/\epsilon\right)$$

with $Re^{*} = O\left(1\right)$. The asymptotic limit of $Re = Re^{*}\epsilon$, depends on the creep flow assumption. Therefore, convective terms in momentum equations are ignored in the leading order approximation (zeroth-order approximation). Asymptotic limit of $Kn = O\left(1/\epsilon\right)$ corresponds to high transition or molecular flow regimes. This limit indicates that continuum flow assumption breaks down and equations of continuum mechanics

can not be used. On the other hand, the limit of $Kn = O(\epsilon)$ leads to totally hydrodynamic flow regime in which rarefaction effects are not observed. The other asymptotic limit, $Kn = O(1)$, generates slip flow regime with $Re = O(\epsilon)$. So; use of this asymptotic limit produces the desired slip flow regime. It should be noted that different alternatives of asymptotic limits of Re and Kn number lead to different flow regimes and flow types of flow such as transonic, hypersonic transition flows, etc. More details about the order of magnitude analysis of Kn number for different Ma and Re numbers can be found in Arkilic *et al.* (1997) The magnitude of Pr number is generally in the range of 0.66-0.72 for the most of gases. Therefore, unity assumption of asymptotic limit of Pr number does not produce any error.

In the next section outer and inner approximation procedure will be exhibited after the completion of order of magnitude analysis.

3.4. Outer Expansion Solution

In this section, outer solutions will be found at different orders by recalling that perturbation parameter, ϵ is sufficiently small. Thus, an uniform outer asymptotic expansion can be written

for stream function,

$$\Psi^o(x,y) = \Psi_0^o(x,y) + \epsilon\Psi_1^o(x,y) + O\left(\epsilon^2\right), \tag{3.51}$$

pressure,

$$p^o(x,y) = p_0^o(x,y) + \epsilon p_1^o(x,y) + O\left(\epsilon^2\right) \tag{3.52}$$

and temperature

$$\theta^o(x,y) = \theta_0^o(x,y) + \epsilon\theta_1^o(x,y) + \epsilon^2\theta_2^o(x,y) + O\left(\epsilon^3\right), \tag{3.53}$$

respectively. Superscript " ^{o} " denotes outer expansion. Note that, third-order expansion of temperature is necessary due to loss of boundary conditions of stream function

formulation as will be verified in the next. Substituting Equations 3.51-3.53 into Equations 3.36-3.49 and equating powers of ϵ, one can get distinct approximations for each order.

The leading-order approach gives the following linear system of equations for stream function,

$$\left(\Psi_0^o\right)_{yyyy} = 0, \tag{3.54}$$

energy,

$$\left(\theta_0^o\right)_{yy} = 0, \tag{3.55}$$

and boundary conditions, on the bottom wall for x- and y-wise velocity components and temperature,

$$\left(\Psi_0^o\right)_y (x,0) = \left[A_1 Kn \left(\Psi_0^o\right)_{yy} (x,0) + A_2 Kn^2 \left(\Psi_0^o\right)_{yyy} (x,0)\right] + Kn^2 \left(\theta_0^o\right)_x (x,0), \tag{3.56}$$

$$\left(\Psi_0^o\right)_x (x,0) = 0, \tag{3.57}$$

$$\left(\theta_0^o\right)_y (x,0) = 0, \tag{3.58}$$

on the top as the sequence with the bottom one,

$$\left(\Psi_0^o\right)_y (x,1) = \left[-A_1 Kn \left(\Psi_0^o\right)_{yy} (x,1) + A_2 \left(\Psi_0^o\right)_{yyy} (x,1)\right] + Kn^2 \left(\theta_0^o\right)_x (x,1), \tag{3.59}$$

$$\left(\Psi_0^o\right)_x (x,1) = 0, \tag{3.60}$$

$$\theta_0^o (x,1) = \theta_{w3} + \left(\frac{2\gamma}{\gamma+1}\right) \frac{1}{Pr} \left[-A_1 Kn \left(\theta_0^o\right)_y (x,1) + A_2 Kn^2 \left(\theta_0^o\right)_{yy} (x,1)\right], \tag{3.61}$$

on the left surface,

$$\left(\Psi_0^o\right)_y(0,y)=0, \tag{3.62}$$

$$\left(\Psi_0^o\right)_x(0,y)=\left[\ A_1Kn\left(\Psi_0^o\right)_{xx}(0,y)+A_2Kn^2\left(\Psi_0^o\right)_{xxx}(0,y)\right], \tag{3.63}$$

$$\theta_0^o(0,y)=\theta_{w4}+\left(\frac{2\gamma}{\gamma+1}\right)\frac{1}{Pr}\left[A_1Kn\left(\theta_0^o\right)_x(0,y)+A_2Kn^2\left(\theta_0^o\right)_{xx}(0,y)\right], \tag{3.64}$$

and on the right one,

$$\left(\Psi_0^o\right)_y(1,y)=0, \tag{3.65}$$

$$\left(\Psi_0^o\right)_x(1,y)=\left[-A_1Kn\left(\Psi_0^o\right)_{xx}(1,y)+A_2Kn^2\left(\Psi_0^o\right)_{xxx}(1,y)\right], \tag{3.66}$$

$$\theta_0^o(1,y)=\theta_{w2}+\left(\frac{2\gamma}{\gamma+1}\right)\frac{1}{Pr}\left[-A_1Kn\left(\theta_0^o\right)_x(1,y)+A_2Kn^2\left(\theta_0^o\right)_{xx}(1,y)\right] \tag{3.67}$$

Because the flow circulates in a closed domain, at any cross-section of the x-direction, the net mass flux should be zero. This was the additional constraint which can be expressed as

$$\int_0^1\left(\Psi_0^o\right)_y dy=\Psi_0^o(x,1)-\Psi_0^o(x,0)=0. \tag{3.68}$$

The solution of θ_0^o satisfying Equation 3.55 and related BCs is simply to be

$$\theta_0^o(x)=x. \tag{3.69}$$

Since mass flow rate at $y=0$, $\Psi_0^o(x,0)$, is zero, $\Psi_0^o(x,1)$ should also be equal to zero due to net mass flow rate restriction, Equation 3.68. Under this conditions, solution of leading-order approximation for stream function and x-wise velocity component,

satisfying Equation 3.54 and related BCs, will be

$$\Psi_0^o(y) = \frac{Kn^2}{1 + 6A_1Kn - 12A_2Kn^2}\left[2y^3 - 3y^2 + y\right], \tag{3.70}$$

$$u_0^o(y) = \frac{Kn^2}{1 + 6A_1Kn - 12A_2Kn^2}\left[6y^2 - 6y + 1\right]. \tag{3.71}$$

Substituting u velocity to Equation 3.20 gives zeroth-order pressure gradient such that

$$\left(p_0^o\right)_x = \frac{12Kn^2}{1 + 6A_1Kn - 12A_2Kn^2}. \tag{3.72}$$

It is clear that the streamline and the horizontal velocity component solutions 3.70 and 3.71 do not satisfy the boundary conditions 3.62 and 3.65. In order to annihilate this disharmony, the leading order solution should be linked to the boundary layer solution of side walls by utilizing method of asymptotic matches. On the other hand, the temperature field θ_0^o satisfies all boundary conditions including end walls, and does not show any boundary layer behavior in the leading-order.

The next-order solution should satisfy both stream function and energy equations and related boundary conditions as well:
stream function,

$$\left(\Psi_1^o\right)_{yyyy} = 0, \tag{3.73}$$

energy,

$$\left(\theta_1^o\right)_{yy} = 0, \tag{3.74}$$

and boundary conditions,

on the bottom:

$$\left(\Psi_1^o\right)_y(x,0) = \left[A_1 Kn \left(\Psi_1^o\right)_{yy}(x,0) + A_2 Kn^2 \left(\Psi_1^o\right)_{yyy}(x,0)\right] + Kn^2 \left(\theta_1^o\right)_x(x,0), \quad (3.75)$$

$$\left(\Psi_1^o\right)_x(x,0) = 0, \quad (3.76)$$

$$\left(\theta_1^o\right)_y(x,0) = 0, \quad (3.77)$$

on the top:

$$\left(\Psi_1^o\right)_y(x,1) = \left[-A_1 Kn \left(\Psi_1^o\right)_{yy}(x,1) + A_2 Kn^2 \left(\Psi_1^o\right)_{yyy}(x,1)\right] + Kn^2 \left(\theta_1^o\right)_x(x,1), \quad (3.78)$$

$$\left(\Psi_1^o\right)_x(x,1) = 0, \quad (3.79)$$

$$\theta_1^o(x,1) = \left(\frac{2\gamma}{\gamma+1}\right)\frac{1}{Pr}\left[-A_1 Kn \left(\theta_1^o\right)_y(x,1) + A_2 Kn^2 \left(\theta_1^o\right)_{yy}(x,1)\right], \quad (3.80)$$

on the left:

$$\left(\Psi_1^o\right)_y(0,y) = 0, \quad (3.81)$$

$$\left(\Psi_1^o\right)_x(0,y) = 0, \quad (3.82)$$

$$\theta_1^o(0,y) = \left(\frac{2\gamma}{\gamma+1}\right)\frac{1}{Pr} A_1 Kn, \quad (3.83)$$

and the right:

$$\left(\Psi_1^o\right)_y(1,y) = 0, \quad (3.84)$$

$$\left(\Psi_1^o\right)_x(1,y)=0, \tag{3.85}$$

$$\theta_1^o(1,y)=-\left(\frac{2\gamma}{\gamma+1}\right)\frac{1}{Pr}A_1Kn. \tag{3.86}$$

Careful examination of Equations 3.74, 3.77 and 3.80 reveals that suitable solution for θ_1^o can only be

$$\theta_1^o=0. \tag{3.87}$$

Clearly, the first-order solution of temperature does not satisfy the requirements on the boundary-layer region. Therefore, corresponding inner approximation must be joined with this outer approximation. In addition to temperature, inspection of Equation 3.73 and all boundary conditions for stream function gives the solution

$$\Psi_1^o=0. \tag{3.88}$$

Definitely, stream function solution satisfies the BCs in the core region and on the end walls.

Accompanying order of approximation results in vanishing pressure gradient as well

$$p_1^o=0. \tag{3.89}$$

Clearly, the order of outer expansion for stream function is limited up to $O(\epsilon^2)$ because there is no necessity to bring out calculations beyond this order. Nevertheless; to expose inner solution of stream function at each order, there will be a need of next order solution of temperature as explained in the next section. Therefore; second-order outer solution of temperature will be investigated in order to compete with the inner approximation. Second-order approximation results in a subsequent energy equation

and associated BCs:

$$\left(\theta_2^o\right)_{yy} = Re^* Pr \left[\left(\Psi_0^o\right)_y \left(\theta_0^o\right)_x\right], \tag{3.90}$$

$$\left(\theta_2^0\right)_y (x,0) = 0, \tag{3.91}$$

$$\theta_2^o (x,1) = \left(\frac{2\gamma}{\gamma+1}\right) \frac{1}{Pr} \left[-A_1 Kn \left(\theta_2^o\right)_y (x,1) + A_2 Kn^2 \left(\theta_2^o\right)_{yy} (x,1)\right], \tag{3.92}$$

$$\theta_2^o (0,y) = \left(\frac{2\gamma}{\gamma+1}\right) \frac{1}{Pr} \left[\ A_1 Kn \left(\theta_1^o\right)_x (0,y) + A_2 Kn^2 \left(\theta_0^o\right)_{xx} (0,y)\right], \tag{3.93}$$

$$\theta_2^o (1,y) = \left(\frac{2\gamma}{\gamma+1}\right) \frac{1}{Pr} \left[-A_1 Kn \left(\theta_1^o\right)_x (1,y) + A_2 Kn^2 \left(\theta_0^o\right)_{xx} (1,y)\right]. \tag{3.94}$$

Substituting Equation 3.70 for zeroth-order solution of stream function and Equations 3.69 and 3.87 for zeroth and first-order solutions of temperature, respectively, solution of energy equation is obtained as

$$\theta_2^o (y) = Re^* Pr \left\{ \frac{Kn^2}{1 + 6A_1 Kn - 12A_2 Kn^2} \left[\frac{1}{2}(y^4+y^2) - y^3 + \left(\frac{2\gamma}{\gamma+1}\right) \frac{A_2 Kn^2}{Pr}\right]\right\} \tag{3.95}$$

Apparently, θ_2^o does not satisfy the BCs of the end regions.

Singular behavior —dissatisfaction BCs of end walls— of the current asymptotic analysis brings us performing inner expansion procedure and method of asymptotic matches as explained in the next section.

3.5. Inner Expansion Solution (Boundary Layer Approximation)

In most physical problems, sharp gradients of flow variables take places in a tiny region such as Jukowski airfoil, flow over round edges etc. (Van Dyke, 1964). Smallness of this region which is generally in a size of $O(\epsilon)$, does not easily permit interpretation

of the flow field. Therefore, stretching or magnification of boundary layer is a standard way eliminating this disadvantage. For the sake of brevity, more details will not be given here and interested readers are referred to any standard textbook about perturbation theory. The next two sections present inner approximations to the proposed model.

3.5.1. Boundary Layer at x = 0

Employing perturbation parameter, ϵ, the left surface region is stretched as

$$\xi = \frac{x}{\epsilon} \quad \text{and} \quad \eta = y,$$

and consequently a new set of governing equations are written as

$$\nabla^4 \tilde{\Psi}^i = Re^* \epsilon \left[\tilde{\Psi}^i_\eta \left(\tilde{\Psi}^i_{\xi\eta\eta} + \tilde{\Psi}^i_{\xi\xi\xi} \right) - \tilde{\Psi}^i_\xi \left(\tilde{\Psi}^i_{\xi\xi\eta} + \tilde{\Psi}^i_{\eta\eta\eta} \right) \right], \tag{3.96}$$

$$\nabla^2 \tilde{\theta}^i = Re^* Pr \epsilon \left[\tilde{\Psi}^i_\eta \tilde{\theta}^i_\xi - \tilde{\Psi}^i_\xi \tilde{\theta}^i_\eta \right], \tag{3.97}$$

where

$$\nabla^4 = \frac{\partial^4}{\partial \xi^4} + 2\frac{\partial^4}{\partial \xi^2 \partial \eta^2} + \frac{\partial^4}{\partial \eta^4} \quad \text{and} \quad \nabla^2 = \frac{\partial^2}{\partial \xi^2} + \frac{\partial^2}{\partial \eta^2}$$

are Biharmonic and Laplacian operators, respectively. Additionally, over tilde, " ˜ ", designates inner expansion at about left wall side. Thus, the coordinate transformation leads to a new class of boundary conditions as the followings
on the bottom surface:

$$(\tilde{\Psi}^i)_\eta(\xi, 0) = \left[A_1 Kn (\tilde{\Psi}^i)_{\eta\eta}(\xi, 0) + A_2 Kn^2 (\tilde{\Psi}^i)_{\eta\eta\eta}(\xi, 0) \right] + \frac{1}{\epsilon} Kn^2 (\tilde{\theta}^i)_\xi(\xi, 0), \tag{3.98}$$

$$(\tilde{\Psi}^i)_\xi(\xi, 0) = 0, \tag{3.99}$$

$$(\tilde{\theta}^i)_\eta(\xi,0)=0, \tag{3.100}$$

on the top surface:

$$(\tilde{\Psi}^i)_\eta(\xi,1)=\left[-A_1Kn(\tilde{\Psi}^i)_{\eta\eta}(\xi,1)+A_2Kn^2(\tilde{\Psi}^i)_{\eta\eta\eta}(\xi,1)\right]+\frac{1}{\epsilon}Kn^2(\tilde{\theta}^i)_\xi(\xi,1), \tag{3.101}$$

$$(\tilde{\Psi}^i)_\xi(\xi,1)=0, \tag{3.102}$$

$$\tilde{\theta}^i(\xi,1)=\epsilon\xi+\left(\frac{2\gamma}{\gamma+1}\right)\frac{1}{Pr}\left[-A_1Kn(\tilde{\theta}^i)_\eta(\xi,1)+A_2Kn^2(\tilde{\theta}^i)_{\eta\eta}(\xi,1)\right], \tag{3.103}$$

and on the left side:

$$(\tilde{\Psi}^i)_\eta(0,\eta)=0, \tag{3.104}$$

$$(\tilde{\Psi}^i)_\xi(0,\eta)=\left[A_1Kn(\tilde{\Psi}^i)_{\xi\xi}(0,\eta)+A_2Kn^2(\tilde{\Psi}^i)_{\xi\xi\xi}(0,\eta)\right], \tag{3.105}$$

$$\tilde{\theta}^i(0,\eta)=\left(\frac{2\gamma}{\gamma+1}\right)\frac{1}{Pr}\left[A_1Kn(\tilde{\theta}^i)_\xi(0,\eta)+A_2Kn^2(\tilde{\theta}^i)_{\xi\xi}(0,\eta)\right]. \tag{3.106}$$

As it can be seen, a complete set of system has not been governed mathematically yet due to lack of some required boundary conditions. Asymptotic matching creates these boundary conditions by recalling a basic idea: *the inner and outer approximations should have the same solution in an overlapping region where solutions of them coincide.* This linkage between two approaches guarantees continuous and smooth transition of solutions from one region to the other region. Fortunately, the application of this principle gives the other conditions such that as $\epsilon\to 0$

$$\lim_{\xi\to\infty}\tilde{\Psi}^i=\lim_{x\to 0^+}\tilde{\Psi}^o, \tag{3.107}$$

$$\lim_{\xi\to\infty}\tilde{\theta}^{i}=\lim_{x\to 0^{+}}\tilde{\theta}^{o}. \tag{3.108}$$

Now, the regular asymptotic series of inner approach for the left boundary are expressed as

$$\tilde{\Psi}^{i}=\tilde{\Psi}_{0}^{i}+\epsilon\tilde{\Psi}_{1}^{i}+O\left(\epsilon^{2}\right), \tag{3.109}$$

$$\tilde{p}^{i}=\tilde{p}_{0}^{i}+\epsilon\tilde{p}_{1}^{i}+O\left(\epsilon^{2}\right), \tag{3.110}$$

$$\tilde{\theta}^{i}=\tilde{\theta}_{0}^{i}+\epsilon\tilde{\theta}_{1}^{i}+\epsilon^{2}\tilde{\theta}_{2}^{i}+O\left(\epsilon^{3}\right), \tag{3.111}$$

Insertion of these expansions to Equations 3.96-3.108 construct zeroth, first and second-order approximations on the side wall. Thus, the leading order approach is written for stream function, energy equations and for BCs,

$$\nabla^{4}\tilde{\Psi}_{0}^{i}=0, \tag{3.112}$$

$$\nabla^{2}\tilde{\theta}_{0}^{i}=0, \tag{3.113}$$

on the bottom surface,

$$(\tilde{\theta}_{0}^{i})_{\xi}(\xi,0)=0, \tag{3.114}$$

$$(\tilde{\Psi}_{0}^{i})_{\xi}(\xi,0)=0, \tag{3.115}$$

$$(\tilde{\theta}_{0}^{i})_{\eta}(\xi,0)=0, \tag{3.116}$$

on the top surface,

$$(\tilde{\theta}_0^i)_\xi(\xi,1)=0, \tag{3.117}$$

$$(\tilde{\Psi}_0^i)_\xi(\xi,1)=0, \tag{3.118}$$

$$\tilde{\theta}_0^i(\xi,1)=\left(\frac{2\gamma}{\gamma+1}\right)\frac{1}{Pr}\left[-A_1Kn\left(\tilde{\theta}_0^i\right)_\eta(\xi,1)+A_2Kn^2(\tilde{\theta}_0^i)_{\eta\eta}(\xi,1)\right], \tag{3.119}$$

and on the left side,

$$(\tilde{\Psi}_0^i)_\eta(0,\eta)=0, \tag{3.120}$$

$$(\tilde{\Psi}_0^i)_\xi(0,\eta)=\left[A_1Kn(\tilde{\Psi}_0^i)_{\xi\xi}(0,\eta)+A_2Kn^2(\tilde{\Psi}_0^i)_{\xi\xi\xi}(0,\eta)\right], \tag{3.121}$$

$$\tilde{\theta}_0^i(0,\eta)=\left(\frac{2\gamma}{\gamma+1}\right)\frac{1}{Pr}\left[A_1Kn(\tilde{\theta}_0^i)_\xi(0,\eta)+A_2Kn^2(\tilde{\theta}_0^i)_{\xi\xi}(0,\eta)\right]. \tag{3.122}$$

Additionally, employment of method of asymptotic matches leads to

$$\lim_{\xi\to\infty}\tilde{\Psi}_0^i=\frac{Kn^2}{1+6A_1Kn-12A_2Kn^2}\left(2\eta^3-3\eta^2+\eta\right), \tag{3.123}$$

$$\lim_{\xi\to\infty}\tilde{\theta}_0^i=0, \tag{3.124}$$

$$\lim_{\xi\to\infty}(\tilde{\Psi}_0^i)_\xi=0. \tag{3.125}$$

Notice that, reduction of order appeared in transpiration terms of Equations 3.98 and 3.101 causes loss of boundary conditions of stream function. Use of Van Dyke's matching procedure given in 3.50 in page 25 and Figure 3.3, enables us expressing outer variables in terms of inner variables at each order. This is the reason why asymptotic

condition addressed Equation 3.123, is written in terms of the inner variables. The condition, Equation 3.123 originates from linking $\tilde{\Psi}_0^i$ with the outer solution Equation 3.70. Examination of energy equation, Equation 3.113, and its boundary conditions advices a solution of

$$\tilde{\theta}_0^i = 0. \tag{3.126}$$

As previously mentioned in page 31, to find zeroth-order stream function solution, we need next order solution of energy equation. Therefore; second-order approach yields expressions

$$\nabla^4 \tilde{\Psi}_1^i = Re^* \Big\{ (\tilde{\Psi}_0^i)_\eta \left[(\tilde{\Psi}_0^i)_{\xi\eta\eta} + (\tilde{\Psi}_0^i)_{\xi\xi\xi} \right] - (\tilde{\Psi}_0^i)_\xi \left[(\tilde{\Psi}_0^i)_{\xi\xi\eta} + (\tilde{\Psi}_0^i)_{\eta\eta\eta} \right] \Big\}, \tag{3.127}$$

$$\nabla^2 \tilde{\theta}_1^i = 0 \tag{3.128}$$

for stream function and energy and BCs
on the bottom:

$$(\tilde{\Psi}_0^i)_\eta(\xi, 0) = \left[A_1 Kn (\tilde{\Psi}_0^i)_{\eta\eta}(\xi, 0) + A_2 Kn^2 (\tilde{\Psi}_0^i)_{\eta\eta\eta}(\xi, 0) \right] + Kn^2 (\tilde{\theta}_1^i)_\xi(\xi, 0), \tag{3.129}$$

$$(\tilde{\Psi}_1^i)_\xi(\xi, 0) = 0, \tag{3.130}$$

$$(\tilde{\theta}_1^i)_\eta(\xi, 0) = 0, \tag{3.131}$$

on the top surface:

$$(\tilde{\Psi}_0^i)_\eta(\xi, 1) = \left[-A_1 Kn (\tilde{\Psi}_0^i)_{\eta\eta}(\xi, 1) + A_2 Kn^2 (\tilde{\Psi}_0^i)_{\eta\eta\eta}(\xi, 1) \right] + Kn^2 (\tilde{\theta}_1^i)_\xi(\xi, 1), \tag{3.132}$$

$$(\tilde{\Psi}_1^i)_\xi(\xi, 1) = 0, \tag{3.133}$$

$$(\tilde{\theta}_1^i)(\xi,1) = \xi + \left(\frac{2\gamma}{\gamma+1}\right)\frac{1}{Pr}\left[-A_1 Kn(\tilde{\theta}_1^i)_\eta(\xi,1) + A_2 Kn^2(\tilde{\theta}_1^i)_{\eta\eta}(\xi,1)\right], \tag{3.134}$$

on the left side:

$$(\tilde{\Psi}_1^i)_\eta(0,\eta) = 0, \tag{3.135}$$

$$(\tilde{\Psi}_1^i)_\xi(0,\eta) = \left[A_1 Kn(\tilde{\Psi}_1^i)_{\xi\xi}(0,\eta) + A_2 Kn^2(\tilde{\Psi}_1^i)_{\xi\xi\xi}(0,\eta)\right], \tag{3.136}$$

$$(\tilde{\theta}_1^i)(0,\eta) = \left(\frac{2\gamma}{\gamma+1}\right)\frac{1}{Pr}\left[A_1 Kn(\tilde{\theta}_1^i)_\xi(0,\eta) + A_2 Kn^2(\tilde{\theta}_1^i)_{\xi\xi}(0,\eta)\right]. \tag{3.137}$$

and matching conditions

$$\lim_{\xi\to\infty} \tilde{\Psi}_1^i = 0, \tag{3.138}$$

$$\lim_{\xi\to\infty} \tilde{\theta}_1^i = \xi, \tag{3.139}$$

$$\lim_{\xi\to\infty} (\tilde{\Psi}_1^i)_\xi = 0. \tag{3.140}$$

Equations 3.129 and 3.132 assign new boundary conditions that are required to close zeroth-order stream function problem, $\tilde{\Psi}_0^i$. Thus, lost BCs are eliminated and combination of Equations 3.115, 3.118, 3.120, 3.121, 3.123, 3.125 and 3.129 governs a new set of boundary conditions for zeroth-order stream function formulation. Determination of $\tilde{\Psi}_1^i$ is analogous to zeroth-order approximation, $\tilde{\Psi}_0^i$. Loss of BCs occurs at this order as well and this drawback can only be eliminated by proceeding to the next order approximation in energy equations, $\tilde{\theta}_2^i$, such that

$$\nabla^2\tilde{\theta}_2^i = Re^* Pr\left[(\tilde{\Psi}_0^i)_\eta(\tilde{\theta}_1^i)_\xi - (\tilde{\Psi}_0^i)_\xi(\tilde{\theta}_1^i)_\eta\right], \tag{3.141}$$

$$(\tilde{\theta}_2^i)_\eta(\xi,0)=0, \tag{3.142}$$

$$\tilde{\theta}_2^i(\xi,1)=\left(\frac{2\gamma}{\gamma+1}\right)\frac{1}{Pr}\left[-A_1Kn(\tilde{\theta}_2^i)_\eta(\xi,1)+A_2Kn^2(\tilde{\theta}_2^i)_{\eta\eta}(\xi,1)\right], \tag{3.143}$$

$$(\tilde{\theta}_2^i)(0,\eta)=\left(\frac{\gamma}{\gamma+1}\right)\frac{1}{Pr}\left[A_1Kn(\tilde{\theta}_2^i)_\xi(0,\eta)+A_2Kn^2(\tilde{\theta}_2^i)_{\xi\xi}(0,\eta)\right], \tag{3.144}$$

$$\lim_{\xi\to\infty}\tilde{\theta}_2^i=Re^*Pr\left\{\frac{Kn^2}{1+6A_1Kn-12A_2Kn^2}\left[\frac{1}{2}(\eta^4+\eta^2)-\eta^3+\left(\frac{2\gamma}{\gamma+1}\right)\frac{A_2Kn^2}{Pr}\right]\right\}. \tag{3.145}$$

Determination of $\tilde{\theta}_1^i$ and $\tilde{\theta}_2^i$ are straightforward by employing the second-order finite difference scheme. Second-order forward and backward discretizations have been applied on the boundaries wherever needed. System of algebraic equations were solved via **S**uccessive **O**ver **R**elaxation (SOR) with relaxation parameter of $\omega=1.6$. Results and discussions about the temperature field affected by mainly rarefaction jumps will be given in Section 3.6. After finding the solution of $\tilde{\theta}_2^i$, lost boundary conditions of $\tilde{\Psi}_1^i$ can be reformulated as the previous case. Therefore; Equations 3.129 and 3.132 are replaced by the following new BCs of bottom and top boundaries

$$(\tilde{\Psi}_1^i)_\eta(\xi,0)=\left[A_1Kn(\tilde{\Psi}_1^i)_{\eta\eta}(\xi,0)+A_2Kn^2(\tilde{\Psi}_1^i)_{\eta\eta\eta}(\xi,0)\right]+Kn^2(\tilde{\theta}_2^i)_\xi(\xi,0), \tag{3.146}$$

$$(\tilde{\Psi}_1^i)_\eta(\xi,1)=\left[-A_1Kn(\tilde{\Psi}_1^i)_{\eta\eta}(\xi,1)+A_2Kn^2(\tilde{\Psi}_1^i)_{\eta\eta\eta}(\xi,1)\right]+Kn^2(\tilde{\theta}_2^i)_\xi(\xi,1). \tag{3.147}$$

Combining Equations 3.146 and 3.147 with Equations 3.130, 3.133, 3.135, 3.136, 3.138 and 3.140 closes the problem mathematically for $\tilde{\Psi}_1^i$. One of the common methodologies for solving the Biharmonic equation is splitting Biharmonic operator into two Poisson equations (Gupta *et al.*, 1979a). On the other hand; a less expensive way of solving the Biharmonic equation is a method such that fourth-order equation is discretized by any discretization scheme and solved directly (Gupta *et al.*, 1979b). Nowadays, usage of compact finite difference have gathered tremendous interest in fluid mechanics

due to higher order accuracy like spectral methods. The fundamentals and details of compact finite differencing can be found in a monograph of Collatz (1966) and Lele (1992), respectively. The current study also employs fourth order compact finite difference scheme pointed out by Stephenson (1983) and Altas *et al.* (1998). Details of discretization are given in Appendix A. SOR iterations converge a solution with the value of relaxation parameters at about $\omega = 0.7$. After exhibition of left side inner approximation, the right side will be examined, finally.

3.5.2. Boundary Layer at x = 1

Investigation of the thermal and flow field on the right side requires such

$$\alpha = \frac{1-x}{\epsilon} \quad \text{and} \quad \beta = y,$$

coordinate transformations. Governing equations and BCs in the new domain of interest are declared by the following system of stream function, energy and relevant BCs:

$$\nabla^4 \hat{\Psi}^i = Re^* \epsilon \left[\hat{\Psi}^i_\alpha \left(\hat{\Psi}^i_{\beta\beta\beta} + \hat{\Psi}^i_{\alpha\alpha\beta} \right) - \hat{\Psi}^i_\beta \left(\hat{\Psi}^i_{\alpha\beta\beta} + \hat{\Psi}^i_{\alpha\alpha\alpha} \right) \right], \tag{3.148}$$

$$\nabla^2 \hat{\theta}^i = Re^* Pr \epsilon \left[\hat{\Psi}^i_\alpha \hat{\theta}^i_\beta - \hat{\Psi}^i_\beta \hat{\theta}^i_\alpha \right] \tag{3.149}$$

BCs on the bottom surface:

$$(\hat{\Psi}^i)_\beta(\alpha,0) = \left[A_1 Kn (\hat{\Psi}^i)_{\beta\beta}(\alpha,0) + A_2 Kn^2 (\hat{\Psi}^i)_{\beta\beta\beta}(\alpha,0) \right] - \frac{1}{\epsilon} Kn^2 (\hat{\theta}^i)_\alpha(\alpha,0), \tag{3.150}$$

$$(\hat{\Psi}^i)_\alpha(\alpha,0) = 0, \tag{3.151}$$

$$(\hat{\theta}^i)_\beta(\alpha,0) = 0, \tag{3.152}$$

on the top surface:

$$(\hat{\Psi}^i)_\beta(\alpha,1) = \left[-A_1 Kn(\hat{\Psi}^i)_{\beta\beta}(\alpha,1) + A_2 Kn^2(\hat{\Psi}^i)_{\beta\beta\beta}(\alpha,1)\right] - \frac{1}{\epsilon} Kn^2(\hat{\theta}^i)_\alpha(\alpha,1), \tag{3.153}$$

$$(\hat{\Psi}^i)_\alpha(\alpha,1) = 0, \tag{3.154}$$

$$\hat{\theta}^i(\alpha,1) = (1-\epsilon\alpha) + \left(\frac{2\gamma}{\gamma+1}\right)\frac{1}{Pr}\left[-A_1 Kn(\hat{\theta}^i)_\beta(\alpha,1) + A_2 Kn^2(\hat{\theta}^i)_{\beta\beta}(\alpha,1)\right], \tag{3.155}$$

and on the right side:

$$(\hat{\Psi}^i)_\beta(0,\beta) = 0, \tag{3.156}$$

$$(\hat{\Psi}^i)_\alpha(0,\beta) = \left[A_1 Kn(\hat{\Psi}^i)_{\alpha\alpha}(0,\beta) + A_2 Kn^2(\hat{\Psi}^i)_{\alpha\alpha\alpha}(0,\beta)\right], \tag{3.157}$$

$$\hat{\theta}^i(0,\beta) = 1 + \left(\frac{2\gamma}{\gamma+1}\right)\frac{1}{Pr}\left[A_1 Kn(\hat{\theta}^i)_\alpha(0,\beta) + A_2 Kn^2(\hat{\theta}^i)_{\alpha\alpha}(0,\beta)\right] \tag{3.158}$$

and matching conditions:

$$\lim_{\alpha\to\infty} \hat{\Psi}^i = \lim_{x\to 1^-} \hat{\Psi}^o, \tag{3.159}$$

$$\lim_{\alpha\to\infty} \hat{\theta}^i = \lim_{x\to 1^-} \hat{\theta}^o. \tag{3.160}$$

Here, " $\hat{}$ " stands for the inner approximation on the right side. Analogous to the previous case, asymptotic expansion takes the form of

$$\hat{\Psi}^i = \hat{\Psi}^i_0 + \epsilon\hat{\Psi}^i_1 + O\left(\epsilon^2\right), \tag{3.161}$$

$$\hat{p}^i = \hat{p}_0^i + \epsilon \hat{p}_1^i + O\left(\epsilon^2\right), \tag{3.162}$$

$$\hat{\theta}^i = \hat{\theta}_0^i + \epsilon \hat{\theta}_1^i + \epsilon^2 \hat{\theta}_2^i + O\left(\epsilon^3\right). \tag{3.163}$$

The leading-order expansion produces a dominant solution of the expansion and takes the following form for governing equations:

$$\nabla^4 \hat{\Psi}_0^i = 0, \tag{3.164}$$

$$\nabla^2 \hat{\theta}_0^i = 0, \tag{3.165}$$

and for BCs: on the bottom,

$$(\hat{\theta}_0^i)_\alpha(\alpha, 0) = 0, \tag{3.166}$$

$$(\hat{\Psi}_0^i)_\alpha(\alpha, 0) = 0, \tag{3.167}$$

$$(\hat{\theta}_0^i)_\beta(\alpha, 0) = 0, \tag{3.168}$$

on the top surface,

$$(\hat{\theta}_0^i)_\alpha(\alpha, 1) = 0, \tag{3.169}$$

$$(\hat{\Psi}_0^i)_\alpha(\alpha, 1) = 0, \tag{3.170}$$

$$\hat{\theta}_0^i(\alpha, 1) = 1 + (\frac{2\gamma}{\gamma + 1})\frac{1}{Pr}\left[-A_1 Kn(\hat{\theta}_0^i)_\beta(\alpha, 1) + A_2(\hat{\theta}_0^i)_{\beta\beta}(\alpha, 1)\right], \tag{3.171}$$

and right side,

$$(\hat{\Psi}_0^i)_\beta(0,\beta) = 0, \tag{3.172}$$

$$(\hat{\Psi}_0^i)_\alpha(0,\beta) = \left[A_1 Kn(\hat{\Psi}_0^i)_{\alpha\alpha}(0,\beta) + A_2 Kn^2(\hat{\Psi}_0^i)_{\alpha\alpha\alpha}(0,\beta)\right], \tag{3.173}$$

$$\hat{\theta}_0^i(0,\beta) = 1 + \left(\frac{2\gamma}{\gamma+1}\right)\frac{1}{Pr}\left[A_1 Kn(\hat{\theta}_0^i)_\alpha(0,\beta) + A_2 Kn^2(\hat{\theta}_0^i)_{\alpha\alpha}(0,\beta)\right], \tag{3.174}$$

and for matching conditions:

$$\lim_{\alpha\to\infty}\hat{\Psi}_0^i = \frac{Kn^2}{1+6A_1Kn-12A_2Kn^2}\left(2\beta^3-3\beta^2+\beta\right), \tag{3.175}$$

$$\lim_{\alpha\to\infty}\hat{\theta}_0^i = 1, \tag{3.176}$$

$$\lim_{\alpha\to\infty}(\hat{\Psi}_0^i)_\alpha = 0. \tag{3.177}$$

Solution of the zeroth-order energy equation will be simply

$$\hat{\theta}_0^i = 0. \tag{3.178}$$

Similar to the procedure applied on the $x = 0$, next order approximation of the energy equation should be discussed firstly to proceed in the solution of $\hat{\Psi}_0^i$. The first-order problem follows for stream function and energy equations:

$$\nabla^4\hat{\Psi}_1^i = Re^*\left\{(\hat{\Psi}_0^i)_\alpha\left[(\hat{\Psi}_0^i)_{\beta\beta\beta} + (\hat{\Psi}_0^i)_{\alpha\alpha\beta}\right] - (\hat{\Psi}_0^i)_\beta\left[(\hat{\Psi}_0^i)_{\alpha\beta\beta} + (\hat{\Psi}_0^i)_{\alpha\alpha\alpha}\right]\right\}, \tag{3.179}$$

$$\nabla^2\hat{\theta}_1^i = 0 \tag{3.180}$$

and BCs on the bottom:

$$(\hat{\Psi}_0^i)_\beta(\alpha,0) = \left[A_1 Kn(\hat{\Psi}_0^i)_{\beta\beta}(\alpha,0) + A_2 Kn^2(\hat{\Psi}_0^i)_{\beta\beta\beta}(\alpha,0)\right] - Kn^2(\hat{\theta}_1^i)_\alpha(\alpha,0), \quad (3.181)$$

$$(\hat{\Psi}_1^i)_\alpha(\alpha,0) = 0, \quad (3.182)$$

$$(\hat{\theta}_1^i)_\beta(\alpha,0) = 0, \quad (3.183)$$

on the top surface:

$$(\hat{\Psi}_0^i)_\beta(\alpha,1) = \left[-A_1 Kn(\hat{\Psi}_0^i)_{\beta\beta}(\alpha,1) + A_2 Kn^2(\hat{\Psi}_0^i)_{\beta\beta\beta}(\alpha,1)\right] - Kn^2(\hat{\theta}_1^i)_\alpha(\alpha,1), \quad (3.184)$$

$$(\hat{\Psi}_1^i)_\alpha(\alpha,1) = 0, \quad (3.185)$$

$$\hat{\theta}_1^i(\alpha,1) = -\alpha + \left(\frac{2\gamma}{\gamma+1}\right)\frac{1}{Pr}\left[-A_1 Kn(\hat{\theta}_1^i)_\beta(\alpha,1) + A_2 Kn^2(\hat{\theta}_1^i)_{\beta\beta}(\alpha,1)\right], \quad (3.186)$$

on the right side:

$$(\hat{\Psi}_1^i)_\beta(0,\beta) = 0, \quad (3.187)$$

$$(\hat{\Psi}_1^i)_\alpha(0,\beta) = \left[A_1 Kn(\hat{\Psi}_1^i)_{\alpha\alpha}(0,\beta) + A_2 Kn^2(\hat{\Psi}_1^i)_{\alpha\alpha\alpha}(0,\beta)\right], \quad (3.188)$$

$$\hat{\theta}_1^i(0,\beta) = \left(\frac{2\gamma}{\gamma+1}\right)\frac{1}{Pr}\left[A_1 Kn(\hat{\theta}_1^i)_\alpha(0,\beta) + A_2 Kn^2(\hat{\theta}_1^i)_{\alpha\alpha}(0,\beta)\right]. \quad (3.189)$$

and for matching conditions

$$\lim_{\alpha\to\infty} \hat{\Psi}_1^i = 0, \quad (3.190)$$

$$\lim_{\alpha\to\infty}\hat{\theta}_1^i = -\alpha, \tag{3.191}$$

$$\lim_{\alpha\to\infty}(\hat{\Psi}_1^i)_\alpha = 0. \tag{3.192}$$

Now, Equations 3.167, 3.170, 3.172-3.173, 3.175 and 3.176 associate with 3.181 and 3.184 built a new class of boundary conditions for $\hat{\Psi}_0^i$.

Similarly, the first-order problem of stream function needs second-order approximation of temperature such that

$$(\hat{\Psi}_1^i)_\beta(\alpha,0) = \left[A_1 Kn(\hat{\Psi}_1^i)_{\beta\beta}(\alpha,0) + A_2 Kn^2(\hat{\Psi}_1^i)_{\beta\beta\beta}(\alpha,0)\right] - Kn^2(\hat{\theta}_2^i)_\alpha(\alpha,0), \tag{3.193}$$

$$(\hat{\Psi}_1^i)_\beta(\alpha,1) = \left[-A_1 Kn(\hat{\Psi}_1^i)_{\beta\beta}(\alpha,1) + A_2 Kn^2(\hat{\Psi}_1^i)_{\beta\beta\beta}(\alpha,1)\right] - Kn^2(\hat{\theta}_2^i)_\alpha(\alpha,1). \tag{3.194}$$

Clearly, introduction of new boundary conditions, Equations 3.193 and 3.194 for $\hat{\Psi}_1^i$, close the problem associated with 3.182, 3.185, 3.187-3.188, 3.190 and 3.191.

Second-order estimation for the temperature is formulated as

$$\nabla^2\hat{\theta}_2^i = Re^* Pr\left[(\hat{\Psi}_0^i)_\alpha(\hat{\theta}_1^i)_\beta - (\hat{\Psi}_0^i)_\beta(\hat{\theta}_1^i)_\alpha\right], \tag{3.195}$$

$$(\hat{\theta}_2^i)_\beta(\alpha,0) = 0, \tag{3.196}$$

$$\hat{\theta}_2^i(\alpha,1) = \left(\frac{2\gamma}{\gamma+1}\right)\frac{1}{Pr}\left[-A_1 Kn(\hat{\theta}_2^i)_\beta(\alpha,1) + A_2 Kn^2(\hat{\theta}_2^i)_{\beta\beta}(\alpha,1)\right], \tag{3.197}$$

$$(\hat{\theta}_2^i)(0,\beta) = \left(\frac{2\gamma}{\gamma+1}\right)\frac{1}{Pr}\left[A_1 Kn(\hat{\theta}_2^i)_\alpha(0,\beta) + A_2 Kn^2(\hat{\theta}_2^i)_{\alpha\alpha}(0,\beta)\right], \tag{3.198}$$

$$\lim_{\alpha\to\infty}\hat{\theta}_2^i = Re^* Pr\left\{\frac{Kn^2}{1+6A_1 Kn - 12A_2 Kn^2}\left[\frac{1}{2}(\beta^4+\beta^2) - \beta^3 + \left(\frac{2\gamma}{\gamma+1}\right)\frac{A_2 Kn^2}{Pr}\right]\right\}. \tag{3.199}$$

Numerical treatments of the $\hat{\theta}_1^i$, $\hat{\theta}_2^i$, $\hat{\Psi}_0^i$ and $\hat{\Psi}_1^i$ are the same as those of the left side. However, recall that the solution domain of interest divided to three distinguished region, namely, left and right sides of inner problem and the core region of outer problem. Since, the outer solution is valid in the entire domain except in a small interval of $O(\epsilon)$ in the proximity of the ends, and also the inner solution is only valid in this small distance; a global approach which is valid in the entire domain is demanded. Two common methods are used widely to construct a general solution which is called *composite solution*. In the first technique, *additive composition*, the inner and outer expansions are summed and then the part they have in common is subtracted from the sum so that it is not counted twice.

$$\Psi^c_{(m,n)} = \Psi^i_{(m)} + \Psi^o_{(n)} - \left[\Psi^o_{(n)}\right]^i_{(m)},$$

$$\Psi^c_{(m,n)} = \Psi^o_{(n)} + \Psi^i_{(m)} - \left[\Psi^i_{(m)}\right]^o_{(n)}.$$

Here, for example $\Psi^i_{(m)}$ means the m-term inner expansion, and the other terms use the same convention as well. The second method is called as *multiplicative composition*. In this methodology, the outer expansion multiplied by a correction factor which is a ratio of the inner expansion to its outer one. This rule is also valid for the inner expansion.

$$\Psi^c_{(m,n)} = \Psi^o_{(n)} \frac{\Psi^i_{(m)}}{\left[\Psi^i_{(m)}\right]^o_{(n)}}$$

$$= \Psi^i_{(m)} \frac{\Psi^o_{(n)}}{\left[\Psi^o_{(n)}\right]^i_{(m)}}.$$

In the current work, *additive composition* technique has been applied to get global solutions for both flow and temperature distributions. The presentation of the solutions are left to the next section.

3.6. Results and Discussions

In this section, the results of asymptotic analysis will be given. In all computations, the aspect ratio $\epsilon = 0.02$ and $Pr = 0.72$ number are kept constant. Two concurrent vortices are identified in the enclosure (Figure 3.4). While the upper branch rotates in the clockwise direction, the lower one rotates in the counter-clockwise direction as well. In Figure 3.5 and 3.6 leading order streamlines on the left side have been shown for $Kn = 0.1$ and $Kn = 0.3$, respectively. Clearly, inspection of both figures reveals that resulting streamlines are pretty parallel to horizontal axis for $\xi \geqslant 3$. Moreover, streamlines of the leading-order inner solution perfectly matches with corresponding solution of outer expansion. A comparison between the u velocity profiles of inner approximation for $Kn = 0.1$ and $Kn = 0.3$ is demonstrated in Figures 3.7 and 3.8. A flow structure like thermal boundary-layer is identified on both walls. At the corners of the bottom and top walls, u velocity is almost negligible, and accelerates rapidly as the flow proceeds with the horizontal direction. To analyze such a motion in more details, consider that a gas which is bounded by infinitely long parallel plates at $y = 0$ and $y = 1$, is initially at rest. If both plates are allowed to start a sudden motion at a constant velocity of $U = \frac{Kn^2}{1+6A_1Kn-12A_2Kn^2}$ (from Equation 3.71), the motion can be described by
the following equation

$$\frac{\partial u}{\partial t} = \frac{1}{Re}\frac{\partial^2 u}{\partial y^2}, \tag{3.200}$$

and the BCs
at $y = 0$ and $y = 1/2$ (symmetry BC)

$$u(0,t) = 1 \qquad \left.\frac{\partial u}{\partial y}\right|_{y=\frac{1}{2}} = 0 \qquad \text{for} \quad t > 0, \tag{3.201}$$

and initial condition

$$u(y,0) = 0 \qquad \text{for} \quad 0 < y < \frac{1}{2} \tag{3.202}$$

where Re number is defined as $Re = \rho U d/2\mu$. Once the plates starts to motion, the fluid brought into motion through the action of wall shear stress. The fluid particles continues to accelerate until the steady-state condition takes place; in which the motion has a constant velocity of U. Time evolution of this motion splits into two stages:

`Stage 1.` a flow until a moment of the time, $t_1 > 0$ in which the particles settled along the centerline of the enclosure start to move due to viscous diffusion, and

`Stage 2.` development of the flow until a moment of the time, $t_2 > t_1$ in which all fluid particles have the same velocity with the velocity (uniform) of walls.

Solution of Equations 3.200-3.202 gives gradual influence of viscous diffusion on the motion (Batchelor, 1967). The proposed model enables us verifying transient behavior of the motion (between $0 < t < t_1$), which is neglected in the asymptotic analysis. Notice that, the boundary layer on the bottom wall develops later than the top wall (these regions were bordered by rectangles in Figures 3.7 and 3.8). On the other hand, examination of Figures 3.9 and 3.10 shows different temperature gradient on the top and bottom walls due to different temperature jumps realized along the stream-wise direction mainly. Adiabatic wall condition on the bottom wall leads to slightly sharp gradient than the top wall, and it causes more velocity slip on the bottom wall as well. This is the reason why development of boundary layer occurs in a longer length on the bottom rather than the top. Another point to be discussed is the effect of rarefaction on the boundary layer. As Kn number increases, the entrance length (like thermal entrance length as mentioned previous paragraphs) will also grow as inspected from Figures 3.7 and 3.8. The flow generates two asymmetric branches on the side walls, and turns around them to conserve the mass flow rate. The resulting asymmetry originates from exactly unequal temperature jumps on the bottom and top half. Since there is no-heat transfer in the vertical direction, the effect of temperature jump is negligible.

First-order temperature distributions for $Kn = 0.1$ and $Kn = 0.3$ have been shown in Figures 3.9 and 3.10, respectively. Since the heat is conducted along the negative ξ direction, temperatures of the side walls are different than zero and take the values (at $y = 1/2$) of $T_l = 0.080$ and $T_l = 0.157$ for $Kn = 0.1$ and $Kn = 0.3$,

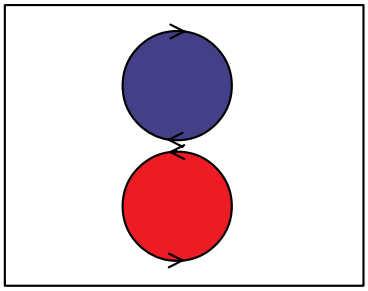

Figure 3.4. Directions of vortices generated by the thermal transpiration effect

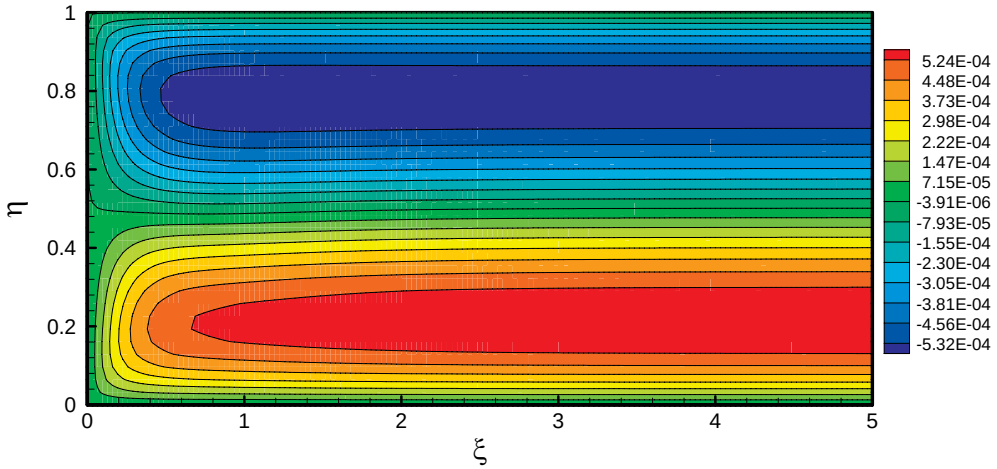

Figure 3.5. Leading order streamlines on the left end wall for $Re^* = 2.5$, $Kn = 0.1$ and $Pr = 0.72$

respectively.

The response of temperature jump to variations in Re number is illustrated in Figure 3.16. Clearly, the effect of Re number on the temperature distribution is constrained by the thermal conditions of the boundaries. Insulation of the bottom boundary decreases the temperature jump. On the other hand, more temperature jump is observed on the top wall on which the temperature varies linearly. Therefore, the temperature field mainly depends on the types of boundary conditions. Figure 3.12 shows first-order approximation to the stream function on the left wall. Nevertheless, the contribution of this order may be negligible for small aspect ratios if Re^* number is sufficiently small. On the other hand, second-order contributions to temperature distribution are shown in Figures 3.13 and 3.14. The effect of this order becomes dominant on the lower branch of the enclosure as inspected from figures. Notice a hot spot on the lower half and the effect of Kn number on this region. As Kn number increases the spots widens as well. The other point should be considered that the

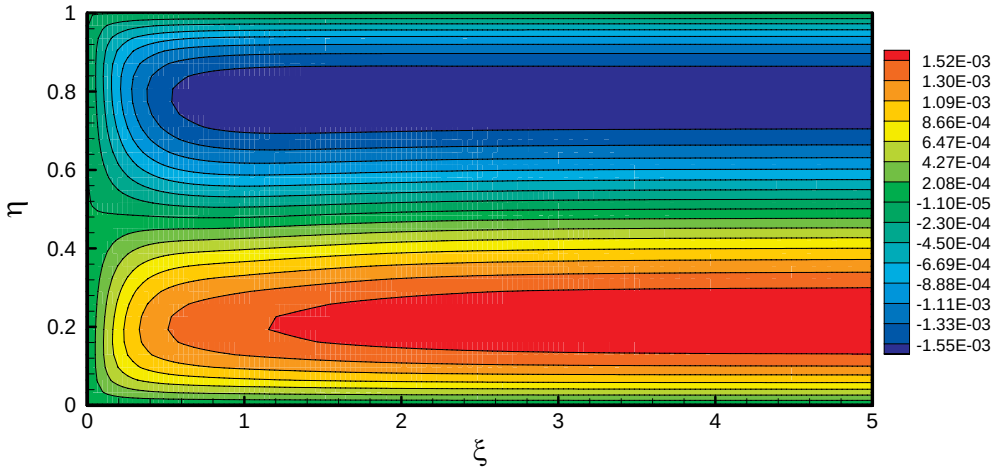

Figure 3.6. Leading order streamlines on the left end wall for $Re^* = 2.5$, $Kn = 0.3$ and $Pr = 0.72$

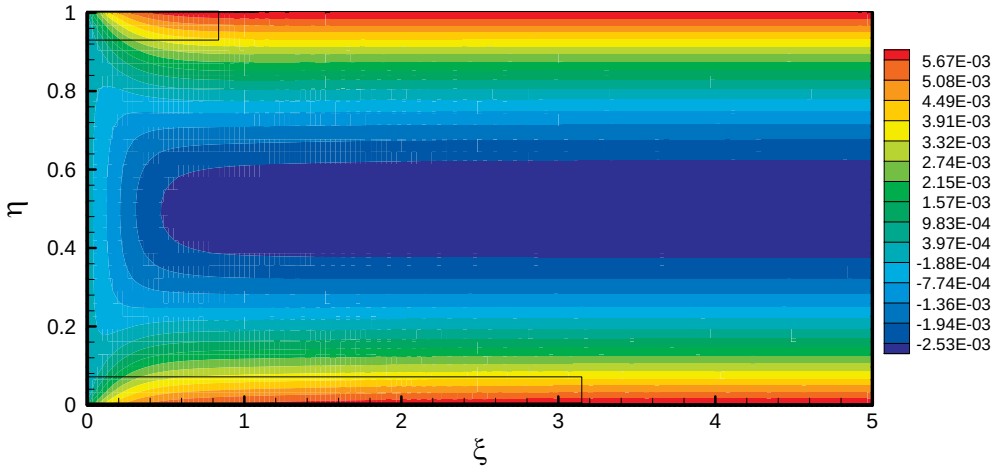

Figure 3.7. Leading order u velocity distribution on the left end wall for $Re^* = 2.5$, $Kn = 0.1$ and $Pr = 0.72$

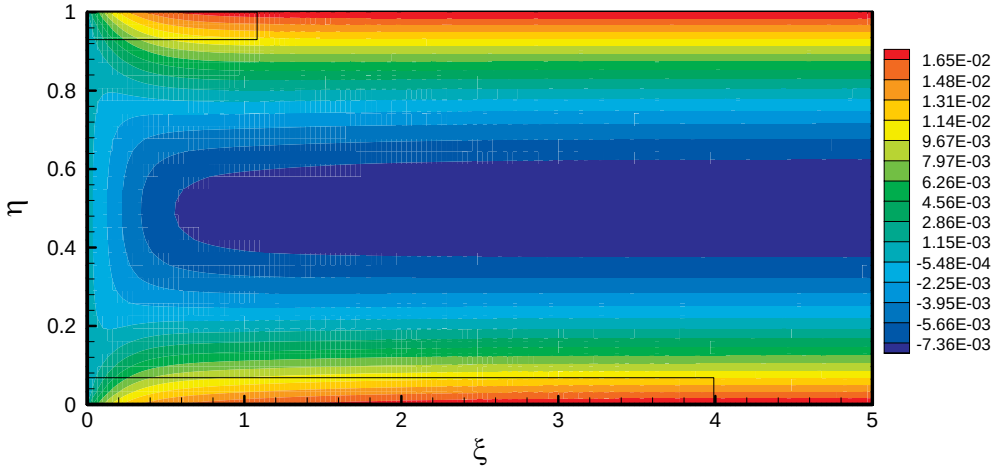

Figure 3.8. Leading order u velocity distribution on the left end wall for $Re^* = 2.5$, $Kn = 0.3$ and $Pr = 0.72$

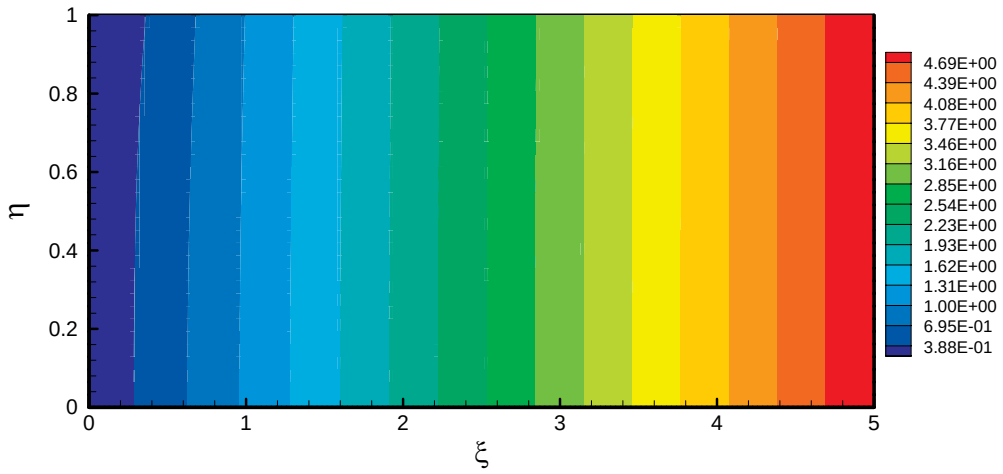

Figure 3.9. First-order temperature field on the left end wall for $Re^* = 2.5$, $Kn = 0.1$ and $Pr = 0.72$

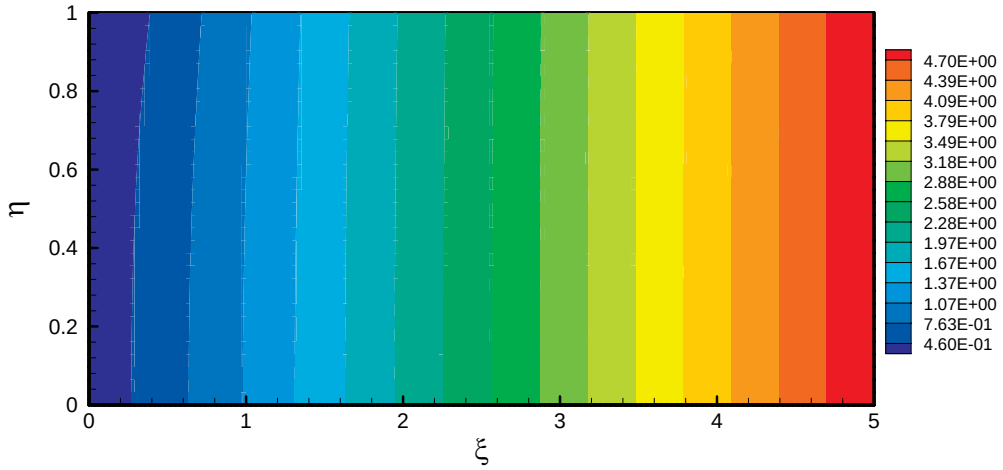

Figure 3.10. First-order temperature field on the left end wall for $Re^* = 2.5$, $Kn = 0.3$ and $Pr = 0.72$

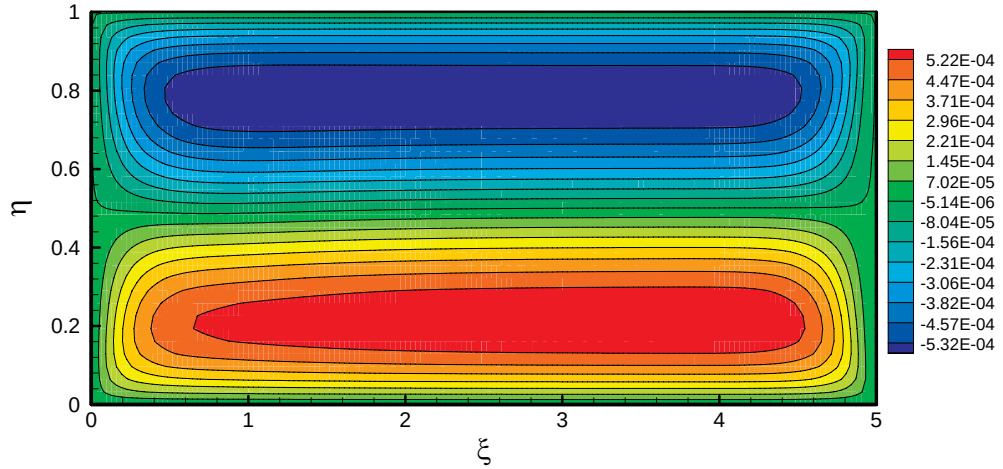

Figure 3.11. First-order approximations to streamlines on the left wall for $Re^* = 2.5$, $Kn = 0.1$ and $Pr = 0.72$

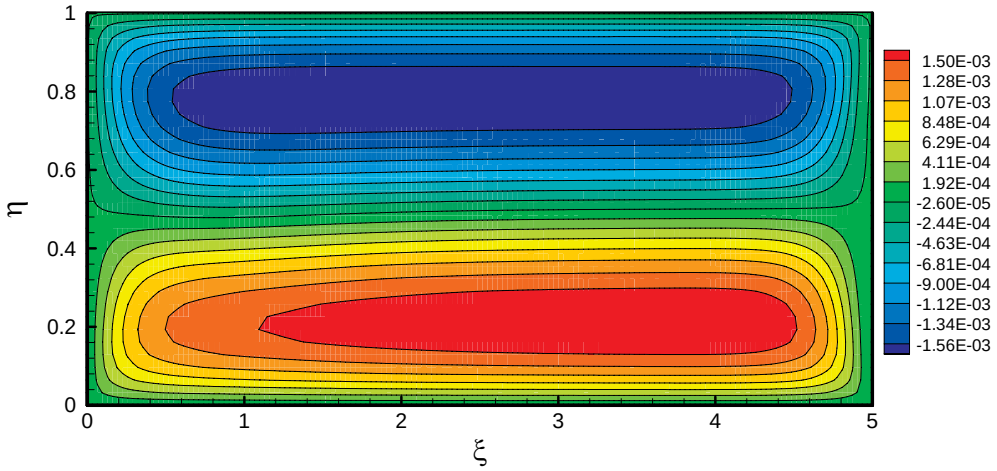

Figure 3.12. First-order approximations to streamlines on the left wall for $Re^* = 2.5$, $Kn = 0.3$ and $Pr = 0.72$

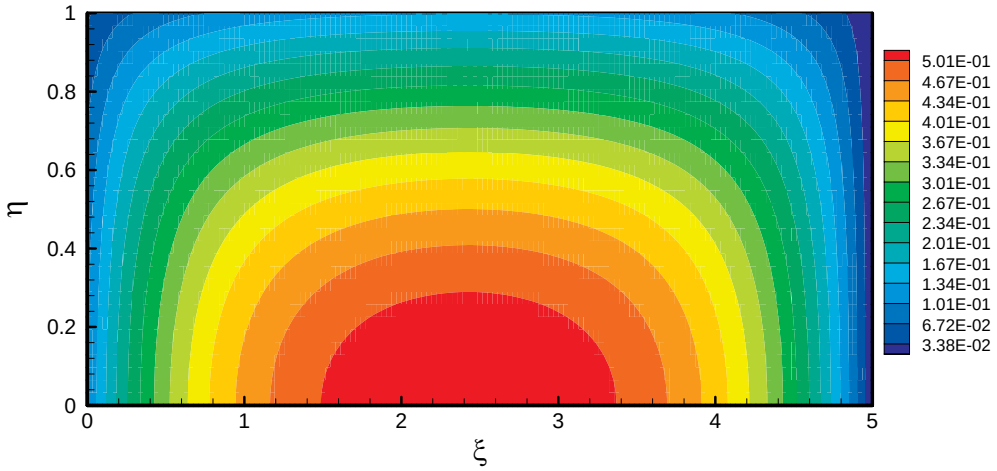

Figure 3.13. Second-order approximations to temperature on the left wall for $Re^* = 2.5$, $Kn = 0.1$ and $Pr = 0.72$

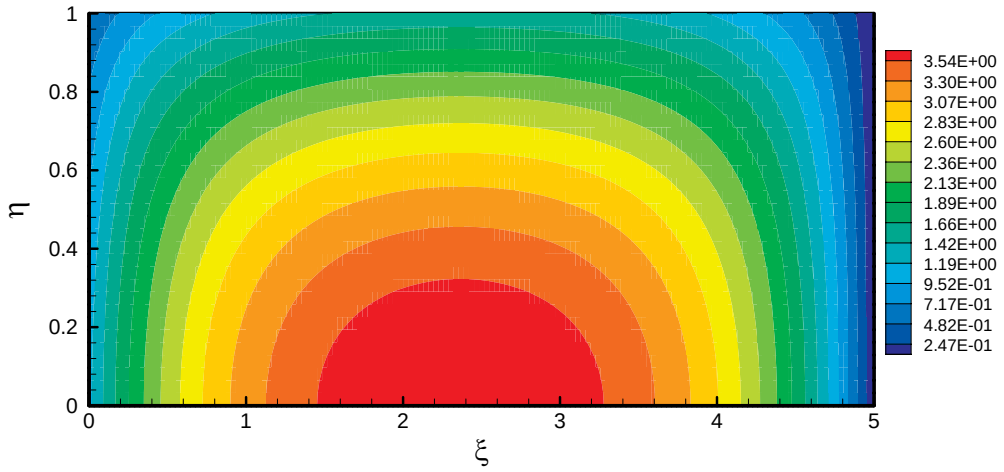

Figure 3.14. Second-order approximations to temperature on the left wall for $Re^* = 2.5$, $Kn = 0.3$ and $Pr = 0.72$

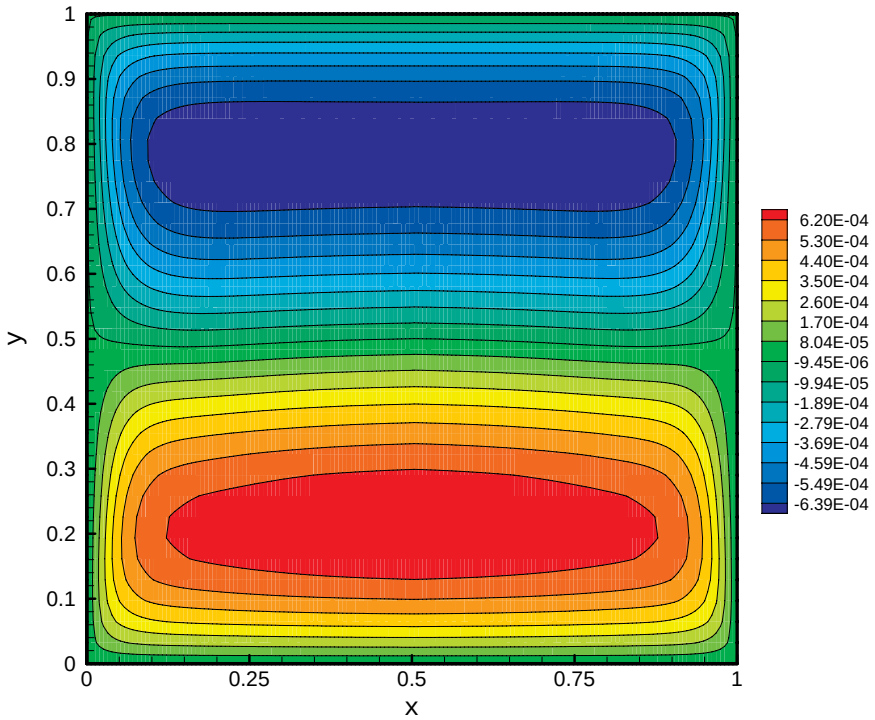

Figure 3.15. Composite streamlines by additive composition for $Re^* = 7.5$, $Kn = 0.1$ and $Pr = 0.72$

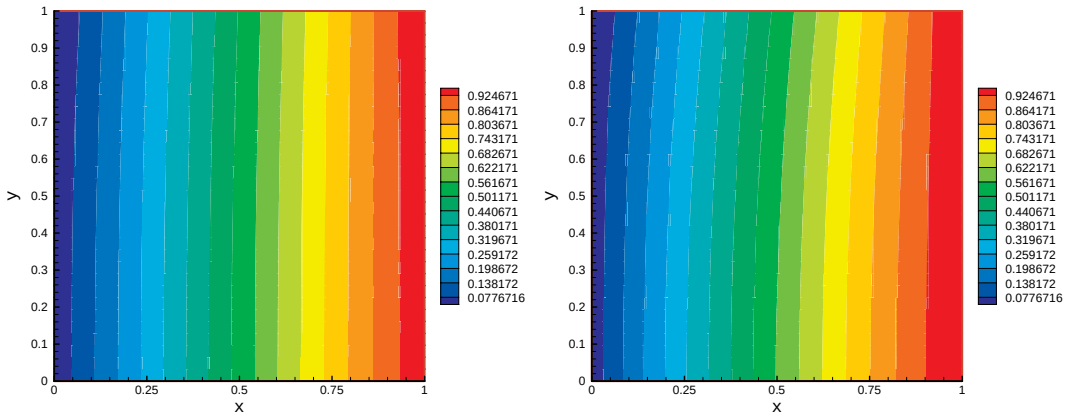

Figure 3.16. The effect of Re number on the temperature distribution for $Kn = 0.1$ and $Pr = 0.72$; for $Re^* = 2.5$ (left figure) and $Re^* = 7.5$ (right figure)

second-order temperature profile shows different gradients on both horizontal walls. A composite streamline is shown in Figures 3.15. Adiabatic boundary condition on the bottom wall causes a thicker streamline pattern as detected from the figure. As previously mentioned, this flow behavior is a natural result of much slip on the lower boundary than the upper one due to slightly different temperature gradient.

To sum up, thermally driven creep flow of the rarefied gases in enclosures has been examined in this chapter. A linear temperature gradient has been enforced along the layer of fluid by keeping side walls at different temperatures. The temperature of the upper wall varies linearly while the lower one is kept adiabatic. The flow directs mainly along the horizontal axis and turns around the side edges in order to satisfy mass conservation law. Regular perturbation has been applied in the asymptotic analysis to evaluate both hydro- and thermo-dynamic characteristics of the flow. For this purpose, a coordinate scaling standing for the regular perturbation parameter is used. Nevertheless, regular perturbation series fail to predict the solutions on the end regions. So, the domain of interest has been divided into three regions: the core and the left and right ends. Solutions have been obtained at different order of approximations on these regions via outer and inner expansions. Once the solutions are found, the remaining task is to join two types of solutions via method of asymptotic matches. Additive composition technique allows us getting global flow and temperature fields. From the

resulting mass and temperature fields, one can make the following deductions:

- A thermal boundary-layer like motion has been identified on the horizontal walls near the ends. Velocity slip on the lateral walls are responsible from such boundary layers. As Kn number increases, hydrodynamic entrance length also increases.
- Boundary conditions and also temperature jumps greatly affect viscous diffusions. Both Kn number (rarefaction) and boundary conditions enlarge or lessen the length of the boundary layer. Although, much temperature jump is observed on the top surface, more slip velocity is taken place on the bottom one due to larger temperature gradient. This leads to more viscous diffusion to the core region of the flow and thicker vortex pattern as well.
- Time evolution of such a motion is accomplished via the analogy to a flow between the suddenly moved parallel plates. Thus, diffusion time at which particles of the fluid along the center-line of enclosure sense viscous diffusion, can be easily obtained.
- Temperature jump is also affected by Re number which designates temperature difference between the end walls for current study as well.
- Although the contribution of the first-order stream function is less than the leading-order, flow pattern at this order convects composite flow character. On the other hand, second order approximation may be more important as Re number increases. An interesting feature of the second-order approximation is the creation of the hot spot on the bottom site.
- The present work neglects compressibility effects in the gas due to smallness of Ma numbers. This assumption is valid along the y direction as we will see from compressible flow simulations.

In fact, the current chapter serves as a preliminary step to accomplish linear stability analysis. Thus, base motions of the convection have been characterized via asymptotic analysis, and next step will be examination of the stability of the thermally driven convection.

4. STABILITY OF RAREFIED GAS FLOW IN ENCLOSURES

Heat transfer to rarefied gases produces mainly three types of motions. In the first one, the motion is primarily induced by buoyancy forces resulting from temperature differences between the bottom and top boundaries. This phenomenon has been widely studied by many researchers under the heading of Rayleigh-Bénard instability. In the second category, the flow is generated by thermally driven surface motion which is the main subject of the current study and especially in the closed domains, it still requires much effort. The third branch of flow is realized dominantly in case of negligible gravity conditions. In this mechanism which is so called *thermal stress flow*, a flow starts to evolve in time due to thermal stresses even in the absence of any external force, such as pressure, magnetic field, etc.

Recently, Rayleigh-Bénard convection has been gathered much attention due to not only lack of sufficient knowledge about the behavior of rarefied gas instabilities but also there is a necessity of proving whether DSMC methods work well in the continuum flow regime or not. Golshtein *et al.* (1996) have pointed out that Boussinesq approximation becomes invalid when the temperature difference between the bottom (T_h) and top (T_c) plate is high enough, and only Rayleigh number can not determine the limit of the instabilities. Stefanov *et al.* (2002a) have investigated the long-time behavior of the Rayleigh-Bénard convection of a rarefied gas for varying Kn and Froude (Fr) numbers. Both DSMC and direct simulation of NS equations have been performed to identify the zone of instabilities within the $Kn - Fr$ parameter space. Although, solutions of both methods constitute well within the wide range of Kn and Fr numbers, they have stressed a discrepancy on the basic state solutions of one dimensional density profile found by these two totally different methods. According to Stefanov *et al.* (2002a), this difference can be attributed to the lack of higher-order terms of Chapman-Enskog expansion in the NS equations. In the second report of Stefanov *et al.* (2002b), new regimes and final states of Bénard convection have been referred. Hirano *et al.*

(2002) have compared solutions of DSMC and NS simulations in the Rayleigh-Bénard convection for $Kn = 0.029$, $Kn = 0.01$ and $Kn = 0.005$ for Rayleigh number, $Ra = 2990$. They have noticed a close similarity between both simulations as Kn number decreases and goes to continuum flow limits. However, they have not included the effect of velocity slip and temperature jump on modeling. Recently, Manela *et al.* (2005) have studied on the linear-stability of compressible Rayleigh-Bénard convection in the slip flow regime. According to their findings, realization of instability is limited to small $Kn \leq 0.03$ numbers. Both temperature dependency of thermo-physical parameters and compressibility effects have been taken into account in the modeling. They have reported close constitution between the linear stability analysis and DSMC on the threshold of the instability. Sone *et al.* (1997) have studied Bénard instability on the basis of finite difference representation of Boltzmann-Krook-Welander equation (BGK model). They have discussed effects on initial condition and aspect ratio of the domain on the type of steady convection rolls.

In the third category, thermal stresses are capable of initiating a flow from rest and principally originate from thermal gradient terms embedded in the Burnett momentum equations. However, thermal stress flow can not be observed by making use of NS equations due to absence of higher-order terms Burnett equations' have. According to Golshtein *et al.* (1996), magnitudes of velocities resulting from thermal stresses may be sufficiently high if the temperature difference between the walls is large. They have also observed cellular flow structures between the plane and wavy patterned surfaces for $T_c \ll T_h$, see pages 255-256 of Golshtein *et al.* (1996). Although, the mentioned flow is slightly different from our proposed flow instability, occurrence of such an motion straightens our hypothesis. Another study regards the effect of thermal stresses on the pressure gradient and normal stress in a stationary, hard-sphere gas under no body and external forces conditions (Mackowski *et al.* 1999). Additionally, Sone (2000) has been reported that the thermal stress produces steady flow even in the *limit of continuum* flow and given some examples exhibiting such a mechanism. Moreover, Sone *et al.* (2003) have considered Bénard convection under the weak gravity conditions. Definitely, NS equations don't pose any thermal convection due to lack of gravity. However, solution of Boltzmann system presents strong fluctuations of temperature

even in the infinitesimal velocity and gravity conditions (Sone *et al.*, 2003). They have stressed insufficiency of the NS system in the continuum limit as well.

Notice that, occurrence of thermal stress flow even for $Kn \leq 0.01$ exposes inadequacy of NS equations and so use of Burnett equations becomes indispensable. This is the reason why the Burnett equations have been chosen as a mathematical model in the present study.

In this study, linear stability theory will be exploited to clear possible unstable behavior of rarefied gas media. In the next section, basic theory of the linear stability theory will be given.

4.1. Theoretical Background of Hydrodynamic Stability

4.1.1. Stability in the Small

Suppose that an incompressible and Newtonian fluid, subjected to a body force of $\mathbf{f}(\mathbf{r}, t)$, flows in a domain of $\Omega \subset R^3$. Such a viscous flow is simply governed by non-dimensional NS system

$$\text{div } \mathbf{u} = 0, \tag{4.1}$$

$$\frac{\partial \mathbf{u}}{\partial t} + (\mathbf{u} \cdot \text{grad})\,\mathbf{u} = \mathbf{f} + \text{grad } p + \frac{1}{Re}\nabla^2 \mathbf{u}, \tag{4.2}$$

with initial condition,

$$\mathbf{u}(\mathbf{r}, 0) = \mathbf{u}_0(\mathbf{r}, 0), \tag{4.3}$$

and the boundary condition

$$\mathbf{u}\big|_{\partial\Omega} = \mathbf{U}, \tag{4.4}$$

where $\mathbf{r} = (x, y, z)^{tr}$ and $\mathbf{u}(\mathbf{r}, t) = (u, v, w)^{tr}$ are the position and velocity vectors in the domain Ω, respectively. Notice that, variations in initial conditions, boundary conditions, the body force and physical parameters produce infinite number of distinct problems. However, by keeping all conditions and parameters constant except initial conditions, the flow problem can be converted to the study of the perturbations acting on the initial condition at the initial time only. Thus, the problem will become purely initial condition dependent. Therefore, consider a motion which is also called basic motion and modeled by

$$\text{div } \bar{\mathbf{u}} = 0 \tag{4.5}$$

$$\frac{\partial \bar{\mathbf{u}}}{\partial t} + (\bar{\mathbf{u}} \cdot \text{grad})\, \bar{\mathbf{u}} = \mathbf{f} - \text{grad } \bar{p} + \frac{1}{Re}\nabla^2 \bar{\mathbf{u}}, \tag{4.6}$$

the initial condition,

$$\bar{\mathbf{u}}(\mathbf{r}, 0) = \bar{\mathbf{u}}_0(\mathbf{r}, 0), \tag{4.7}$$

and the boundary condition,

$$\bar{\mathbf{u}}\big|_{\partial\Omega} = \mathbf{U}, \tag{4.8}$$

Assume that the basic field is subjected to the perturbations of $(\mathbf{u_0'}, p_0')$ at the initial moment. Thus, the initial conditions of the flow, Equation 4.3, will be a composition of the initial condition of the basic motion and its perturbation

$$\mathbf{u}_0 = \bar{\mathbf{u}}_0 + \mathbf{u_0'}.$$

Analogously, the sum of basic states and their perturbations forms the perturbed flow such that

$$\mathbf{u} = \bar{\mathbf{u}} + \mathbf{u}', \quad p = \bar{p} + p'.$$

If the basic motion is disturbed slightly, the disturbance may either be killed, survives as a disturbance of similar magnitude or grows so much that the basic flow converts to a different state, such as another laminar flow or turbulent flow. In other words, such disturbances may be *asymptotically stable*, *neutrally stable* or *unstable*, respectively (Drazin *et al.*, 1993). Formal definition is given in the following statement (Georgescu, 1985).

Definition 4.1. *The solution* $\bar{\mathbf{u}}$ *is said to be* ***stable in the small*** *if for every* $\epsilon > 0$ *there exists* $\eta(\epsilon)$ *such that* $\sup_{x,t} |\mathbf{u}(\mathbf{x},t) - \bar{\mathbf{u}}(\mathbf{x},t)| < \epsilon$ *for* $\sup_{x} |\mathbf{u}_0(\mathbf{x}) - \bar{\mathbf{u}}_0(\mathbf{x})| < \eta(\epsilon)$*;* $\bar{\mathbf{u}}$ *is said to be* ***asymptotically stable in the small*** *if it is stable in the small and* $\lim_{t\to\infty} |\mathbf{u}(\mathbf{x},t) - \bar{\mathbf{u}}(\mathbf{x},t)| = 0$

Here the "sup" operator designates positive definite norm of any quantity. Hydrodynamic stability does not focus on time evolution of the initial disturbance, and it gives the effect of physical parameters at which the instability initiates. Notice that an important parameter, Re number, determines the faith of the flow such that for small values of it, the problem of Equations 4.1-4.4 admits unique and stable basic solution $\bar{\mathbf{u}}$. Let's consider a Re_G number at which the basic flow passes from stable state to one of the states: "pure instability" or "instability by steps —neutral instability". In case of "pure instability", the perturbations grow and the flow becomes turbulent when $Re \geq Re_G$ as $t \to \infty$. On the other hand, the flow structure changes to a new laminar basic motion, $\bar{\mathbf{u}}_1$, as $t \to \infty$ for the case of "instability by steps". This intermediate step lasts until reaching the new critical level of Re'_G at which $\bar{\mathbf{u}}_1$ becomes unstable and this process continues consecutively. Re'_G is a bifurcation point where the stability is lost. Consequently the solution will not be unique at this point.
Substraction of Equations 4.5-4.8 from the perturbed state, Equations 4.1-4.4 result in an initial-value problem for the perturbation to velocity vector

$$\frac{\partial \mathbf{u}'}{\partial t} + (\bar{\mathbf{u}} \cdot \text{grad})\,\mathbf{u}' + (\mathbf{u}' \cdot \text{grad})\,\bar{\mathbf{u}} + (\mathbf{u}' \cdot \text{grad})\,\mathbf{u}' = -\text{grad}\ p' + \frac{1}{Re}\nabla^2 \mathbf{u}', \tag{4.9}$$

$$\mathbf{u}'(\mathbf{x},0) = \mathbf{u}'_0 \tag{4.10}$$

which is differentiable and continuous class of solenoidal functions, (div $\mathbf{u}' = 0$), vanishing on the boundary $\partial\Omega$. So, the null vector of solution represents the basic flow state. Generally, the global existence for solutions of perturbations and basic state flows can be found only by use of some Hilbert spaces H, such as the perturbation vector $\mathbf{u}'$, or spatial change of it, grad $\mathbf{u}'$. For example; a flow is stable if any one of the conditions

$$\int_\Omega |\mathbf{u}'|^2 \, dx \to 0 \quad \text{if } t \to \infty,$$

$$\int_\Omega |\operatorname{grad} \mathbf{u}'|^2 \, dx \to 0 \quad \text{if } t \to \infty$$

become valid. The first condition represents energy of fluctuations and corresponds to a kind of stability in the large which is called as *stability in the mean*. The second condition enforces negligible gradient of the large perturbations and more stiff than the instability in the small which is only related to the velocities. The generalized solutions corresponding to bounded velocities and their gradients not only give basic state solutions but also permit to study transition stages of the flow.

4.1.2. Stability in the Mean

Equations 4.9 and 4.10 (difference motions: in fact the perturbation velocity equals to the difference between the perturbed velocity and basic velocity fields) representing basically the balance between the diffusion and convection of perturbations, construct complete set by introducing solenoidality condition —in reality continuity of perturbed velocities— and zero perturbation on the boundary, $\partial\Omega$

$$\operatorname{div} \mathbf{u}' = 0, \tag{4.11}$$

$$\mathbf{u}'\big|_{\partial\Omega} = 0. \tag{4.12}$$

Assuming the volume Ω is bounded (otherwise periodicity condition is assumed with respect to $\mathbf{x}$) one can get perturbation energy multiplying Equation 4.9 by $\mathbf{u}'$ and then integrating over the flow domain of Ω

$$\frac{d}{dt}\int_\Omega \frac{|\mathbf{u}'|^2}{2}\,dx + \int_\Omega (\bar{\mathbf{u}}\cdot \text{grad})\,\mathbf{u}'\cdot\mathbf{u}'\,dx + \int_\Omega (\mathbf{u}'\cdot \text{grad})\,\bar{\mathbf{u}}\cdot\mathbf{u}'\,dx$$

$$+\int_\Omega (\mathbf{u}'\cdot \text{grad})\,\mathbf{u}'\cdot\mathbf{u}'\,dx = -\int_\Omega \mathbf{u}'\,\text{grad}\ p'\,dx + \tag{4.13}$$

$$\frac{1}{Re}\int_\Omega \nabla^2\mathbf{u}'\cdot\mathbf{u}'$$

For selenoidal vectors $\mathbf{u'}_1$ the vectorial identity of div $(\mathbf{u'}_1\ \Phi) = \mathbf{u'}_1\ \text{grad}\ \Phi + \Phi\ \text{div}\ \mathbf{u'}_1$ converts to div $(\mathbf{u'}_1\ \Phi) = \mathbf{u'}_1\ \text{grad}\ \Phi$ which can be written in another form by remembering Gauss's theorem

$$\int_\Omega \mathbf{u'}_1\ \text{grad}\,\Phi\,dx = \text{div}\ (\mathbf{u'}_1\ \Phi)\,dx$$

$$= \int_{\partial\Omega} \mathbf{u'}_1\Phi\mathbf{n}\ dA$$

where Φ denotes any scalar function. No perturbation condition of $\mathbf{u'}_1|_{\partial\Omega} = 0$ sets the above equation as

$$\int_\Omega \mathbf{u'}_1\ \text{grad}\,\Phi\,dx = 0 \tag{4.14}$$

Considering the equalities of $(\bar{\mathbf{u}}\cdot\text{grad})\,\mathbf{u}'\cdot\mathbf{u}' = \bar{\mathbf{u}}\cdot\text{grad}\,\frac{|\mathbf{u}'|^2}{2}$, $(\mathbf{u}'\cdot\text{grad})\,\mathbf{u}'\cdot\mathbf{u}' = \mathbf{u}'\cdot\text{grad}\,\frac{|\mathbf{u}'|^2}{2}$ and Equation 4.14 encourages the following relations

$$\begin{aligned}\int_\Omega (\bar{\mathbf{u}}\cdot\text{grad})\mathbf{u}'\cdot\mathbf{u}'\,dx &= \int_\Omega (\mathbf{u}'\cdot\text{grad})\mathbf{u}'\cdot\mathbf{u}'\,dx \\ &= \int_\Omega \mathbf{u}'\cdot\text{grad}\ p'\,dx.\end{aligned} \tag{4.15}$$

Viscous term of the Equation 4.13 turns out to be

$$\int_\Omega \nabla^2\mathbf{u}'\cdot\mathbf{u}'\,dx = -\int_\Omega |\,\text{grad}\ \mathbf{u}'|^2\,dx$$

where

$$|\,\text{grad}\ \mathbf{u}'|^2 = \sum_{1\le i,j\le 3}\frac{\partial u_i'}{\partial x_j}\frac{\partial u_i'}{\partial x_j}.$$

Thus, Equation 4.13 modifies to the famous *Reynolds-Orr* energy equation by accounting also Equation 4.15

$$\frac{d}{dt}\int_\Omega \frac{|\mathbf{u}'|^2}{2}\,dx = -\int_\Omega (\mathbf{u}'\cdot\text{grad})\bar{\mathbf{u}}\cdot\mathbf{u}'\,dx - \frac{1}{Re}\int_\Omega |\,\text{grad}\ \mathbf{u}'|^2\,dx \tag{4.16}$$

The first term on the right hand side of Equation 4.16 is decomposed into a vectorial identity of $(\mathbf{u}'\cdot\text{grad})\bar{\mathbf{u}}\cdot\mathbf{u}' = \text{div}[(\bar{\mathbf{u}}\cdot\mathbf{u}')\cdot\mathbf{u}'] - (\mathbf{u}'\cdot\text{grad})\mathbf{u}'\cdot\bar{\mathbf{u}}$. Integration of this relation by considering Gauss's theorem and Equation 4.12 yields

$$\int_\Omega (\mathbf{u}'\cdot\text{grad})\bar{\mathbf{u}}\cdot\mathbf{u}'\,dx = -\int_\Omega (\mathbf{u}'\cdot\text{grad})\mathbf{u}'\cdot\bar{\mathbf{u}}\,dx.$$

Thus, *Reynolds-Orr* equation is reorganized as

$$\frac{d}{dt}\int_\Omega \frac{|\mathbf{u}'|^2}{2}\,dx = \int_\Omega (\mathbf{u}'\cdot\text{grad})\mathbf{u}'\cdot\bar{\mathbf{u}}\,dx - \frac{1}{Re}\int_\Omega |\,\text{grad}\ \mathbf{u}'|^2\,dx \tag{4.17}$$

Notice that first term of the Equation 4.17 designates time rate change of the mean energy of the perturbations. So, let's label such an important quantity as

$$K(t) = \int_{\Omega} \frac{|\mathbf{u}'|^2}{2}\, dx$$

Definitely, the first term of the right hand side of Equation 4.17 represents the quantity of energy transporting from basic state to perturbed state and the second term designates energy smeared by viscous diffusion. In fact, rearranged *Reynolds-Orr* equation is nothing more than the energy balance between the time rate change of mean energy of perturbations and the competition between the energy transfer to the perturbations from basic state and dissipation due to viscous dissipation.

Definition 4.2. *The basic motion* $\bar{\mathbf{u}}$ *is said to be* ***stable in the mean*** *to the perturbations of the initial conditions, if the mean energy of the perturbations* $\mathbf{u}'$*, solution of Equations 4.9-4.10 remains bounded for every* $t \geq 0$*;* $\bar{\mathbf{u}}$ *is said to be* ***asymptotically stable in the mean*** *if* $K(t) \to 0$ *as* $t \to \infty$*.*

Definition 4.2 exhibits sufficient condition for *the stability in the mean* such that

$$\frac{dK(t)}{dt} < 0, \quad \text{for} \quad t > 0. \tag{4.18}$$

The methodology modeled by Equations 4.9-4.12 (equations of difference motions) is called as *energy method* and it refers only bounds of the stability but does not point out exact limits of the stability. See discussions about this topic in page 24 of Georgescu (1985) and page 424 of Drazin *et al.* (1993). Due to non-linear nature of the equations of difference motions, an assumption of infinitesimally small perturbations eliminates insolvability restriction of Equations 4.9-4.12 and details of the procedure will be given in Section 4.2. A closer look into Equation 4.17 reveals sufficient condition for the stability of the basic motion

$$\frac{-\int_{\Omega} (\mathbf{u}' \cdot \operatorname{grad}) \bar{\mathbf{u}} \cdot \mathbf{u}'\, dx}{\frac{1}{Re} \int_{\Omega} |\operatorname{grad} \mathbf{u}'|^2\, dx} < 1$$

which is derived from the requirements of $\frac{dK}{dt} < 0$

4.1.3. Linear Stability Theory

Equations of difference motion either preserves its non-linearity for finite perturbations or simplifies to a linear form in case of infinitesimally small disturbances. Neglecting powers of infinitesimally small fluctuations allows us to study in the framework of *linear theory of hydrodynamic stability*. Thus, equations of difference motion is reduced to equations of linearized hydrodynamic stability.

$$\frac{\partial \mathbf{u}'}{\partial t} + (\bar{\mathbf{u}} \cdot \text{grad})\mathbf{u}' + (\mathbf{u}' \cdot \text{grad})\bar{\mathbf{u}} = -\text{grad}\ p' + \frac{1}{Re}\nabla^2 \mathbf{u}', \tag{4.19}$$

$$\mathbf{u}'(\mathbf{x}, 0) = \mathbf{u}'_{\mathbf{0}} \tag{4.20}$$

Definitely, this initial-value problem can be separable into some functions and the perturbations can be expressed as a superposition of the product of these functions such that $\mathbf{u}'(\mathbf{x}, t) = \mathbf{u}'_{\mathbf{0}}(\mathbf{x})e^{-\sigma t}$ which is called as *normal modes*, where complex number of σ is an eigenvalue representing propagation of perturbation waves in time and $\mathbf{u}'_{\mathbf{0}}$ is an eigenvector of the initial-value problem. Thus, substitution of the normal mode formulation to the mathematical model of the linear stability yields

$$-\sigma \mathbf{u}'_{\mathbf{0}} + (\bar{\mathbf{u}} \cdot \text{grad})\mathbf{u}'_{\mathbf{0}} + (\mathbf{u}'_{\mathbf{0}} \cdot \text{grad})\bar{\mathbf{u}} = -\text{grad}\ p'_0 + \frac{1}{Re}\nabla^2 \mathbf{u}'_{\mathbf{0}}, \tag{4.21}$$

$$\mathbf{u}'_{\mathbf{0}}|_{\partial\Omega} = 0. \tag{4.22}$$

Note also that $\mathbf{u}'_{\mathbf{0}}$ is solenoidal function.

Definition 4.3. *The basic motion of* $\bar{\mathbf{u}}$ *is* ***linearly asymptotically stable****, if the system of Equations 4.21 and 4.22 has no eigenvalue with negative real part. The basic flow becomes* ***asymptotically unstable*** *if at least one eigenvalue with negative real part is an eigenvalue of the problem. The flow is neutrally or marginally stable if there exists at least an eigenvalue with only imaginary part, the rest of the eigenvalues may have positive or vanishing real parts.*

Clearly, Re number which is the most important parameter of the problem directly determines the direction of being stable or not. The Re number in which at least one eigenvalue with negative reel part exists, corresponds to critical Re number and this level is also known as *bound of linear stability*. If any value of σ corresponds to a certain value of Re number, this matching is expressed by $\xi_0(Re) = \inf \Re(\sigma)$. Analogously, the critical Re number is simply $\xi_0(Re_{cr}) = 0$ corresponding to neutral perturbations with $\Re(\sigma) = 0$.

If the flow domain is unbounded in one or two dimensions; the general procedure is keeping perturbations periodic and bounded in these directions such that

$$\mathbf{u}' = \mathbf{u}'_{\mathbf{0}}(y, z)e^{ik_x x - \sigma t}$$

or

$$\mathbf{u}' = \mathbf{u}'_{\mathbf{0}}(z)e^{i(k_x x + k_y y) - \sigma t}$$

where k_x and k_y are wave numbers in the x and y directions, respectively. In this case, the eigenvalue σ depends on not only Re number but also k_x and k_y. In fact, the main purpose of the linear theory is to correlate a relation between these numbers, such as $(k_x,\ Re)$ in two-dimensions or $(k_x,\ k_y,\ Re)$ in three-dimensions. At the planes of this parameters, domain of stability and instability are decomposed by neutral curves (or surfaces in three-dimensions) at which the instability grows up. So, it is important to find Re_{cr} values for each values of the other parameters.

4.1.4. Global Stability

In this section, the rate of mean perturbation energy $K(t)$ to $K(0)$ for varying Re number will be scrutinized. For the sake of brevity, we will introduce only the main conclusions of the global stability concept. Interested readers are referred to Georgescu (1985) for more details. Equation 4.17 can be rewritten in a different way by use of Serrin's theorem

$$\lim_{t \to \infty} \frac{K(t)}{K(0)} = 0. \tag{4.23}$$

The basic state $\bar{\mathbf{u}}$ is *attractive in the mean* if it satisfies Equation 4.23. A flow is asymptotically stable if it is stable and attractive. The basic state of $\bar{\mathbf{u}}$ is *globally stable* or *unconditionally stable* if Equation 4.23 is fulfilled for all values of $K(0)$. $\bar{\mathbf{u}}$ will become *conditionally stable* if Equation 4.23 holds only for $K(0) < \delta > 0$.

In the current study, we assume that the perturbations $\mathbf{u}'$ to the basic state are infinitesimally small and so linear stability theory will be applied through the Section 4.2.

4.2. Modeling

Let's consider circulation of rarefied gas in an enclosure with an aspect ratio as illustrated in Figure 3.2. While left side of the enclosure is maintained at temperature of T_c, the other side is kept at temperature of T_h, where $T_h > T_c$. Temperature gradient on the top wall is constant such that $b = \frac{dT}{dx} = constant,\ b > 0$. Thermal BC of the bottom surface directly affects characteristics of the stability as described by Priede *et al.* (1995). So, the following BCs are performed for temperature

1. Robin type in two-dimensional stability analysis
2. Neumann type in three-dimensional stability analysis.

For the first case, the temperature of the boundary varies linearly as the top one, $b = \frac{dT}{dx}$. The second case stands for adiabatic wall. It is clear that, there is a flow axisymmetry with respect to the centerline of the enclosure for the first case. For this reason, we will restrict the analysis for axisymmetric disturbances. According to the our experiences in two-dimensional stability analysis, there are some symmetry-breaking disturbances as well.

Once, suitable scales for non-dimensionalization are introduced, the governing equations in dimensionless form are formulated as

$$t^* = \frac{tu_0}{d}, \quad x^* = \frac{x}{d}, \quad y^* = \frac{y}{d},$$

$$u^* = \frac{u}{u_0}, \quad v^* = \frac{v}{u_0}, \quad \theta = \frac{T - T_c}{bd}, \quad p^* = \frac{p}{\mu_0 u_0/d}$$

continuity, momentum and energy equations:

$$\text{div } \mathbf{u} = 0 \tag{4.24}$$

$$Re\left[\frac{\partial \mathbf{u}}{\partial t} + (\mathbf{u}\cdot\text{grad})\,\mathbf{u}\right] = -\text{grad } p + \nabla^2\mathbf{u} \tag{4.25}$$

$$RePr\left[\frac{\partial \theta}{\partial t} + (\mathbf{u}\cdot\text{grad})\,\theta\right] = \nabla^2\theta. \tag{4.26}$$

where Re and Kn numbers are defined as

$$Re = \frac{3}{2\pi}\left(\frac{\gamma-1}{\gamma}\right)\frac{c_{p0}\rho_0^2 d^3 b}{\mu_0^2}, \quad Kn = \frac{\mu_0}{d\rho_0\sqrt{2RT_0/\pi}}$$

One important point to be discussed is that the order of magnitude of Re does not depend on ϵ. We set Re number to be $O(1)$. Such an approximation does not violate basic state solutions found by outer expansions in the preceding chapter.

4.3. Linearized Stability Analysis

Using the fact that instantaneous flow variables can be represented as a sum of basic motion solutions and small disturbances

$$\mathbf{u} = \bar{\mathbf{u}} + \mathbf{u}', \quad p = \bar{p} + p', \quad \theta = \bar{\theta} + \theta'.$$

Application of linearization process as described in Section 4.1.1 gives the following equations of disturbance motion

$$\text{div } \mathbf{u}' = 0, \tag{4.27}$$

$$Re\left[\frac{\partial \mathbf{u}'}{\partial t} + (\bar{\mathbf{u}} \cdot \text{grad})\mathbf{u}' + (\mathbf{u}' \cdot \text{grad})\bar{\mathbf{u}}\right] = -\text{ grad } p' + \nabla^2 \mathbf{u}', \tag{4.28}$$

$$RePr\left[\frac{\partial \theta'}{\partial t} + (\bar{\mathbf{u}} \cdot \text{grad})\theta' + (\mathbf{u}' \cdot \text{grad})\bar{\theta}\right] = \nabla^2 \theta' \tag{4.29}$$

As previously mentioned in Section 4.1.3, perturbations to the basic states of flow variables can be represented in normal mode forms given by

$$\begin{bmatrix} u' \\ v' \\ w' \\ p' \\ \theta' \end{bmatrix} = \begin{bmatrix} u'_0 \\ v'_0 \\ w'_0 \\ p'_0 \\ \theta'_0 \end{bmatrix} e^{i(k_x x + k_z z - \sigma t)} \tag{4.30}$$

where k_x and k_z are positive valued real numbers representing perturbation wave-numbers in the x and z directions, respectively. Here, σ is the complex eigenvalue of the system. Real part of the eigenvalue, $\Re(\sigma)$, denotes frequency of perturbation modes, ie. u'_0, v'_0, and the imaginary part of it, $\Im(\sigma)$, designates the temporal amplification rate of the perturbations. When $\Im(\sigma)$ is greater, equal to, or smaller than zero, a perturbation mode is unstable with temporal amplification, neutrally stable, or stable with finite damping, respectively (Hu *et al.*, 1998). The perturbation waves travel in a direction of $\phi = \arctan(k_z/k_x)$ with respect to the positive $x-$ axis and overall wave number is defined by, $k = \sqrt{k_x^2 + k_z^2}$. Complex wave (phase) velocity, c_R , of the perturbation waves is defined as $c_R = \sigma/k_x$. Note that, although, perturbation waves propagate in the space, a reduction to two-dimension may possible by ignoring k_x or k_z. Substitution of Equation 4.30 into Equations 4.27 - 4.29 results in normal mode equations

$$ik_x u'_0 + \mathrm{D}\, v'_0 + ik_z w'_0 = 0, \tag{4.31}$$

$$\{\mathrm{D}^2 - (k_x^2 + k_z^2) - ik_x Re\bar{u} + i\nu_r Pr^{-1}\}u_0' = ik_x p_0' + Rev_0' \,\mathrm{D}\,\bar{u}, \tag{4.32}$$

$$\{\mathrm{D}^2 - (k_x^2 + k_z^2) - ik_x Re\bar{u} + i\nu_r Pr^{-1}\}v_0' = \mathrm{D}\,p_0', \tag{4.33}$$

$$\{\mathrm{D}^2 - (k_x^2 + k_z^2) - ik_x Re\bar{u} + i\nu_r Pr^{-1}\}w_0' = ik_z p_0', \tag{4.34}$$

$$\{\mathrm{D}^2 - (k_x^2 + k_z^2) - ik_x RePr\bar{u} + i\nu_r\}\theta_0' = RePru_0'\bar{\theta}_x + RePrv_0'\bar{\theta}_y, \tag{4.35}$$

where $\mathrm{D} = d/dy$ and $\mathrm{D}^2 = d^2/dy^2$ are differential operators. Neutral conditions of the disturbances require setting the growth rate (complex part) of the eigenvalue of the system to zero. Thus, the remaining part the eigenvalue will only be the frequency of the perturbation modes,

$$\nu_r = RePr\sigma_r.$$

4.3.1. Reduction to Two-Dimensional Normal Mode Form

Normal mode equations of the problem, Equations 4.31 - 4.35, set coupled system of partial differential equations and requires a numerical approximation for the solution. On the other hand, a special case of $k_x = 0$, simplifies the system and allows finding an analytical solution. In this case, the continuity equation can be used to eliminate variables w_0' and p_0', Thus, the reduced system of equations can be rearranged as

$$\{\mathrm{L} + i\nu_r Pr^{-1}\}u_0' = Rev_0' \,\mathrm{D}\,\bar{u} \qquad \text{x-wise}, \tag{4.36}$$

$$\{\mathrm{L} + i\nu_r Pr^{-1}\}\,\mathrm{L}\,v_0' = 0 \qquad \text{y-wise}, \tag{4.37}$$

$$\{\mathrm{L} + i\nu_r\}\theta_0' = RePr\{u_0'\bar{\theta}_x + v_0'\bar{\theta}_y\} \qquad \text{energy}, \tag{4.38}$$

where the differential operator L is defined as $\mathrm{L} = \mathrm{D}^2 - k_z^2$. Next-section gives solution procedures for the linear stability equations.

4.4. Eigensystems in Two- and Three-Dimensions

This section brings forward solutions of both two- and three-dimensional normal mode equations. In the proceeding section, analytical solutions of normal mode equations in two-dimensions will be derived.

4.4.1. The Eigensystem for Axisymmetric Disturbances in Two-dimensions

Analytical solution of linear stability equations in two-dimensions gives valuable information about creation of instability mechanism. Effect of three second-order models (Cercignani, Deissler, Schamberg) and a first-order slip model (Maxwell) on the limits of the proposed instability have also been examined (see Table 2.1). The main purpose of the current section is to establish bounds of the instability and to examine effects of some important dimensionless numbers about instability. For this purpose, after solving v_0', u_0' and θ_0', neutral curves of instability will be found with the aid of characteristic equation as shown in Section 4.4.1.3. Illustration of the axisymmetric problem has been shown in Figure 4.1. Note that, dimensions of the enclosure has been

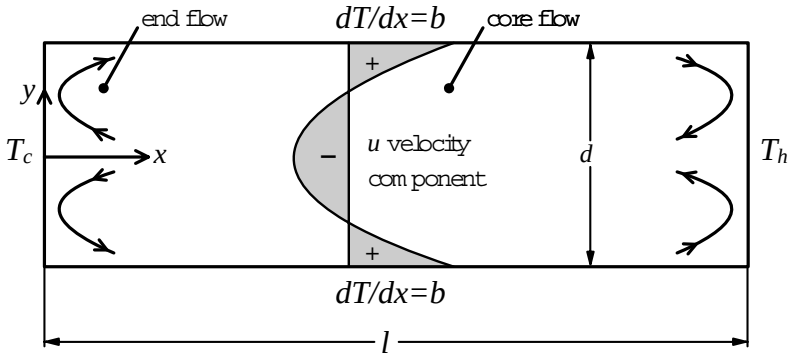

Figure 4.1. Geometry for the axisymmetric disturbances

scaled with half channel height of $d/2$. In this situation, disturbance equations can be

rearranged as,

$$\{\mathrm{L} + i\nu_r Pr^{-1}\} u_0' = Re_d v_0' \,\mathrm{D}\,\bar{u} \qquad \text{x-wise,} \tag{4.39}$$

$$\{\mathrm{L} + i\nu_r Pr^{-1}\} \,\mathrm{L}\, v_0' = 0 \qquad \text{y-wise,} \tag{4.40}$$

$$\{\mathrm{L} + i\nu_r\}\theta_0' = Re_d Pr\{u_0'\bar{\theta}_x + v_0'\bar{\theta}_y\}, \qquad \text{energy} \tag{4.41}$$

where $Re_d = Re/8$. Here ν_r modifies to $\nu_r = \sigma_r Re_d Pr$. Basic state for the axisymmetric case can be represented as the followings;

$$\bar{\mathbf{u}} = [u, v, w]^{tr} = \left[\frac{Kn^2}{2 + 6A_1 Kn - 6A_2 Kn^2}\left(3y^2 - 1\right), 0, 0\right]^{tr}$$

$$\bar{p}_x = \frac{6Kn^2}{2 + 6A_1 Kn - 6A_2 Kn^2}$$

$$\bar{\theta} = x + Re_d Pr\left\{\frac{Kn^2}{2 + 6A_1 Kn - 6A_2 Kn^2}\left[\frac{y^4}{4} - \frac{y^2}{2} + \frac{2\gamma}{\gamma + 1}\frac{8A_2 Kn^2 + 1}{4Pr}\right]\right\}. \tag{4.42}$$

After the introduction of basic states, disturbance equations of two-dimensional case, 4.39-4.41, will be solved analytically with the following boundary conditions:
on the centerline of the enclosure, $y = 0$;

$$\mathrm{D}\, u_0' = v_0' = \mathrm{D}^2\, v_0' = \mathrm{D}\,\theta_0' \tag{4.43}$$

on the top wall, $y = 1$;

$$u_0' + A_1 Kn_d \,\mathrm{D}\, u_0' - A_2 Kn_d^2 \,\mathrm{D}^2\, u_0' = 0, \tag{4.44}$$

$$v_0' = 0, \tag{4.45}$$

$$\mathrm{D}\, v_0' + A_1 Kn_d\, \mathrm{D}^2\, v_0' - A_2 Kn_d^2\, \mathrm{D}^3\, v_0' - Kn_d^2 k_z^2 \theta_0' = 0, \tag{4.46}$$

$$\theta_0' - \left(\frac{2\gamma}{\gamma+1}\right)\frac{1}{Pr}\left[-A_1 Kn_d\, \mathrm{D}\, \theta_0' + A_2 Kn_d^2\, \mathrm{D}^2\, \theta_0'\right] = 0, \tag{4.47}$$

where Kn_d is based on the half enclosure height and defined as $Kn_d = 2Kn$.

4.4.1.1. Solution of normal mode v equation. In order to advance in analytical solutions, v_0' equation should be solved at first. For this purpose, let's consider the equation of

$$(\mathrm{L} + i\nu_r Pr^{-1})\, \mathrm{L}\, v_0' = 0 \tag{4.48}$$

and related BCs

$$v_0'(0) = 0, \quad \mathrm{D}^2\, v_0'(0) = 0 \tag{4.49}$$

$$v_0'(1) = \mathrm{D}\, v_0'(1) + A_1 Kn_d\, \mathrm{D}^2\, v_0'(1) - Kn_d^2 k_z^2 \theta_0'(1) = 0. \tag{4.50}$$

In order to get a solution to the system of Equations 4.48-4.50, boundary values of θ_0' should be specified. If normal mode form of temperature on the top boundary is prescribed as

$$\theta_0'(1) = 1, \tag{4.51}$$

then v_0', u_0' and θ_0' can be solved subsequently. Under this circumstances, general solution for v_0' can simply be represented as a sum of exponential functions

$$v_0'(y) = Ae^{zy} + Be^{-zy} + Ce^{-k_z y} + De^{k_z y}, \tag{4.52}$$

where A, B, C and D are constants to be determined from BCs and complex number, z, is given by

$$z = \sqrt{\frac{Prk_z^2 - i\nu_r}{Pr}}.$$

Applications of BCs, Equations 4.49 and 4.50 yield;

$$A = \frac{A_n}{A_{d1} + 2\left(A_{d2} + A_{d3}\right)\sinh k_z},$$
$$A_n = Kn_d^2 k_z^2 \sinh k_z,$$
$$A_{d1} = 2k_z\left(A_2 k_z^2 Kn_d^2 - 1\right)\cosh k_z \sinh z,$$
$$A_{d2} = \left(z - A_2 z^3 Kn_d^2\right)\cosh z,$$
$$A_{d3} = A_1 Kn\left(z^2 - k_z^2\right)\sinh z,$$

$$-C = D = B = -A.$$

4.4.1.2. Solution of normal mode u equation. After finding the solution of v_0', let's consider the u_0' equation;

$$\left(\mathrm{L} + i\nu_r Pr^{-1}\right) u_0' = Re_d v_0' \,\mathrm{D}\,\bar{u} \tag{4.53}$$

with the boundary conditions,

$$\mathrm{D}\,u_0'(0) = u_0'(1) + A_1 Kn_d\,\mathrm{D}\,u_0'(1) - A_2 Kn_d^2\,\mathrm{D}^2\,u_0'(1) = 0 \tag{4.54}$$

where

$$\mathrm{D}\,\bar{u} = \frac{6Kn^2}{2 + 6A_1 Kn - 6A_2 Kn^2} y.$$

General solution of Equation 4.53 is represented as the sum of particular and homogeneous solutions,

$$u_0'(y) = Ee^{zy} + Fe^{-zy} + u_{0_p}'(y) \tag{4.55}$$

where E and F are coefficients to be determined from the BCs of u_0' and u_{0_p}' corresponds to particular solution. These coefficients are calculated as

$$\begin{aligned}
E &= \frac{E_{n1} + E_{n2}}{E_d}, \\
E_{n1} &= u_{0_p}'(1) + Kn_d(A_1 \,\mathrm{D}\, u_{0_p}'(1) - A_2 Kn_d \,\mathrm{D}^2\, u_{0_p}'(1))z, \\
E_{n2} &= -\,\mathrm{D}\, u_{0_p}'(0)(Kn_d z(A_1 + A_2 Kn_d z) - 1)e^{-z}, \\
E_d &= 2z((A_2 z^2 Kn_d^2 - 1)\cosh z - A_1 z Kn_d \sinh z),
\end{aligned}$$

$$\begin{aligned}
F &= \frac{F_{n1} + F_{n2}}{F_d}, \\
F_{n1} &= u_{0_p}'(1) + Kn_d(A_1 \,\mathrm{D}\, u_{0_p}'(1) - A_2 Kn_d \,\mathrm{D}^2\, u_{0_p}'(1))z, \\
F_{n2} &= \mathrm{D}\, u_{0_p}'(0)(Kn_d z(A_2 Kn_d z - A_1) - 1)e^{z}, \\
F_d &= 2z((A_2 z^2 Kn_d^2 - 1)\cosh z - A_1 z Kn_d \sinh z).
\end{aligned} \tag{4.56}$$

4.4.1.3. Solution of normal mode energy equation. The governing equation and the BCs of θ_0' are rewritten as

$$(\mathrm{L} + i\nu_r)\,\theta_0' = Re_d Pr\left[u_0'\bar{\theta}_x + v_0'\bar{\theta}_y\right], \tag{4.57}$$

$$\mathrm{D}\,\theta_0'(0) = \theta_0'(1) - \frac{2\gamma}{\gamma+1}\frac{1}{Pr}\left[-Kn_d \,\mathrm{D}\,\theta_0'(1) + A_2 Kn_d^2 \,\mathrm{D}^2\,\theta_0'(1)\right] = 0 \tag{4.58}$$

Lastly, the normal mode representation of temperature is expressed as a sum of

$$\theta_0' = Ge^{z_1 y} + He^{-z_1 y} + \theta_{0_p}'(y) \tag{4.59}$$

where z_1 is calculated as

$$z_1 = \sqrt{k_z^2 - i\nu_r},$$

and θ'_{0_p} designates particular solution of the Equation 4.59. Implementation of BCs, Equation 4.58 gives constants G and H;

$$\begin{aligned}
G &= \frac{G_{n1} + G_{n2}}{G_d}, \\
G_{n1} &= u'_{0_p}(1) + c_\theta Kn_d(A_1 \,\mathrm{D}\, u'_{0_p}(1) - A_2 Kn_d \,\mathrm{D}^2\, u'_{0_p}(1))z, \\
G_{n2} &= -\,\mathrm{D}\, u'_{0_p}(0)(c_\theta Kn_d z(A_1 + A_2 Kn_d z) - 1)e^{-z}, \\
G_d &= 2z((c_\theta A_2 z^2 Kn_d^2 - 1)\cosh z - c_\theta A_1 z Kn_d \sinh z),
\end{aligned}$$

$$\begin{aligned}
H &= \frac{H_{n1} + H_{n2}}{H_d}, \\
H_{n1} &= u'_{0_p}(1) + c_\theta Kn_d(A_1 \,\mathrm{D}\, u'_{0_p}(1) - A_2 Kn_d \,\mathrm{D}^2\, u'_{0_p}(1))z, \\
H_{n2} &= \mathrm{D}\, u'_{0_p}(0)(c_\theta Kn_d z(A_2 Kn_d z - A_1) - 1)e^{z}, \\
H_d &= 2z((c_\theta A_2 z^2 Kn_d^2 - 1)\cosh z - c_\theta A_1 z Kn_d \sinh z),
\end{aligned} \tag{4.60}$$

where $c_\theta = \frac{2\gamma}{\gamma+1}\frac{1}{Pr}$.

The solution of θ'_0 can be expressed in terms of a complex function such that

$$\theta'_0 = (Re)^2 f\left[y; \nu_r, k_z, Pr, Kn, \gamma\right], \tag{4.61}$$

where $f = f_r + i f_i$. Real valued prescription of θ'_0 on the top boundary, Equation 4.51 requires setting

$$\Im f\left[1; \nu_r, k_z, Pr, Kn, \gamma\right] = 0. \tag{4.62}$$

This equation is the characteristic equation for the eigenvalue ν_r. The root ν_r has been determined numerically by use of `bisection method`, for other varying parameters.

Subsequently, the critical values of Re forming neutral curves are detected from

$$Re = \Re f\left[1; \nu_r, k_z, Pr, Kn, \gamma\right]^{-\frac{1}{2}}. \tag{4.63}$$

Thus, corresponding eigenvalue σ_r is simply determined from

$$\sigma_r = \frac{\nu_r}{RePr}.$$

Note that all mathematical simplifications during the solution process of normal mode equations are accomplished by MATHEMATICA®.

4.4.2. Results and Discussions for Two-Dimensional Case, ($k_x = 0$)

In this section we will introduce neutral and critical states of some second-order slip models i.e. Cercignani, Deissler and Schamber, and a first-order slip model i.e. Maxwell. Critical states for the mentioned slip modes are summarized in Table 4.1. The critical states are approximately the same for all second-order slip models. On the other hand, there is a increase in the $(Re_d)_{cr}$ for increasing second order slip coefficient A_2 as inspected from Deissler and Schamber models. Although, A_2 of Cercignani models is greater than Deissler and Schamberg, its first-order coefficient A_1 leads to highest critical Re_d number among the second-order models. Maxwell model gives the stronger stability threshold due to vanishing A_2. Since the flow is totally generated by thermal transpiration and a significant velocity slip takes place on the boundaries depending on Kn, Re and Pr numbers, behavior of slip perturbations will be very important for

Table 4.1. Eigenvalues and corresponding critical values of slip models for $Kn = 0.40$ and $Pr = 0.70$

Slip model	ν_r	$(k_z)_{cr}$	$(Re_d)_{cr}$
Cercignani	3.07	0.76	181.584
Deissler	2.78	0.74	178.670
Maxwell	36.15	1.53	429.238
Schamberg	2.56	0.72	186.345

the current flow type. Because of the fact that the proposed flow originates from the temperature variations along the surfaces bounding the rarefied gases, looking at the temperature fluctuations on the boundaries will be a nice starting point. In Figure 4.2 real parts of the temperature perturbations are shown for different models. Notice

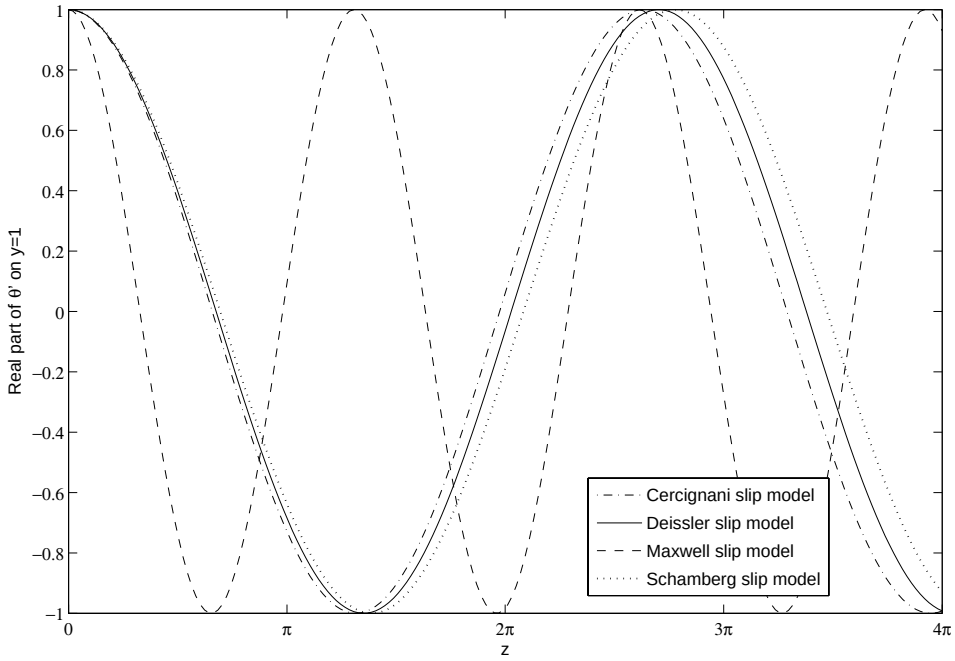

Figure 4.2. Real part of the temperature perturbations for different slip models with $Pr = 0.70$ and $Kn = 0.40$ at $t = 1/\sigma_r$

that a wave shift takes place for each model. Maxwell models shows the greatest shift compared with the others due to relatively large wave number of $(k_z)_{cr}$. Since critical wave numbers of all second-order models are approximately the same, wave shifts of all those also approach to each other. Perturbations of the temperature are illustrated in Figure 4.5 with increasing dominance as approaching axisymmetry plane of the enclosure. The strongest perturbations are observed starting from $y \cong 0.52$ and take extreme values on the centerline. To illustrate surface flow we show $\Re w_0'$ on $y = 1$ (Figure 4.3). Maxwell model creates the highest wave amplitude. Again the other models have nearly the same wave amplitudes. Maximums and minimums of all models take place at different locations as well. The important point to be discussed at this stage that although Maxwell model leads to the highest wave speeds on the top surface, its stability threshold shows significant increases and takes higher values as compared

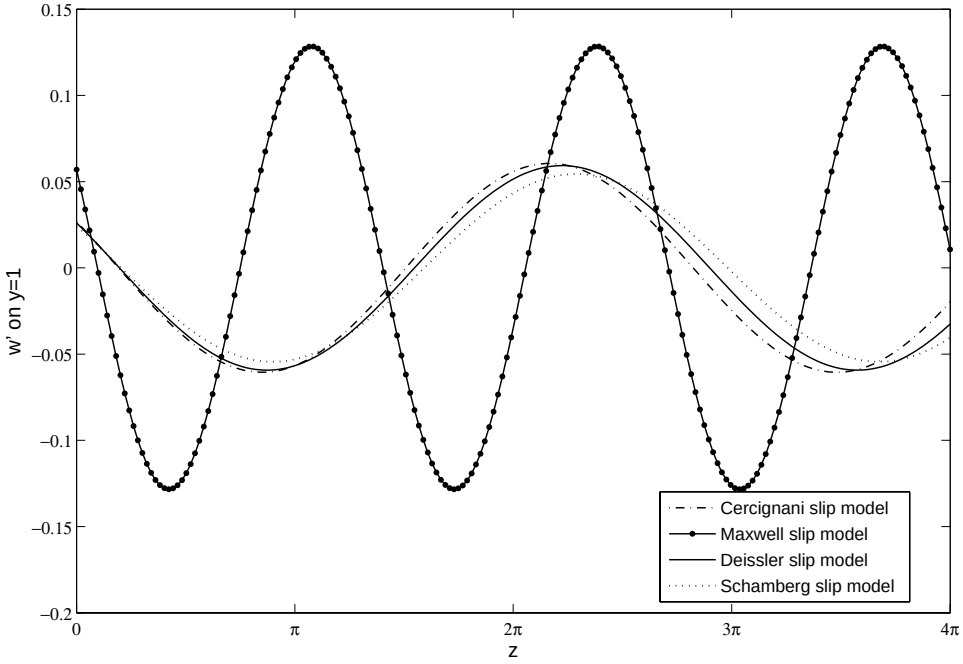

Figure 4.3. Real part of w_0' disturbances on $y = 1$ for various models with $Pr = 0.70$ and $Kn = 0.40$ at $t = 1/\sigma_r$

those of the other slip models. This observation is oppose to our expectations. If we totally ignore slip effect due to momentum accommodation, the slip on the surface will be proportional to $Kn_d^2\theta'(1)$ and then inserting $A_1 = 1.0$ corresponds to Maxwell models of which stability limits were the highest. If the second-order contribution of the momentum accommodation, $A_2 Kn_d^2 \,\mathrm{D}^2\, u_t'$, comes into effect, we observe reduction in critical Re number. More importantly, higher values of A_2 strengthen stability of the flow. This is the reason why the Maxwell models gives the highest amplitude. The disturbance waves of w' on the x plane are illustrated in Figure 4.4.

Disturbance flow created by thermal waves exhibits cellular patterns (Figure 4.7 and Figure 4.6). While the negative valued streamlines rotate clockwise direction, negative valued ones spin counter direction as well. Figure 4.8 shows variation of streamlines on the top plane of the enclosure. Notice that, Schamberg model gives the lowest value as compared the other second-order models. On the other hand, smallness of the values is a proof of zero net mass flow rate along the cross-section of the enclosure.

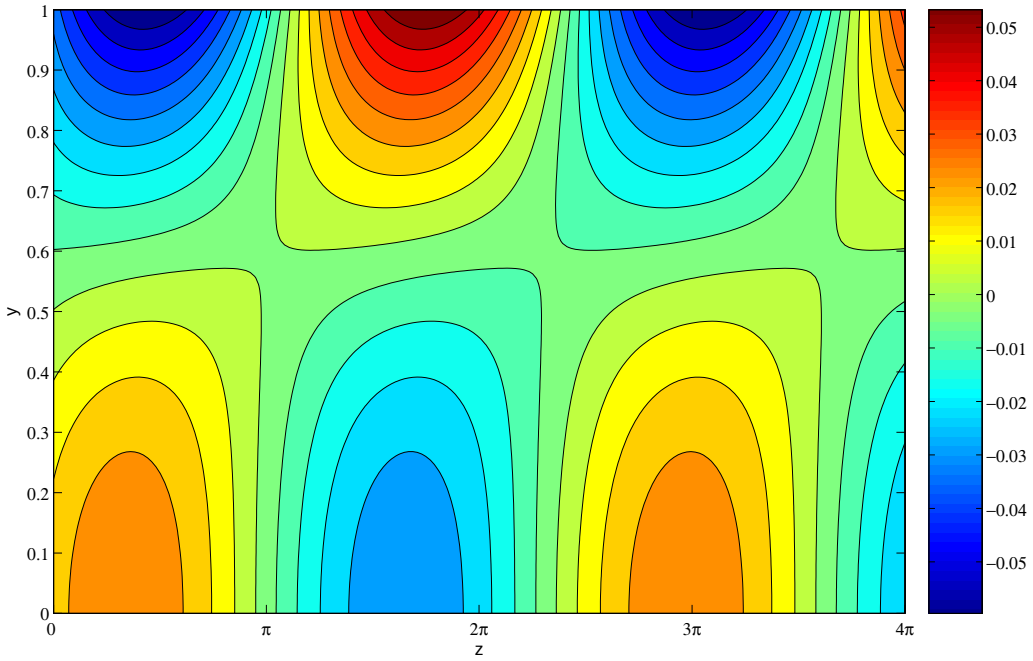

Figure 4.4. Real part of the w' perturbations on the $y - z$ plane for Cercignani model with $Pr = 0.70$ and $Kn = 0.40$ at $t = 1/\sigma_r$

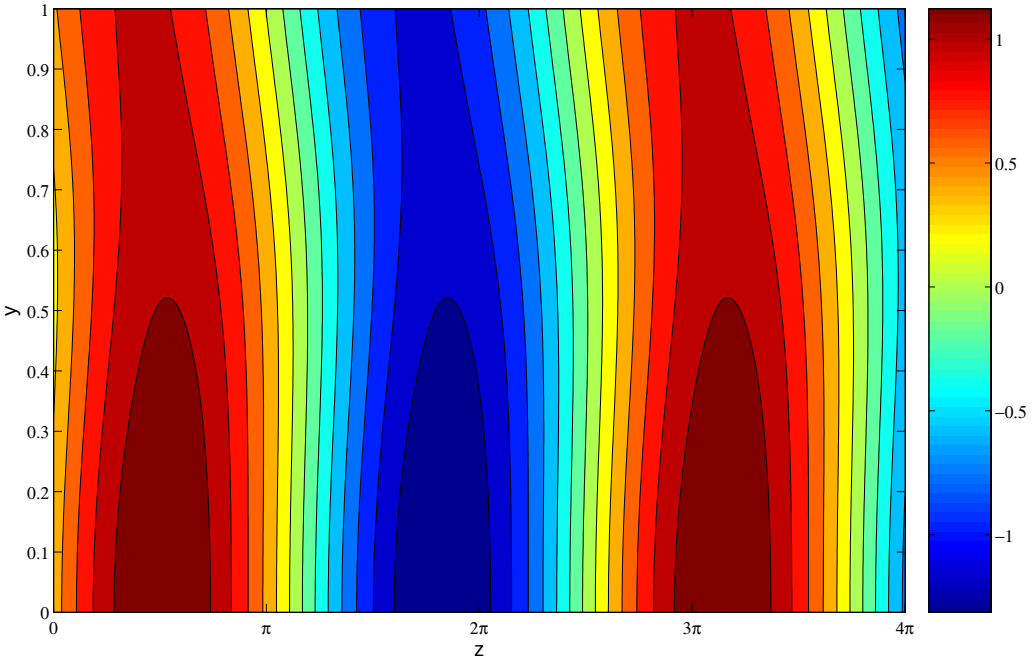

Figure 4.5. Real part of the temperature perturbations on the $y - z$ plane for Cercignani model with $Pr = 0.70$ and $Kn = 0.40$ at $t = 1/\sigma_r$

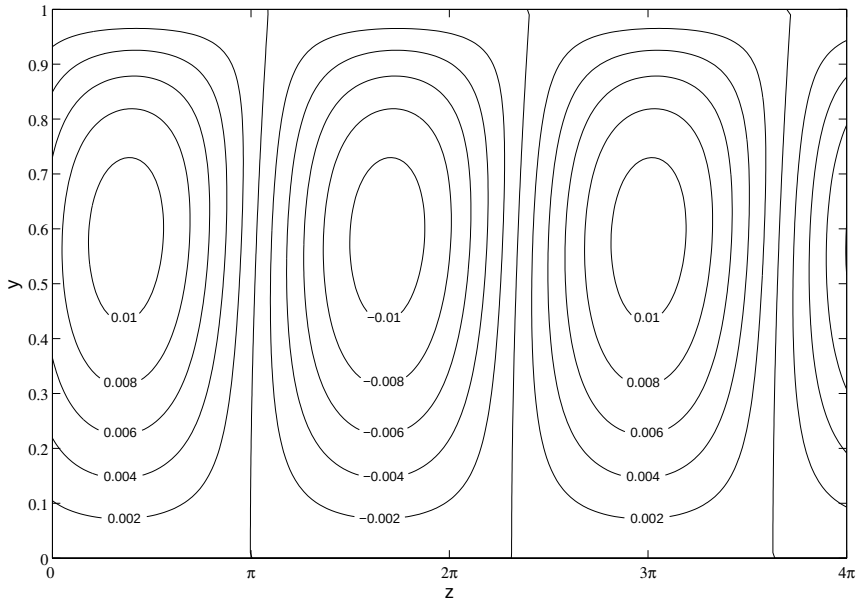

Figure 4.6. Real streamline disturbances on the x plane for Cercignani model, $Pr = 0.70$ and $Kn = 0.40$ at $t = 0$.

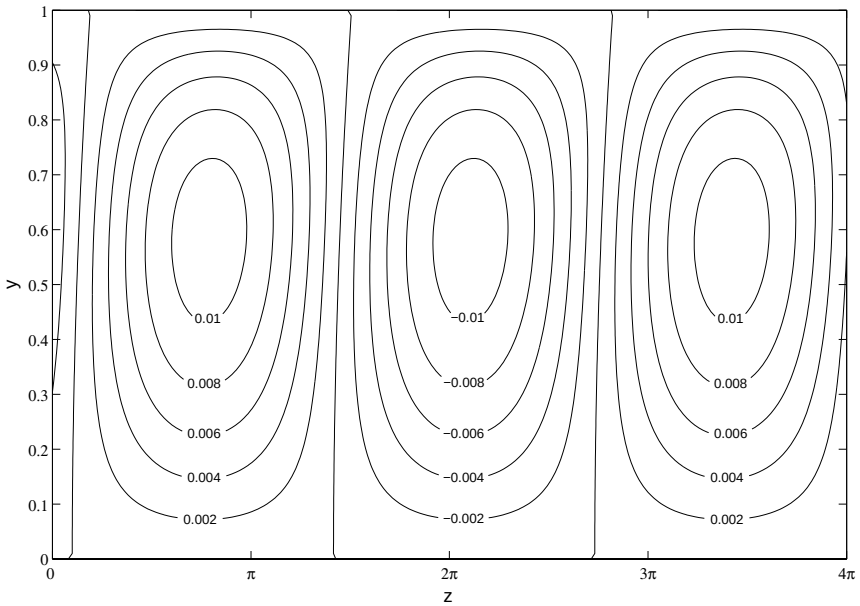

Figure 4.7. Real streamline disturbances on the x plane for Cercignani model, $Pr = 0.70$ and $Kn = 0.40$ at $t = 1/\sigma_r$.

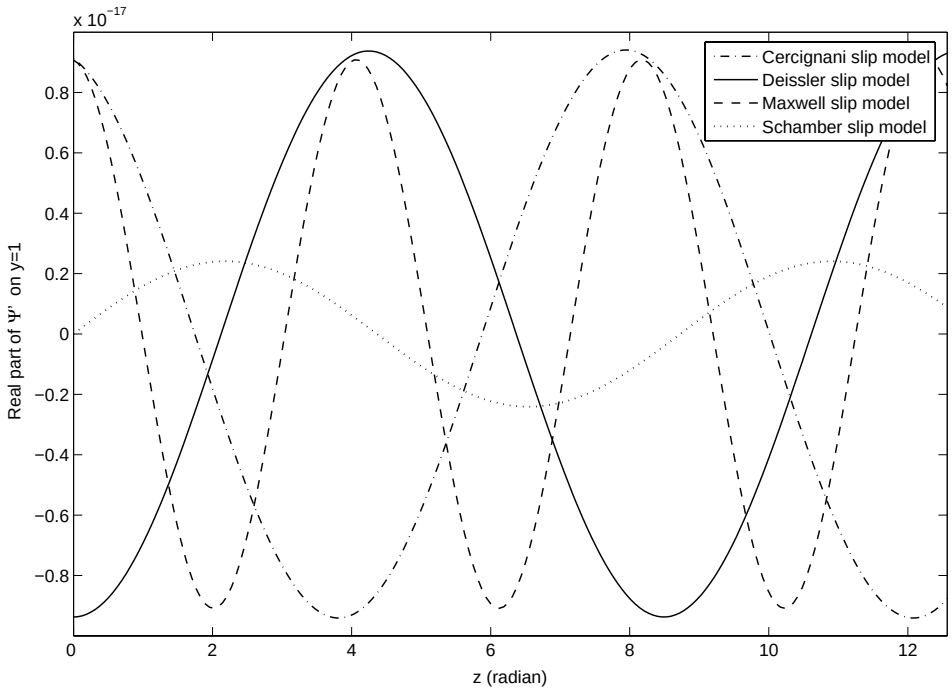

Figure 4.8. Real streamline disturbances on $y = 1$ plane for different models, $Pr = 0.70$ and $Kn = 0.40$ at $t = 1/\sigma_r$.

After the introduction of thermal waves occurring on the top wall and streamline patterns, we can explain the mechanism lying behind the initiation of the proposed instability. For this purpose, we should consider both temperature and w' disturbances indicated by Figures 4.2 and 4.7. Increase in local temperature on somewhere of the top surface leads to migration (in fact transpiration) of the fluid from cooler region to this new hotter region. Thus, surface motion from one side takes place to this hot location. At the same time, fluid particles located in the inner region of the enclosure are directed to the previous region of the fluid particles which have just migrated to the hotter region. Thus, the conservation of mass law is satisfied and a vertical stream is established. As a result of this vertical stream, fluid particles on the other side of the hot region goes to the inner region of the enclosure as well. Thus, cellular flow pattern are observed in the x plane as shown Figures 4.6 and 4.7. While the negative-valued iso-curves rotate in clockwise direction, the negative valued ones spin in counter direction as well.

Neutral curves for the slip models have been shown in Figure 4.9. Inspection

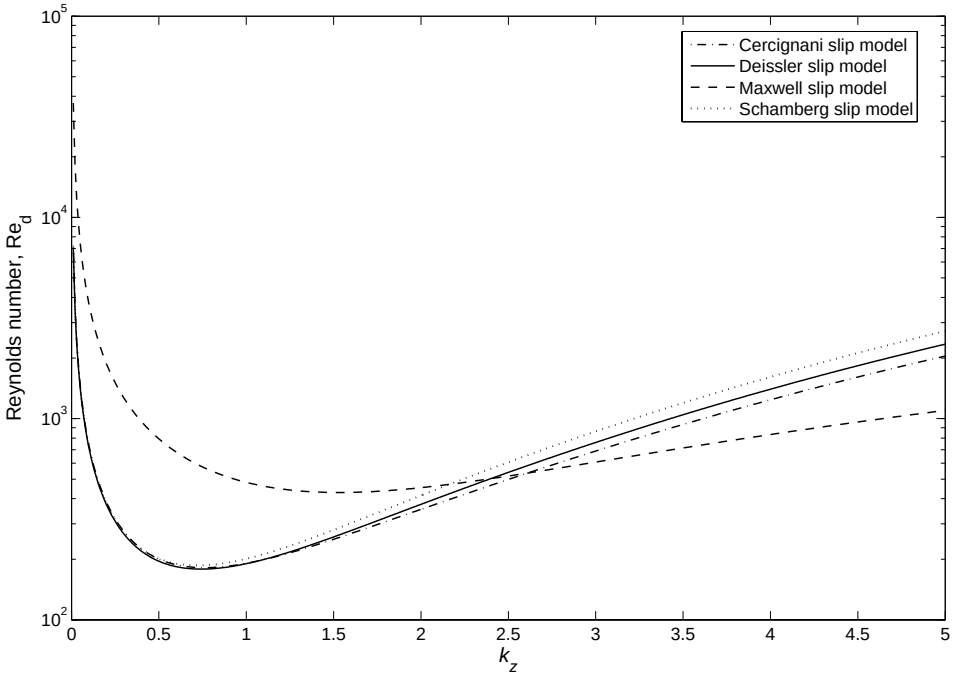

Figure 4.9. Neutral curves for different models; $Pr = 0.70$ and $Kn = 0.40$

of the Figure 4.9 reveals that Maxwell model is more stable as compared the other slip boundary conditions. All second-order slip boundary conditions have the same character in the critical region. As k_z increases, the discrepancy among the neutral states by second-order models slightly increases as well. It is important to see response of neutral states to varying Kn numbers. Figure 4.10 shows neutral curves for different Kn numbers with the Cercignani model. It can be eventually recognized that increase in Kn number leads to decreases in critical Re_d. Most importantly, variation of critical thresholds with Kn number is shown Figure 4.11. Maxwell model is always more stable than the other slip models. Moreover, as Kn number increases critical Re_d decreases monotonically as expected.

We should also discuss the effect of Pr number on the stability limits. Table 4.2 gives $(Re_d)_{cr}$ for varying Pr numbers for the different slip boundary conditions. From Table 4.2 it can be concluded that the effect of Pr number on critical states is negligible.

A question coming into minds is phase speed of the waves. Figure 4.12 gives

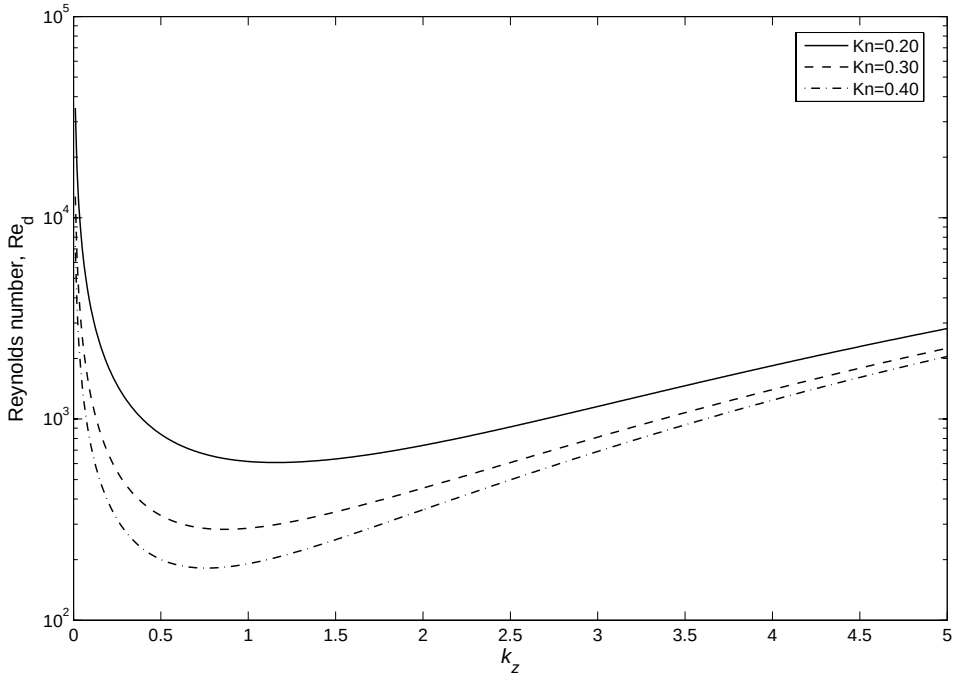

Figure 4.10. Neutral curves for different Kn numbers with Cercignani model; $Pr = 0.70$

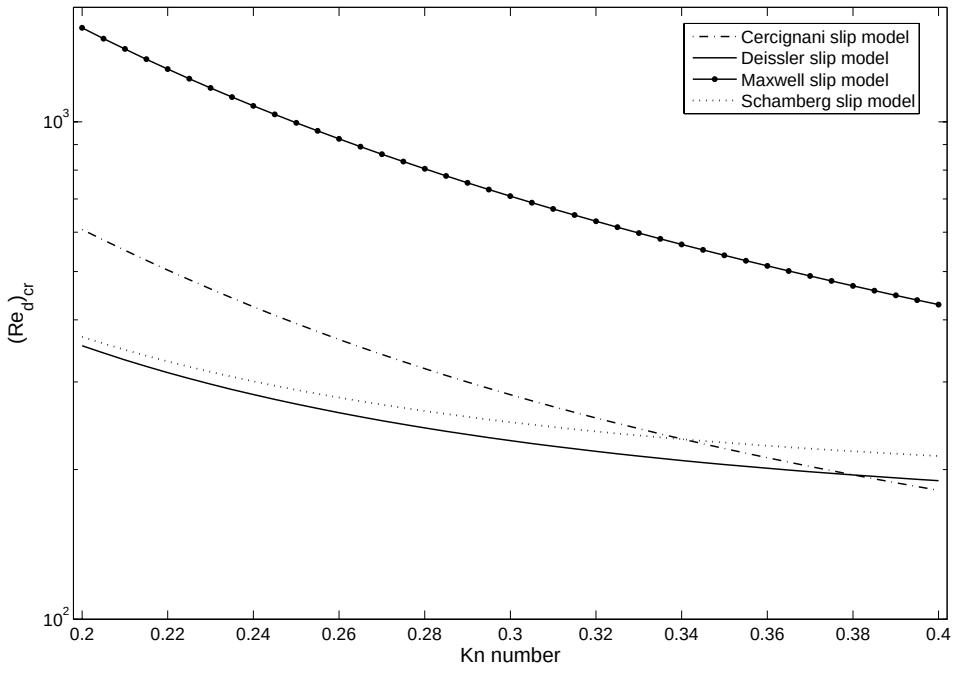

Figure 4.11. Neutral curves for different Kn numbers with Cercignani model; $Pr = 0.70$

Table 4.2. $(Re_d)_{cr}$ for varying Pr numbers and different slip models

	Cercignani model	Deissler model	Maxwell model	Schamberg model
$Pr = 0.65$	183.62	181.05	445.87	189.07
$Pr = 0.70$	181.58	178.67	429.23	186.35
$Pr = 0.75$	176.82	176.58	414.30	183.97

critical phase speeds for three second-order models. As it can be seen from the figure

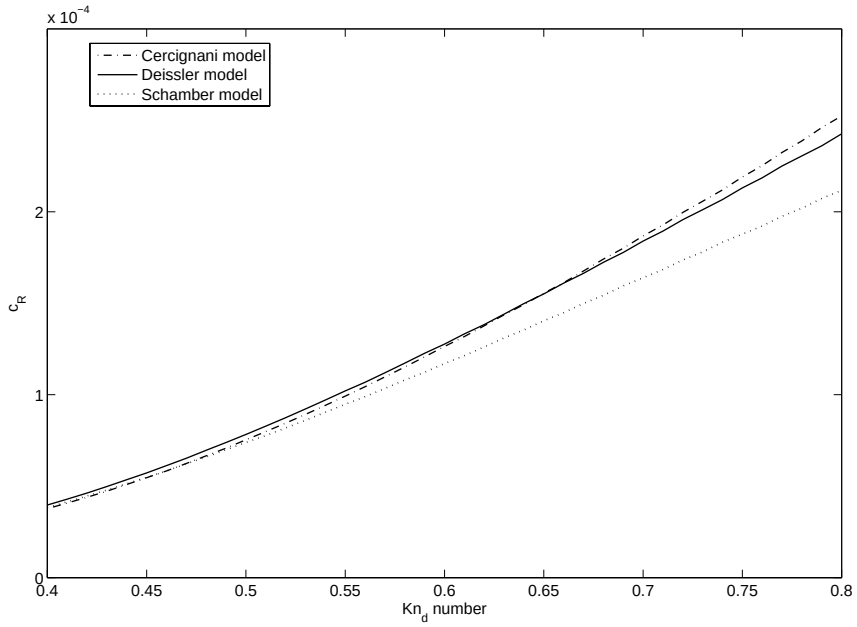

Figure 4.12. Critical phase speeds for varying Kn numbers; $Pr = 0.70$

the phase speed is very small. However, there is an increase with Kn_d number. Phase speeds by three second-order slip model are approximately equal up to $Kn_d = 0.55$. After this limit, Schamberg model gives smaller values than the other two models (recall that$A_2 = -5\pi/12$ for Schamberg model is the smallest among the models)

Apart from the studied models, stability limits of Beskok model has also been investigated. Beskok model are always stable to axisymmetric disturbances. $A_2 = 0.5$ coefficient of Beskok model which is greater than zero leads to this stable behavior. This behavior has also been observed for the other models. In other words, as A_2 increases, stability of the thermal transpiration flow becomes stronger.

The following deductions can be made for the stability of thermal transpiration flow to the axisymmetric disturbances:

1. As Pr number increases, threshold of the instability decreases. However the effect of Pr number is still weak for this flow.
2. Slip models play an important role in the formation of neutral states. Maxwell model which is the first-order model is more stable than second-order models. Such an observation can be supported by considering the mathematical formulation of the velocity slip boundary conditions. Clearly, increase in A_1 or A_2 results in higher stability limits. Since $A_1 = 1.1466$ of Cercignani model is greater than Deissler and Schamberg models, Cercignani model gives higher critical Re_d's. In addition to the first-order coefficient, increase in A_2 leads to more stable states.
3. As wave number increases, sharp decreases are observed in $(Re_d)_n$ up to the $(k_z)_{cr}$. After this limit, Re_d increases monotonically.
4. Kn number plays a critical role on the formation of instable states. $(Re_d)_{cr}$ varies non-linearly with respect to Kn number as seen from Figure 4.11. Undoubtedly, the same analysis may be done for a larger range of Kn numbers. Nonetheless, creation of surface slip velocity leading to instable states may not be possible for small Kn number. Moreover, choosing large valued $Kn \geq 0.5$ numbers causes invalidity of continuum hypothesis. These limitations are the bottleneck of the analysis.
5. We have also investigated the effect of Beskok model on the stability of proposed flow. Our efforts have shown that Beskok model is always stable to axisymmetric disturbances. This is due to positive valued second-order coefficient of Beskok model. Such behavior also exhibits the effect of slip coefficients.
6. The mechanism in the initiation of the instability has been tried to verified. Immigration of fluid particles to hot spots creates a surface flow. Satisfaction of mass conservation requires a vertical current originating from the core regions of the enclosure. Thus, rolls of disturbances are established.

In the next section three-dimensional stability analysis will be performed. For this purpose, an artificial compressibility method will be employed to the generalized

eigenvalue problem.

4.4.3. Generalized Eigenvalue Problem in Three-Dimensions, ($k_x \neq 0$)

Numerical methods to solve the normal mode equations of linear the stability theory can be categorized in two main headings: Initial Value Problem (IVP) and Boundary Value Problem (BVP).

In the first methodology, the normal mode equations are reduced to a system of first-order differential equations and the solution is integrated from one boundary to the other one until both boundary conditions are satisfied. A pioneering work performed by Scott *et al.* (1977) deals with solving two-point differential equations. They have used superposition coupled with an orthonormalization procedure and a variable step Runge-Kutta-Fehlberg integration scheme. This methodology along with resulting computer code has been widely used in the study of hydrodynamic stability. The main advantage of the IVPs is having optimum memory requirements and being sufficiently accurate. On the other hand, this method necessitates very good initial guess of the eigenvalues for convergence.

Differential equations of linear stability are discretized using either finite differences or spectral methods in case of BVPs. The global eigenvalues can be obtained by solving characteristic determinants of the generalized eigenvalue problem. If anything is known about stability problem, BVP methods can get eigen-spectra. Mostly, eigen-spectra found from BVP is used as the initial condition of IVP. The BVP techniques are more time and memory consuming compared with IVPs.

Malik (1990) has been compared both global (BVPs) and local (IVPs) to search eigenvalues for temporal linear stability analysis of the hyperbolic boundary layer. He has been taken account a second-order finite difference, a fourth-order accurate two-point compact finite difference scheme and a Chebyshev spectral collocation method. On the other hand, Hu *et al.* (1998) has been examined stability of supersonic Couette flow of a compressible and viscous fluid. Equations of normal mode form for com-

pressible flow reduced to algebraic set of equations so called Generalized Eigenvalue Problem (GEP), using Chebyshev spectral collocation methods and fourth-order finite difference. Solution of GEP has been achieved by employing QZ algorithm (Moler *et al.*, 1973). In the present study, both second-order and fourth-order (co-located) finite difference schemes have been used like Malik (1990) and Hu *et al.* (1998). Details of the discretization can be found in referred articles.

Let's introduce a vector of perturbation modes $\mathbf{\Phi} = [u_0', v_0', p_0', w_0', \theta_0']^{tr}$. After the reduction to discrete form whatever the difference scheme is, the GEP can be formed with respect to the eigenvalue, σ, as

$$A\mathbf{\Phi} = \sigma B\mathbf{\Phi}, \tag{4.64}$$

where Φ is the discrete version of the eigenfunctions. Equation 4.64 can easily be converted to the singularity condition of $A - \sigma B$

$$\det(A - \sigma B) = 0. \tag{4.65}$$

If B is not singular, Equation 4.65 is solved via LR or QR methods (Wilkinson, 1965; Stoer *et al.*, 1992).

$$\det(B^{-1}A - \sigma I) = 0. \tag{4.66}$$

In the current study, if the boundary conditions are settled down in the discrete form of the eigensystem —in this case dimensions of $B^{-1}A$ will be $(5n-2) \times (5n-2)$, excluding pressure on the boundaries— one encounters with an obstacle which makes the matrix B singular. Two remedies are suggested by Malik (1990). The first alternative is elimination of boundary nodes by substituting boundary values into interior grids wherever the discrete equations need. This is one of the natural ways to overcome the singularity as expected and the present study considers this approach as well. Thus the dimensions of matrix $B^{-1}A$ will be $(5n-10) \times (5n-10)$. In the second

alternative, the boundary values are replaced by reasonable values which will not affect the physical eigenvalue spectrum. For more details, the readers referred to pages 388-389 of Malik (1990). On the other hand, not only direct substitution of BCs both also absence of time derivative introduces a singularity in the incompressible model. Some of the strategies removing the singularity have been explained by Khorrami *et al.* (1989). Row and column operations, reducing the rank of the matrix B are commonly used methods. The other choice is placing a time derivative of pressure, $\gamma\sigma p_j$, into the continuity equation. This procedure may be termed as artificial compressibility and eliminates singularity of the matrix. The parameter, γ, is chosen as a small parameter such that it does not influence the physical eigenvalue spectrum. Such a procedure will be implemented rather different way in our work. For this purpose, we should go back to the origin of artificial compressibility idea. Chorin (1967) was the first who reorganized continuity equations so that the equation resembles compressible version of it. According to his proposition incompressible continuity equation takes the form

$$\frac{\partial \rho}{\partial t} + \operatorname{div} \mathbf{u} = 0$$

where ρ is taken as artificial density. The density is linked to pressure by an artificial eos $p = \rho/\delta$ and δ is called as artificial compressibility. As the solution proceeds to the converged state, the added time derivative will lose its importance and behaves like a relaxation parameter. After Chorin's initiative study which does not consist of physical time derivative, the methodology has been extended to time accurate formulations which are applied to unsteady problems (Peyret, 1976; Rogers *et al.*, 1990; Rogers *et al.*, 1991; Kallinderis *et al.*, 2005). One of the studies employing artificial compressibility method has been performed by Ding *et al.* (1999). In their analysis, material derivative of pressure p is located in the incompressible continuity equation. The idea behind their approaches will be verified in the next sentences.

Let's consider three-dimensional compressible continuity equation

$$\frac{\partial \rho}{\partial t} + (\mathbf{u} \cdot \operatorname{grad})\rho + \rho \operatorname{div} \mathbf{u} = 0$$

Assuming $\rho = \rho(p)$, the continuity equation is rewritten using chain rule of differenti-

ation

$$\frac{\partial \rho}{\partial p}\left[\frac{\partial p}{\partial t}+(\mathbf{u}\cdot \operatorname{grad})p\right]+\rho \operatorname{div}\mathbf{u}=0,$$

where the term $\frac{\partial \rho}{\partial p}$ is easily determined from the artificial eos

$$\frac{\partial \rho}{\partial p}=\delta.$$

On the other hand, the relationship between artificial speed of sound and the compressibility factor, δ is given as

$$\tilde{c}=\frac{1}{\sqrt{\delta}}$$

which leads to artificial Mach number;

$$\tilde{Ma}=\frac{V_{max}}{\tilde{c}}.$$

Here, V_{max} denotes maximum value of velocity vector in the flow domain and its estimated by the following relation

$$V_{max}=\max\left[\left(u^2+v^2+w^2\right)^{\frac{1}{2}},u_0\right].$$

Since most of the compressible flows are assumed as incompressible for Ma number smaller than 0.3, the maximum allowable artificial $\tilde{Ma}$ number should be less than 0.3,

$$\tilde{Ma}=\frac{V_{max}}{\tilde{c}}=\sqrt{\delta}V_{max}\leq 0.3.$$

Thus, assuming the maximum velocity in the flow domain occurs on the top boundary (this maximum velocity has also been taken as reference velocity on the flow field), the

new continuity equation including the artificial $\tilde{M}a$ number is written

$$\left[\frac{\partial p}{\partial t} + (\mathbf{u} \cdot \mathrm{grad})p\right] + \frac{Re}{\tilde{M}a^2}\,\mathrm{div}\,\mathbf{u} = 0. \tag{4.67}$$

For more details, interested readers are referred to Rahman *et al.* (2001) and pages 661-665 of Tannehill *et al.* (1997).

Once, artificial compressibility is applied to the problem, the new continuity equation should be rewritten in terms of normal mode form. Note that, material derivative of the basic flow pressure vanishes,

$$\frac{\mathrm{D}\,\bar{p}}{\mathrm{D}\,t} = \frac{\partial \bar{p}}{\partial t} + (\bar{\mathbf{u}} \cdot \mathrm{grad})\,\bar{p} = 0,$$

and so continuity equation turns out to be Equation 4.5. Utilizing Equation 4.67, linear disturbance equation and its normal mode representation can be expressed as

$$\left[\frac{\partial p'}{\partial t} + (\bar{\mathbf{u}} \cdot \mathrm{grad})p' + (\mathbf{u}' \cdot \mathrm{grad})\bar{p}\right] + \frac{Re}{\tilde{M}a^2}\,\mathrm{div}\,\mathbf{u}' = 0 \tag{4.68}$$

and

$$\left[-ik_x\bar{u} + i\sigma\right]p_0' = u_0'\frac{d\bar{p}}{dx} + \frac{Re}{\tilde{M}a^2}\left[ik_x u_0' + \mathrm{D}\,v_0' + ik_z w_0'\right], \tag{4.69}$$

respectively. In the current analysis, freshly derived normal mode representation of continuity equation, Equation 4.69, will be used instead of Equation 4.31 for three-dimensional linear stability analysis. It should be noted that adiabatic boundary condition for the bottom boundary has been employed in three-dimensional analysis. The boundary conditions are read as, on the bottom wall, $y = 0$

$$u_0' = \left[A_1 Kn\,\mathrm{D}\,u_0' + A_2 Kn^2\,\mathrm{D}^2\,u_0'\right] + Kn^2(ik_x\theta_0') \tag{4.70}$$

$$v_0' = 0 \tag{4.71}$$

$$w_0' = \left[A_1 Kn\, \mathrm{D}\, w_0' + A_2 Kn^2\, \mathrm{D}^2\, w_0'\right] + Kn^2(ik_z\theta_0') \tag{4.72}$$

$$\mathrm{D}\,\theta_0' = 0 \tag{4.73}$$

and $y = 1$

$$u_0' = \left[-A_1 Kn\, \mathrm{D}\, u_0' + A_2 Kn^2\, \mathrm{D}^2\, u_0'\right] + Kn^2(ik_x\theta_0') \tag{4.74}$$

$$v_0' = 0 \tag{4.75}$$

$$w_0' = \left[-A_1 Kn\, \mathrm{D}\, w_0' + A_2 Kn^2\, \mathrm{D}^2\, w_0'\right] + Kn^2(ik_z\theta_0') \tag{4.76}$$

$$\theta_0' = \left(\frac{2\gamma}{\gamma+1}\frac{1}{Pr}\left[-A_1 Kn\, \mathrm{D}\,\theta_0' + A_2 Kn^2\, \mathrm{D}^2\,\theta_0'\right]\right) \tag{4.77}$$

The basic motion solutions are borrowed from Chapter 3 and given as

$$\bar{\mathbf{u}} = [u, v, w]^{tr} = \left[\frac{Kn^2}{1 + 6A_1 Kn - 12A_2 Kn^2}\left(6y^2 - 6y + 1\right), 0, 0\right]^{tr}$$

$$\bar{p}_x = \frac{12Kn^2}{1 + 6A_1 Kn - 12A_2 Kn^2}$$

$$\bar{\theta} = x + RePr\left\{\frac{Kn^2}{1 + 6A_1 Kn - 12A_2 Kn^2}\left[\frac{1}{2}\left(y^4 + y^2\right) - y^3 + \left(\frac{2\gamma}{\gamma+1}\right)\frac{A_2 Kn^2}{Pr}\right]\right\}. \tag{4.78}$$

Note that, Re number is based on the channel height d in the three dimensional analysis.

The next section introduces some results and critics of the three-dimensional analysis.

4.4.4. Results and Discussions for Three-Dimensional Instability, ($k_x \neq 0$)

In this section, eigenvalue spectrums for certain cases will be exhibited and then the dependency of eigen-solutions to $\tilde{Ma}$ number and the number of grids will be elucidated. Dependency of eigen-spectra will be examined for certain cases.

We list discretization ways used in this study as the following:

- `Method 1.` Fourth-order accurate, co-located finite difference representation only on the inner grids of the domain,
- `Method 2.` Fourth-order accurate, co-located finite difference representation including boundary grids,
- `Method 3.` Second-order accurate, co-located finite difference discretization only on the inner grids of the domain.

It should be pointed out that two types of eigenvalues are observed in all computations. The first item of the group expresses the correct solution and called as "physical modes". This eigenvalues show small changes with the number of grids. As the number of grids increases, no change in eigen-modes is expected. In contrast to physical eigenvalues, there are outstanding, highly damped, negative and large valued $\Im\sigma$'s in all computations. Magnitude of these modes greatly affected by the grid resolution. Such modes are called as "spurious modes" in the specialized literature. For the time being, we are not dealing with details of spurious modes or the ways elimination of them. Using captured correct physical modes, we will just try to analyze eigen-spectra and eigen-solutions. Throughout the analysis `Method 2` is chosen to be the best candidate.

Effect of artificial compressibility on eigenvalue spectrum is pictured in Figures 4.13 and 4.14. As $1/\tilde{M}a^2$ diminishes, the spectrum widens along the $\Re\sigma$. Moreover, majority of the modes exhibits dominant damping effects (eigen values do not accommodate in the vicinity of the axis $\Im\sigma = 0$). Clearly, choosing a large valued $\tilde{M}a^2$ destroys the basic idea lying behind the artificial compressibility. To examine behavior of instable modes obtained by different levels of artificial compressibility, we refer Table 4.3. As it can be seen, each of artificial $\tilde{M}a^2$ number leads to approximately the same mode. While, `Method 2` captures instable modes, the other methods are still stable. Instable eigenvalues captured by $\tilde{M}a^2 = 1/10$, $\tilde{M}a^2 = 1/50$ and $\tilde{M}a^2 = 1/150$ just give the same eigenvalue, $(-0.6672E-03+0.1900E-02\ i)$. Therefore, $\tilde{M}a^2 = 1/50$ has been chosen for the safety of computations in the current analysis. Figures 4.15 and 4.16 give a comparison of eigen-spectra calculated by `Method 1`, `Method 2` and

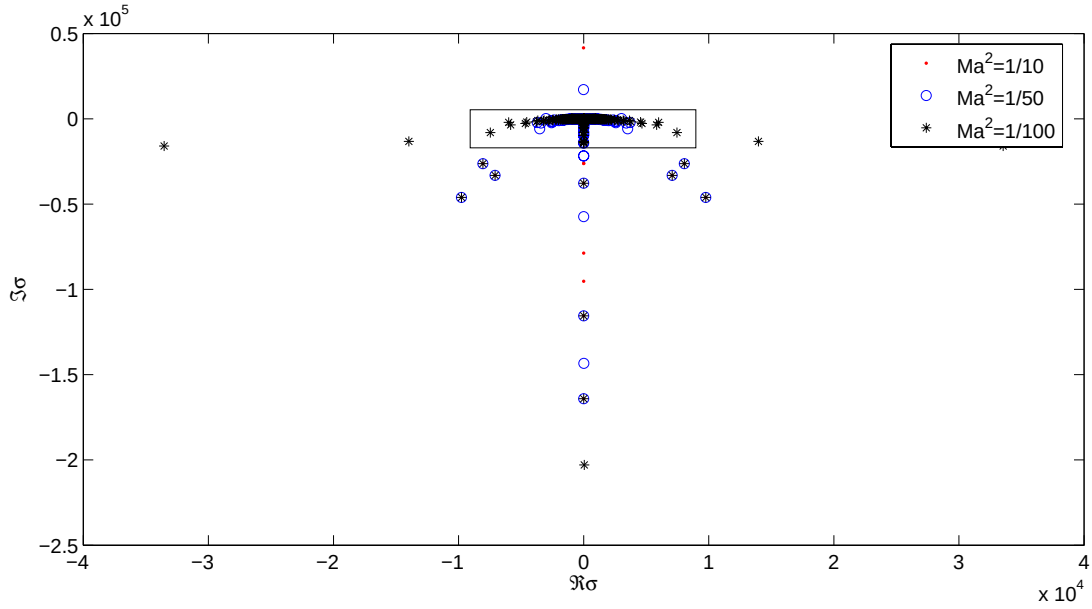

Figure 4.13. Eigenspectrum for different artificial $\tilde{M}a$ numbers at a neutral state defined by of $RePr = 89.994$, $Kn = 0.25$, $Pr = 0.72$, $k_x = 0.15$, $k_z = 0.10$ $(A_1 = 1.1466)$

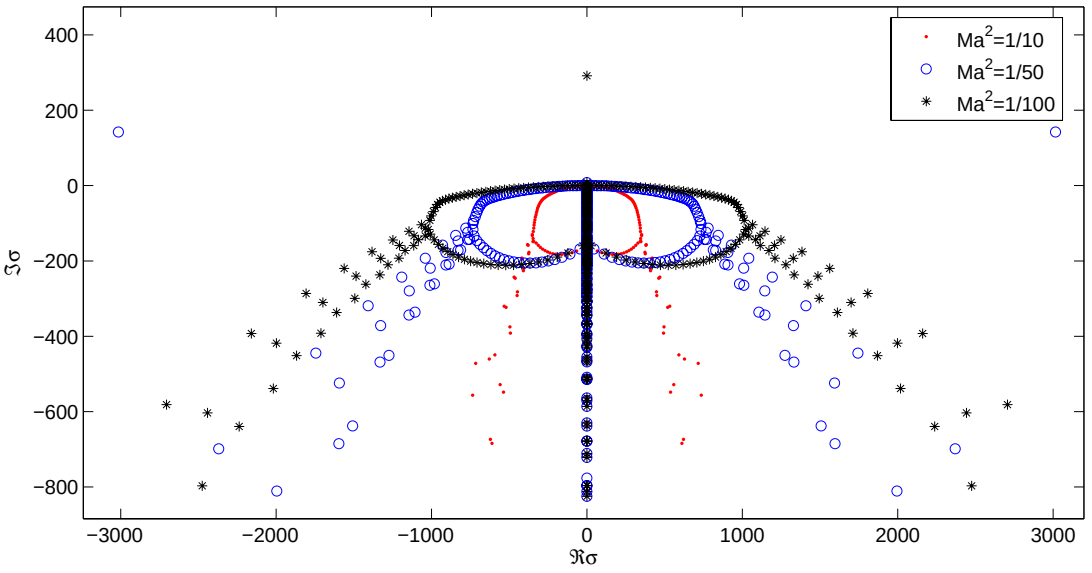

Figure 4.14. Magnified view of the eigenspectrum pointed out by a rectangle in Figure 4.13

Table 4.3. The effect of $\tilde{Ma}^2$ on the real and imaginary parts of the instable mode of the eigensystem for $k_x = 0.15$, $k_z = 0.10$, $RePr = 89.993804$, $A_1 = 1.1466$ and $n = 120$

$\tilde{Ma}^2$	Method 1		Method 2		Method 3	
1/10	-0.684342E-03	-0.353387E-03	-0.667294E-03	0.190056E-02	-0.741302E-03	-0.790412E-02
1/25	-0.690327E-03	-0.369649E-03	-0.673937E-03	0.193024E-02	-0.741313E-03	-0.790411E-02
1/50	-0.689301E-03	-0.373666E-03	-0.667259E-03	0.190036E-02	-0.741309E-03	-0.790412E-02
1/75	-0.689324E-03	-0.373885E-03	-0.753457E-03	0.198887E-02	-0.741313E-03	-0.790400E-02
1/100	-0.690097E-03	-0.373633E-03	-0.664753E-03	0.182552E-02	-0.741312E-03	-0.790402E-02
1/150	-0.691274E-03	-0.365891E-03	-0.667123E-03	0.189970E-02	-0.741312E-03	-0.790412E-02

`Method 3`. Although, two fourth-order accurate methods approximately give the same spectra, the second-order methodology does not present precise results contrary to our expectations. Table 4.4 examines grid resolution of `Method 2` for $A_1 = 1.1466$ and

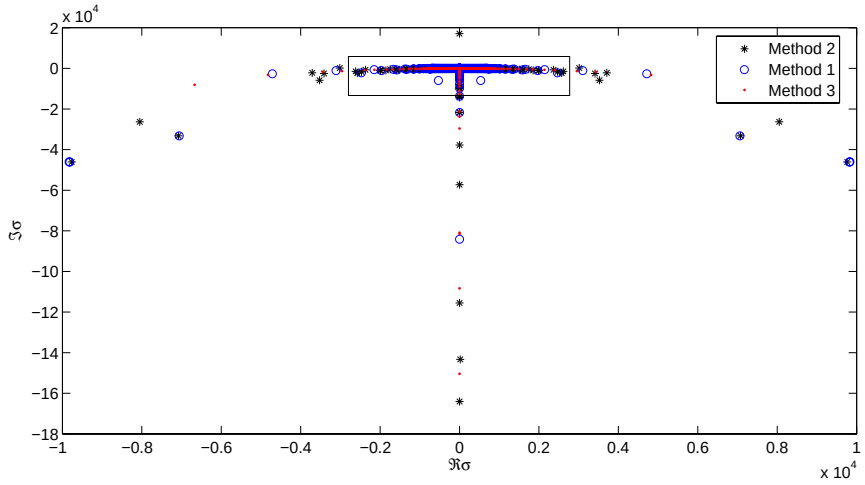

Figure 4.15. Eigenspectrum for enclosure flow of a rarefied gas at the neutral state of $RePr = 89.994$, $Kn = 0.25$, $Pr = 0.72$, $k_x = 0.10$ and $k_z = 0.15$ ($A_1 = 1.1466$)

$A_2 = 1$, respectively. Clearly, increase in the number of grids lead to slight variations in $\Re\sigma$ for both BC models. However, real part of the eigenvalue for Maxwell model always gives smaller values than the Cercignani model. In Figures 4.17 and 4.18 some of the eigen-vectors are shown for $A_1 = 1.1466$ and $A_1 = 1$. As it can be seen from the figures, all disturbances are symmetric with respect to the $y = 0.5$ axis, the centerline

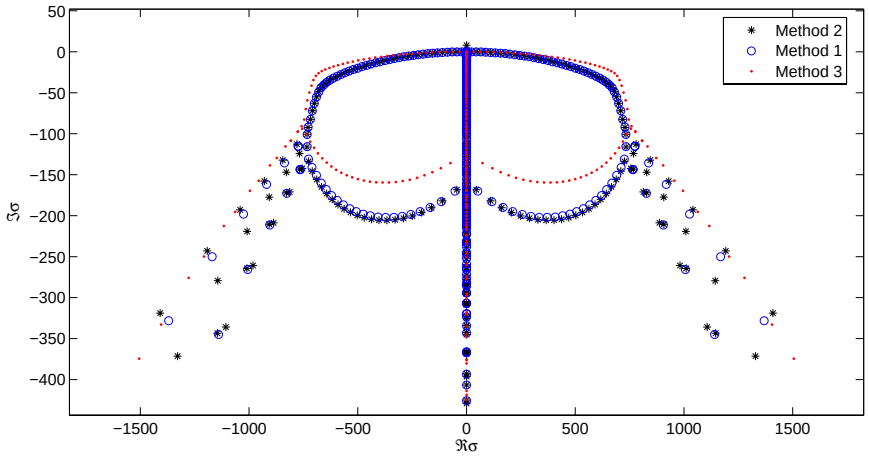

Figure 4.16. Zoomed eigenspectrum specified by a rectangle in Figure 4.15

of the enclosure.

From the results we can come up with the following consequences:

1. Although, employed finite difference approximation is accurate enough fourth-order accurate, it is not suitable for GEP. Due to unavoidable spurious eigen-modes, we could not get any neutral curve which defines instability limits of the proposed flow.
2. Artificial compressibility methods works well even for moderate $\tilde{M}a$'s. However, due to limitations of finite difference formulation, very dense grid resolution is required to guarantee correct results. Apparently, increase in the number of grids makes such an eigen-system analysis impossible in terms of computational cost.
3. Since GEP is very sensitive to indispensable discretization errors resulting spurious eigenvalue spectrum, we propose spectral methods to get error-free eigen-spectra.

Table 4.4. Variation of real part of the leading mode with grid resolution for $k_x = 0.15$, $k_z = 0.10$, $RePr = 89.993804$ and $Kn = 0.25$

n	$A_1 = 1.1466$	$A_1 = 1.0$
10	-0.859321E-03	-0.932548E-03
15	-0.777720E-03	-0.847985E-03
50	-0.684632E-03	-0.745403E-03
100	-0.679848E-03	-0.730296E-03
120	-0.667259E-03	-0.726088E-03
150	-0.661683E-03	-0.719843E-03
200	-0.645793E-03	-0.697878E-03

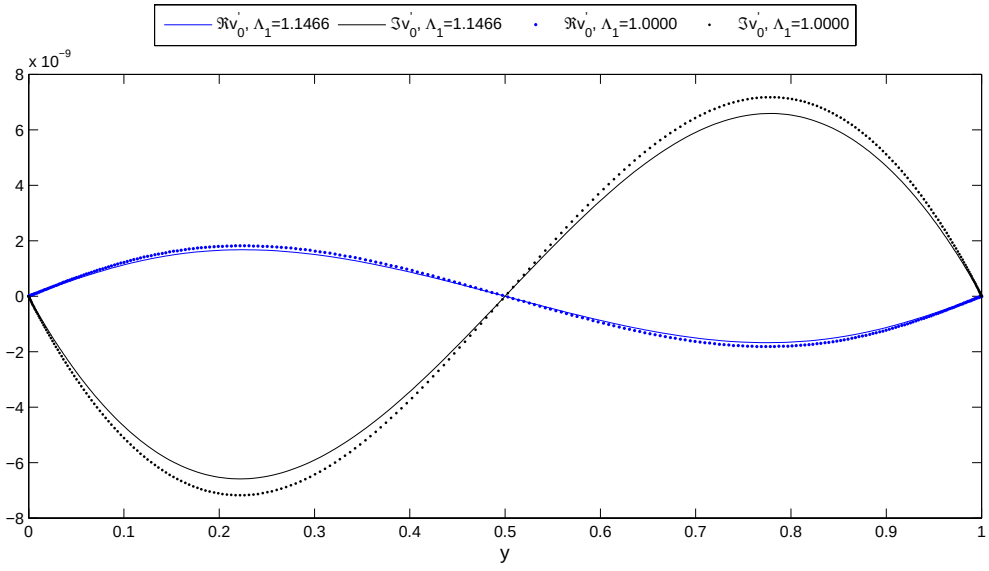

Figure 4.17. Real and Imaginary parts of the disturbance eigenfunction v_0' at a neutral state defined by $(RePr)_n = 46.8327$, $Kn = 0.25$, $Pr = 0.72$ and $k_z = 0.15$ for $(n = 280)$

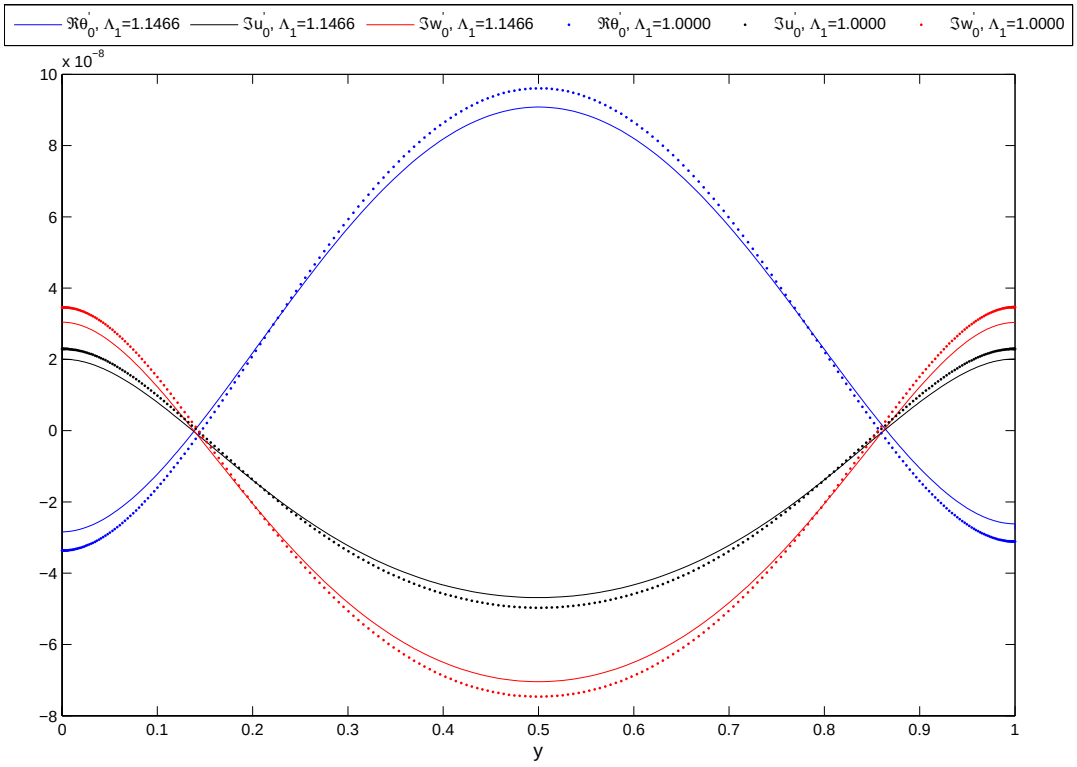

Figure 4.18. The effect of slip boundary conditions on the same disturbance eigenfunctions for $(RePr)_n = 46.8327$, $Kn = 0.25$, $Pr = 0.72$ and $k_z = 0.15$, $(n = 280)$

5. CONVECTION OF RAREFIED GASES IN ENCLOSURES: NUMERICAL SIMULATIONS

This chapter introduces stability characteristics and flow structures of two dimensional, thermal transpiration driven convection of rarefied gases by numerical simulation. In the analysis, two-dimensional, unsteady Burnett and NS equations will be used as modeling tools. As reported Chapter 4, employment of Burnett equations allows to observe motions created by both thermal transpiration and thermal stress effects. On the other hand, use of NS equations excludes the effects of thermal stresses. Both mathematical model will be discretized by finite volume method and will be solved via a multi-stage scheme which will be presented in the following sections.

5.1. Physical and Mathematical Models

This section brings the details of both physical and mathematical issues of proposed flow instability. In Section 5.1.1, anatomical aspects of the flow will be pictured. All details about the mathematical model will be given in Section 5.1.2

5.1.1. Physical Model for the Two-Dimensional Convection

Thermal transpiration of a compressible, Newtonian rarefied gas is contemplated. The flow takes places in a rectangular enclosure with length l and height $\epsilon \times l$, where ϵ is the aspect ratio. As described in Section 4.2, the vertical side walls are kept at temperatures T_c on the left and T_h on the right. The bottom wall is assumed as adiabatic and temperature of the top boundary varies linearly. The schematized view of the enclosure has been shown in Figure 3.2.

The kinematic viscosity, μ, and the coefficient of heat conduction k are temperature dependent and variations of these thermo-physical parameters with temperature have been modeled with Power-Law relation, as given by Equations 2.14 and 2.15.

5.1.2. Mathematical Models

Two-dimensional mathematical model of the present study is defined in Equations 2.5-2.13 with the boundary conditions given in Equations 3.5-3.16. Remember that, exclusion of second and third-order approximations of Burnett equations gives the classical NS equations. To take the advantage of studying non-dimensional numbers, the following scaling parameters are introduced

$$t^* = \frac{tu_0}{d}, \quad x^* = \frac{x}{d}, \quad y^* = \frac{y}{d}, \quad u^* = \frac{u}{u_0}, \quad v^* = \frac{v}{u_0}, \quad \theta = \frac{T}{\Delta T}, \quad \epsilon = \frac{d}{l}$$

$$p^* = \frac{p}{\mu_0 u_0/d}, \quad \mu^* = \frac{\mu}{\mu_0}, \quad k* = \frac{k}{k_0}, \quad \rho^* = \frac{\rho}{\rho_0}, \quad E^* = \frac{E}{c_{p_0}\Delta T}, \quad r_T = \frac{\Delta T}{T_0}.$$

Remember that, quantities marked with 0 are evaluated at mean temperature of $T_0 = (T_h + T_c)/2$. Such reference values are more convenient for the non-dimensional representation of Burnett equations. Here, u_0 is defined in terms of thermal speed as the following

$$u_0 = \sqrt{\frac{r_T}{\pi}}\, V_{th} \qquad \text{with} \qquad V_{th} = \sqrt{2RT_0}.$$

In this case, Re number will be

$$Re = \frac{\rho_0 u_0 d}{\mu_0} = \frac{\sqrt{r_T}}{Kn} \qquad \text{with} \qquad Kn = \frac{\mu_0}{\rho_0 d\sqrt{2RT_0/\pi}}.$$

Integral conservation equation read as

$$\frac{\partial}{\partial t}\int_\Omega \mathbf{W}\, d\Omega + \oint_{\partial\Omega} (\mathbf{F}_c - \mathbf{F}_v)\, dA = \int_\Omega \mathbf{S}\, d\Omega.$$

Dropping *'s in the scaled variables, dimensionless form of the flux vectors, given by Equations 2.5-2.7, results in the following expressions (*in two-dimensions*)

for conservative variables

$$\mathbf{W} = \begin{bmatrix} \rho \\ \rho u \\ \rho v \\ \rho E \end{bmatrix} \tag{5.1}$$

for convective fluxes

$$\mathbf{F}_c = \begin{bmatrix} \rho V \\ \rho u V \\ \rho v V \\ \rho E V \end{bmatrix} \tag{5.2}$$

and for diffusive fluxes

$$\mathbf{F}_v = \begin{bmatrix} 0 \\ n_x(\tau_{xx} - \frac{1}{Re}p) + n_y\tau_{xy} \\ n_x\tau_{yx} + n_y(\tau_{yy} - \frac{1}{Re}p) \\ n_x\Phi_x + n_y\Phi_y \end{bmatrix}, \tag{5.3}$$

$$\mathbf{S} = \begin{bmatrix} 0 \\ 0 \\ \frac{\rho f_y}{Fr} \\ 0 \end{bmatrix}. \tag{5.4}$$

where

$$\Phi_x = -\frac{Ec}{Re}\, up + Ec\,(u\tau_{xx} + v\tau_{xy}) - q_x,$$

$$\Phi_y = -\frac{Ec}{Re}\ vp + Ec\left(u\tau_{yx} + v\tau_{yy}\right) - q_y,$$

and

$$f_y = -1$$

Chapman-Enskog expansion of diffusive terms in Burnett equations are expressed for

the first-order approximations expansion:

$$\tau_{xx}^{(1)} = \frac{1}{Re}\mu\left(\frac{4}{3}u_x - \frac{2}{3}v_y\right),\ \tau_{xy}^{(1)} = \tau_{yx}^{(1)} = \frac{1}{Re}\mu\left(u_y + v_x\right),\ \tau_{yy}^{(1)} = \frac{1}{Re}\mu\left(\frac{4}{3}v_y - \frac{2}{3}u_x\right),$$

$$q_x^{(1)} = \frac{1}{RePr}\left(-k\theta_x\right), \qquad q_y^{(1)} = \frac{1}{RePr}\left(-k\theta_y\right),$$

the second order approximations:

$$\tau_{xx}^{(2)} = -\frac{1}{Re}\frac{\mu^2}{p}\left[\alpha_1 u_x^2 + \alpha_2 u_x v_y + \alpha_3 v_y^2 + \alpha_4 u_x v_y + \alpha_5 u_y^2 + \alpha_6 v_x^2\right]$$

$$-\frac{\pi}{2}\frac{1}{Re}\frac{\mu^2}{p}\left[\alpha_7\theta_{xx} + \alpha_8\theta_{yy} + \alpha_9\frac{\theta}{\rho}\rho_{xx} + \alpha_{10}\frac{\theta}{\rho}\rho_{yy} + \alpha_{11}\frac{\theta}{\rho^2}\rho_x^2 +\right.$$

$$\left.\alpha_{12}\frac{1}{\rho}\theta_x\rho_x + \alpha_{13}\frac{1}{\theta}\theta_x^2 + \alpha_{14}\frac{\theta}{\rho^2}\rho_y^2 + \alpha_{15}\frac{1}{\rho}\theta_y\rho_y + \alpha_{16}\frac{1}{\theta}\theta_y^2\right]$$

$$\tau_{yx}^{(2)} = \tau_{xy}^{(2)} = -\frac{1}{Re}\frac{\mu^2}{p}\left[\beta_1 u_x u_y + \beta_2(u_y v_y + u_x v_x) + \beta_1 v_x v_y +\right]$$

$$-\frac{\pi}{2}\frac{1}{Re}\frac{\mu^2}{p}\left[\beta_3\theta_{xy} + \beta_4\frac{\theta}{\rho}\rho_{xy} + \beta_5\frac{1}{\theta}\theta_x\theta_y + \beta_6\frac{\theta}{\rho^2}\rho_x\rho_y + \beta_7\frac{1}{\rho}\rho_x\theta_y + \beta_7\frac{1}{\rho}\rho_y\theta_x\right],$$

$$\tau_{yy}^{(2)} = -\frac{1}{Re}\frac{\mu^2}{p}\Big[\alpha_1 v_y^2 + \alpha_2 u_x v_y + \alpha_3 u_x^2 + \alpha_4 u_y v_x + \alpha_5 v_x^2 + \alpha_6 u_y^2\Big]$$

$$-\frac{\pi}{2}\frac{1}{Re}\frac{\mu^2}{p}\Big[\alpha_7\theta_{yy} + \alpha_8\theta_{xx} + \alpha_9\frac{\theta}{\rho}\rho_{yy} + \alpha_{10}\frac{\theta}{\rho}\rho_{xx} + \alpha_{11}\frac{\theta}{\rho^2}\rho_y^2 +$$

$$\alpha_{12}\frac{1}{\rho}\theta_y\rho_y + \alpha_{13}\frac{1}{\theta}\theta_y^2 + \alpha_{14}\frac{\theta}{\rho^2}\rho_x^2 + \alpha_{15}\frac{1}{\rho}\theta_x\rho_x + \alpha_{16}\frac{1}{\theta}\theta_x^2\Big],$$

$$q_x^{(2)} = -\frac{Ec}{Re^2}\frac{\mu^2}{\rho}\Big[\gamma_1\frac{1}{\theta}\theta_x u_x + \gamma_2\frac{1}{\theta}\theta_x v_y + \gamma_3 u_{xx} + \gamma_4 u_{yy} + \gamma_5 v_{xy} + \gamma_6\frac{1}{\theta}\theta_y v_x$$

$$\gamma_7\frac{1}{\theta}\theta_y u_y + \gamma_8\frac{1}{\rho}\rho_x u_x + \gamma_9\frac{1}{\rho}\rho_x v_y + \gamma_{10}\frac{1}{\rho}\rho_y u_y + \gamma_{11}\frac{1}{\rho}\rho_y v_x\Big],$$

$$q_y^{(2)} = -\frac{Ec}{Re^2}\frac{\mu^2}{\rho}\Big[\gamma_1\frac{1}{\theta}\theta_y u_y + \gamma_2\frac{1}{\theta}\theta_y v_x + \gamma_3 v_{yy} + \gamma_4 v_{xx} + \gamma_5 u_{xy} + \gamma_6\frac{1}{\theta}\theta_x u_y$$

$$\gamma_7\frac{1}{\theta}\theta_x v_x + \gamma_8\frac{1}{\rho}\rho_y v_y + \gamma_9\frac{1}{\rho}\rho_y u_x + \gamma_{10}\frac{1}{\rho}\rho_x v_x + \gamma_{11}\frac{1}{\rho}\rho_x u_y\Big]$$

and finally third-order approximations (augmented terms)

$$\tau_{xx}^{(3)} = -\frac{\pi}{2}\frac{1}{Re}\frac{\mu^3}{p^2}\theta\left[\alpha_{17}(u_{xxx} + u_{xyy}) + \alpha_{18}(v_{xxy} + v_{yyy})\right],$$

$$\tau_{yx}^{(3)} = \tau_{xy}^{(a)} = -\frac{\pi}{2}\frac{1}{Re}\frac{\mu^3}{p^2}\theta\left[\beta_8(u_{xxy} + u_{yyy} + v_{xyy} + v_{xxx})\right],$$

$$\tau_{yy}^{(3)} = -\frac{\pi}{2}\frac{1}{Re}\frac{\mu^3}{p^2}\theta\left[\alpha_{17}(v_{yyy} + v_{xxy}) + \alpha_{18}(u_{xyy} + u_{xxx})\right],$$

$$q_x^{(3)} = \frac{\gamma-1}{\gamma}\frac{1}{Re^2}\frac{\mu^3}{p\rho}\left[\gamma_{12}(\theta_{xxx} + \theta_{xyy}) + \gamma_{13}\frac{\theta}{\rho}\left(\rho_{xxx} + \rho_{xyy}\right)\right],$$

$$q_y^{(3)} = \frac{\gamma-1}{\gamma}\frac{1}{Re^2}\frac{\mu^3}{p\rho}\left[\gamma_{12}(\theta_{yyy}+\theta_{xxy})+\gamma_{13}\frac{\theta}{\rho}\left(\rho_{yyy}+\rho_{xxy}\right)\right].$$

The coefficients, $\alpha_1 \ldots \alpha_{18}$, $\beta_1 \ldots \beta_8$ and $\gamma_1 \ldots \gamma_{13}$ are determined from Chapman-Enskog expansion. For the sake of brevity we will not give these coefficients. More details can be found from Aqarwal *et al.* (2001). Here, Eckert (Ec) and Fr numbers are determined as

$$Ec = \frac{2}{\pi}\frac{\gamma-1}{\gamma} \qquad \text{and} \qquad Fr = \frac{u_0^2 d}{g_0},$$

respectively. In addition to the governing equations, dimensionless forms of eos and total energy become

$$p = \frac{\pi}{2}Re\rho\theta \qquad \text{and} \qquad E = \frac{\theta}{\gamma}+\frac{Ec}{2}\left(u^2+v^2\right),$$

respectively. Boundary conditions have been re-organized for mentioned reference values and formulated as
for the bottom wall:

$$u(x,0,t) - A_1 Kn u_y(x,0,t) - A_2 Kn^2 u_{yy}(x,0,t) - \frac{3}{4}r_T\frac{1}{Re}\theta_x(x,0,t) = 0 \tag{5.5}$$

$$v(x,0,t) = 0 \tag{5.6}$$

$$\theta_y(x,0,t) = 0 \tag{5.7}$$

for the top wall:

$$u(x,1,t) + A_1 Kn u_y(x,1,t) - A_2 Kn^2 u_{yy}(x,1,t) - \frac{3}{4}r_T\frac{1}{Re}\theta_x(x,1,t) = 0 \tag{5.8}$$

$$v(x,1,t) = 0 \tag{5.9}$$

$$\theta(x,1,t) - \theta_{w3} - \frac{2\gamma}{\gamma+1}\frac{1}{Pr}\left[-A_1 Kn\theta_y(x,1,t) + A_2\theta_{yy}(x,1,t)\right] = 0 \tag{5.10}$$

$$\text{with} \qquad \theta_{w3} = \frac{1}{r_T} - A_2 + \epsilon x$$

on the left wall:

$$v(0,y,t) - A_1 Kn u_x(0,y,t) - A_2 Kn^2 u_{xx}(0,y,t) - \frac{3}{4} r_T \frac{1}{Re} \theta_y(0,y,t) = 0 \tag{5.11}$$

$$u(0,y,t) = 0 \tag{5.12}$$

$$\theta(0,y,t) - \theta_{w4} - \frac{2\gamma}{\gamma+1}\frac{1}{Pr}\left[A_1 Kn \theta_x(0,y,t) + A_2 Kn^2 \theta_{xx}(0,y,t)\right] = 0 \tag{5.13}$$

$$\text{with} \qquad \theta_{w4} = \frac{1}{r_T} - \frac{1}{2}$$

and finally the right wall:

$$v(\epsilon,y,t) + A_1 Kn u_x(\epsilon,y,t) - A_2 Kn^2 u_{xx}(\epsilon,y,t) - \frac{3}{4} r_T \frac{1}{Re} \theta_y(\epsilon,y,t) = 0 \tag{5.14}$$

$$u(\epsilon,y,t) = 0 \tag{5.15}$$

$$\theta(\epsilon,y,t) - \theta_{w2} - \frac{2\gamma}{\gamma+1}\frac{1}{Pr}\left[-A_1 Kn \theta_x(\epsilon,y,t) + A_2 Kn^2 \theta_{xx}(\epsilon,y,t)\right] = 0 \tag{5.16}$$

$$\text{with} \qquad \theta_{w2} = \frac{1}{r_T} + \frac{1}{2}$$

Since Burnett equations are fourth-order differential equations, there should be additional two BCs to complete mathematical system. Lack of such additional BCs are the most important drawback of the Burnett equations. To overcome this difficulty, linear extrapolation is conducted in most cases (Lee, 1994).

Initial conditions of Burnett equations are referenced to basic state solutions which are rearranged according to the new scales and read as

$$u(x,y,0) = \frac{3 r_T}{4Re(1 + 6A_1 Kn - 6A_2 Kn^2)}\left(6y^2 - 6y + 1\right), \tag{5.17}$$

$$p(x,y,0) = \frac{36 r_T}{4Re(1 + 6A_1 Kn - 6A_2 Kn^2)} x + p_0, \tag{5.18}$$

$$\theta(x,y,0) = \left(\frac{1}{r_T} - \frac{1}{2}\right) + \epsilon x + \frac{3r_T}{4Re(1+6A_1Kn-6A_2Kn^2)}\left[\frac{1}{2}\left(y^4+y^2\right) - y^3 + \frac{\gamma}{\gamma+1}\frac{Kn^2}{Pr}\right], \quad (5.19)$$

where p_0 stands for a reasonable initial guess for the pressure. Initial condition for density is computed using eos.

5.2. Numerical Approach

The cell centered finite volume method is applied for the reduction of conservation equations and BCs to non-linear sets of algebraic equations. All flow variables are fixed at the centroid of the volume cells as illustrated Figure 5.1 Assuming that the shape

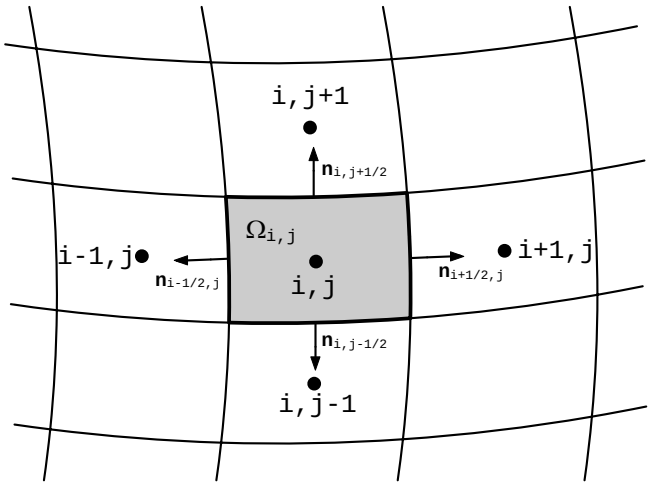

Figure 5.1. A cell-centered control volume and its neighbors.

of the control volume (cv) does not change with time. Thus, time rate of change of conserved quantities modifies to

$$\frac{\partial}{\partial t}\int_\Omega \mathbf{W}\, d\Omega = \Omega\frac{\partial \mathbf{W}}{\partial t}$$

and Equation 2.5 turns out to be

$$\frac{\partial \mathbf{W}}{\partial t} = -\frac{1}{\Omega}\left\{ \oint_{\partial\Omega} \left(\mathbf{F}_c - \mathbf{F}_v\right)\, dA - \int_\Omega \mathbf{S}\, d\Omega \right\}, \quad (5.20)$$

where $\mathbf{W} = [\rho,\ \rho\mathbf{u},\ \rho E]^{tr}$ is the vector of conservative variables. The integrals on the right hand side of the Equation 5.20 can be represented in discrete form by accounting geometric details of the control volume as illustrated in Figure 5.1 (by generalization to three-dimension)

$$\frac{d\mathbf{W}_{i,j,k}}{dt} = -\frac{1}{\Omega_{i,j,k}}\left\{ \sum_{m=1}^{N} \left(\mathbf{F}_c - \mathbf{F}_v\right)_m \Delta A_m - \left(\mathbf{S}\ \Omega\right)_{i,j,k} \right\} \tag{5.21}$$

where N designates the number of cell faces and ΔA_m stands for the area of the m^{th} cell face. Equation 5.21 can be written in a different way such that

$$\frac{d\mathbf{W}_{i,j,k}}{dt} = -\frac{1}{\Omega_{i,j,k}}\mathbf{R}_{i,j,k} \tag{5.22}$$

and $\mathbf{R}_{i,j,k}$ stands for residual vector. Thus, Equation 5.22 governs a system of first-order IVPs and should be solved with appropriate BCs. Since, finite volume discretization necessitates evaluation of convective and diffusive fluxes at the cell faces, they should be calculated in terms of main nodes located on the geometric centers of the cells. An averaging technique for the calculation of the flux vectors on the cell faces can be cast in the following form, for example on cell face of $\mathbf{n}_{i+\frac{1}{2},j}$,

$$\left(\mathbf{F}\Delta A\right)_{i+\frac{1}{2},j} \cong \mathbf{F}\left(\mathbf{W}_{i+\frac{1}{2},j}\right)\Delta A_{i+\frac{1}{2},j} \tag{5.23}$$

where all conservative and dependent, such as p, u, v etc., variables are computed on the cell face of $\mathbf{n}_{i+1/2,j,k}$ by arithmetic mean

$$\mathbf{W}_{i,j,k} = \frac{1}{2}\left(\mathbf{W}_{i,j,k} + \mathbf{W}_{i+1,j,k}\right),$$

where $\mathbf{F}$ designates either convective or viscous diffusion fluxes.

5.2.1. Discretization of Convection Fluxes

As is well known, in some problems of the compressible fluid mechanics, central difference schemes may not exhibits the correct physics or it totally fails to get a solution. For example, capturing shock waves may not be possible or contact discontinuities may not be resolved without undesirable oscillations (Jameson, 2001). Therefore, non-oscillatory schemes by introducing controlled diffusive or anti-diffusive terms become indispensable for successful computations.

The central scheme expressed by Equation 5.23, can be reformed by adding anti-diffusive terms in a controlled manner to preserve positivity of the central differencing scheme.

$$(\mathbf{F}\Delta A)_{i+\frac{1}{2},j} \cong \mathbf{F}\left(\mathbf{W}_{i+\frac{1}{2},j}\right)\Delta A_{i+\frac{1}{2},j} - \mathbf{D}_{i+\frac{1}{2},j,k} \tag{5.24}$$

Let's define an difference operator such that, $\delta\mathbf{W}_{i+\frac{1}{2},j,k} = \mathbf{W}_{i+1,j,k} - \mathbf{W}_{i,j,k}$. The first version of JST scheme has been constructed by subtraction of neighbored differences to develop a third-order diffusive flux

$$\mathbf{D}_{i+\frac{1}{2},j,k} = \alpha_{i+\frac{1}{2},j,k}\left\{\delta\mathbf{W}_{i+\frac{1}{2},j,k} - \frac{1}{2}\left(\delta\mathbf{W}_{i+\frac{3}{2},j,k} + \delta\mathbf{W}_{i-\frac{1}{2},j,k}\right)\right\}$$

According to Jameson (1995), this scheme does not satisfy positivity condition. The scheme generates oscillations in the vicinity of shock waves and this oscillatory behavior can be eliminated by switching to the first order scheme locally and resulting blended diffusion follows as

$$\begin{aligned}\mathbf{D}_{i+\frac{1}{2},j,k} = &+ \epsilon^{(2)}_{i+\frac{1}{2},j,k}\delta\mathbf{W}_{i+\frac{1}{2},j,k} \\ &- \epsilon^{(4)}_{i+\frac{1}{2},j,k}\left(\delta\mathbf{W}_{i+\frac{3}{2},j,k} - 2\delta\mathbf{W}_{i+\frac{1}{2},j,k} + \delta\mathbf{W}_{i-\frac{1}{2},j,k}\right)\end{aligned} \tag{5.25}$$

The idea lying behind the use of adaptive coefficients, $\epsilon^{(2)}_{i+\frac{1}{2},j,k}$ and $\epsilon^{(4)}_{i+\frac{1}{2},j,k}$ is to produce

low level diffusion on regions where sharp gradients are not observed, and prevent oscillations near the discontinuities. Note that blend of $\epsilon^{(2)}_{i+\frac{1}{2},j,k}$ and $\epsilon^{(4)}_{i+\frac{1}{2},j,k}$ which are order of two and four, respectively, generates a third-order accurate dissipation of $\mathbf{D}_{i+\frac{1}{2},j,k}$. The details of switching between the second- and fourth-order diffusions, and also construction of them will not be given in this text and can be found in Blazek (2001), Wesseling (2001) and Jameson *et al.* (1981), etc. On the other hand, the simulation of Burnett equations requires density values on the boundaries due to discretization of inviscid terms. Therefore, derivation of suitable density BCs for the slip flow regime should be made by smearing characteristic theory of compressible fluid dynamics. The procedure will be presented in Appendix B.

5.2.2. Discretization of Viscous Fluxes

The viscous fluxes $\mathbf{F}_v$ which appears in Equation 5.21 can be discretized similar to those of convective fluxes. The main difference between the two fluxes is that the viscous flux requires to know dependent and thermo-physical variables at main nodes. Some of these variables are $\mathbf{u}$, T, μ etc. whose values on the cell faces are specified as

$$\Upsilon_{i+\frac{1}{2},j,k} = \frac{1}{2}\left(\Upsilon_{i,j,k} + \Upsilon_{i+1,j,k}\right)$$

where Υ stands for any one of the flow or the thermo-physical variables. Derivatives on the cell faces can be reduced to discrete form by means of

- finite difference and
- Green's theorem.

In the present study, the latter item will be employed for the discretizations methodology. There will be a need of constructing auxiliary cell, shown in Figure 5.2, to compute gradients on the cell faces. The first-order derivative is easily estimated (at

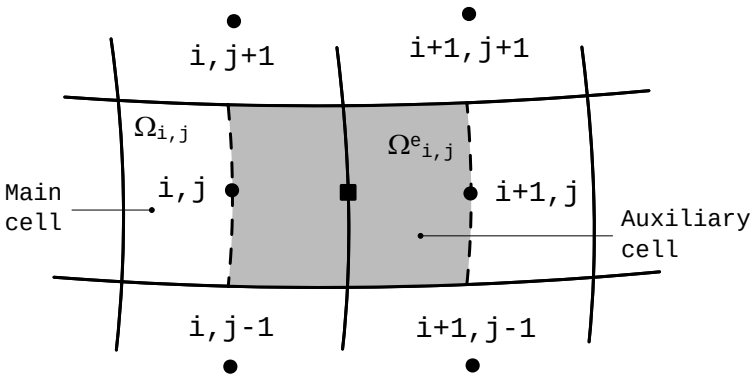

Figure 5.2. An auxiliary cell to compute derivatives on the cell face of $\mathbf{n}_{i+\frac{1}{2},j}$

the point shown by square in Figure 5.2 by applying Green's theorem

$$\left.\frac{\partial \Upsilon}{\partial x}\right|_{i+\frac{1}{2},j} = \frac{1}{\Omega^e}\int_{\partial\Omega^e} \Upsilon \, dA_x^e = \frac{1}{\Omega_{i,j}^e}\sum_{m=1}^{N} \Upsilon_m \, A_{x,m}^e, \tag{5.26}$$

where N designates number of faces in the auxiliary cell e, (east cell with respect to the main cell). $\Omega_{i,j}^e$ is being the volume of the auxiliary control volume and $A_{x,m}^e$ is x component of surface vector which is determined from $\mathbf{A}_m^e = A_m^e \mathbf{n}_m^e = [A_{x,m}^e,\ A_{y,m}^e,\ A_{z,m}^e]^{tr}$ on the m^{th} face of the "e" cell.

The higher-order derivatives are treated by a similar manner. Let's consider second-order derivative on the cell face of "$i+\frac{1}{2}, j$ ". Adoption of basic principle simply yields

$$\left.\frac{\partial^2 \Upsilon}{\partial x^2}\right|_{i+\frac{1}{2},j} = \frac{1}{\Omega^e}\int_{\partial\Omega^e} \frac{\partial \Upsilon}{\partial x} \, dA_x^e = \frac{1}{\Omega_{i,j}^e}\sum_{m=1}^{N} \left.\frac{\partial \Upsilon}{\partial x}\right|_m A_{x,m}^e. \tag{5.27}$$

Notice that, calculation of the second-order gradient requires the first-order derivatives (in Equation 5.27) on the faces of the auxiliary cell (Jameson, 2001). High-order stress tensor terms of the Burnett equations have been discretized subsequent uses of Green's theorem.

5.2.3. Time Stepping Scheme

When the spatial discretization task is accomplished, a set of coupled differential equations emerges and it can be expressed as

$$\frac{d\mathbf{W}_{i,j,k}}{dt} = -\mathbf{R}_{i,j,k}\left(\mathbf{W}\right) \tag{5.28}$$

where $\mathbf{R}(\mathbf{W})$ is the vector residual which composes of convective, viscous and artificially added dissipative fluxes. In steady state computations, the transient solution acts as an relaxation parameter and accelerates the rate of convergence. This set of differential equation can be solved either via *implicit* or *explicit schemes*. Information about the solution procedures can be found any standard textbook related to the " Numerical Analysis or Computational Fluid Mechanics". Since, Burnett equations have stiff non-linear terms in stress tensors of order-two and three, the present study takes into account explicit schemes.

Now, consider the principle idea of explicit time discretization such that

$$\Delta\mathbf{W}^{n}_{i,j,k} = -\frac{\Delta t_{i,j,k}}{\Omega_{i,j,k}}\mathbf{R}_{i,j,k}\left(\mathbf{W}\right) \tag{5.29}$$

where $\Delta\mathbf{W}_{i,j,k} = \mathbf{W}^{n+1}_{i,j,k} - \mathbf{W}^{n}_{i,j,k}$ denotes the difference between the solutions of conservative variable at time gap $\Delta t_{i,j,k}$ which varies locally in the domain. An explicit scheme takes the information from past time (t), which is already known, and proceeds to the solution of next time step $(t + \Delta t)$ with the relation of Equation 5.29.

Explicit multi-stage schemes are widely used in practice. Especially, Direct Numerical Simulation of turbulent flows requires efficient solution methodologies involving low memory storage, high stability region and good convergence characteristics (Williamson, 1980; Christopher *et al.*, 2000). In this study, an explicit multi stage scheme of Jameson *et al.* (1981) has been applied to get solutions of Burnett equations.

Table 5.1. Coefficients of multistage scheme for varying CFL numbers.

	first-order scheme			**second-order scheme**		
CFL	1.5	2.0	2.5	0.69	0.92	1.15
$\boldsymbol{\alpha_1}$	0.1481	0.0833	0.0533	0.1918	0.1084	0.0695
$\boldsymbol{\alpha_2}$	0.4000	0.2069	0.1263	0.4929	0.2602	0.1602
$\boldsymbol{\alpha_3}$	1.0000	0.4265	0.2375	1.0000	0.5052	0.2898
$\boldsymbol{\alpha_4}$	-	1.0000	0.4414	-	1.0000	0.5060
$\boldsymbol{\alpha_5}$	-	-	1.0000	-	-	1.0000

The m-stage scheme is written as

$$
\begin{aligned}
\mathbf{W}_{i,j,k}^{(0)} &= \mathbf{W}_{i,j,k}^{n} \\
\mathbf{W}_{i,j,k}^{(1)} &= \mathbf{W}_{i,j,k}^{(0)} - \alpha_1 \frac{\Delta t_{i,j,k}}{\Omega_{i,j,k}} \mathbf{R}_{i,j,k}\left(\mathbf{W}_{i,j,k}^{(0)}\right) \\
\mathbf{W}_{i,j,k}^{(2)} &= \mathbf{W}_{i,j,k}^{(0)} - \alpha_2 \frac{\Delta t_{i,j,k}}{\Omega_{i,j,k}} \mathbf{R}_{i,j,k}\left(\mathbf{W}_{i,j,k}^{(1)}\right) \\
&\vdots \\
\mathbf{W}_{i,j,k}^{n+1} &= \mathbf{W}_{i,j,k}^{(m)} = \mathbf{W}_{i,j,k}^{(0)} - \alpha_m \frac{\Delta t_{i,j,k}}{\Omega_{i,j,k}} \mathbf{R}_{i,j,k}\left(\mathbf{W}_{i,j,k}^{(m-1)}\right)
\end{aligned}
\tag{5.30}
$$

where α_k designates stage coefficients. Additionally, $\mathbf{R}_{i,j,k}^{k}$ designates residual vector formed by the solution $\mathbf{W}_{i,j,k}^{(k)}$ evaluated on the k^{th} stage.

The time step $\Delta t_{i,j,k}$ is restricted by the flow type and grid structure which are mainly expressed by Courant-Friedrichs-Lewy condition. Determination of maximum allowable time step is not given in this context and can be found on pages 186-190 and 337-343 of Blazek (2001) and pages 91-92 of Kallinderis *et al.* (2005). While, many problems in mechanics require small time advancements, such as Direct Numerical Simulation and Large Eddy Simulation of turbulence in which time increments should be smaller than Kolmogorov time scale, in some transient problems, time scale

should be large enough compared with scales divided by the eigenvalues, such as flutter, rotor-stator interaction, etc (Blazek, 2001). As is well known, implicit methods give a flexibility of choosing any desired time step for unsteady state simulation. In addition to implicit methods, *dual time stepping* approach considerably reduces time restriction of explicit schemes, which will be elucidated in Section 5.2.4.

5.2.4. Dual Time Stepping Scheme

Recall that, the innovative idea of Chorin (1967) was a process adding a time derivative of artificial compressibility to continuity equation. This conception may be extended to the compressible flow equations by adding an artificial time derivative of each conservative variables to their own equations. Thus, conservation equations have two different time derivative terms

$$\frac{d\mathbf{W}_{i,j,k}}{dt^*} + \frac{d\mathbf{W}_{i,j,k}}{dt} = -\mathbf{R}_{i,j,k}\left(\mathbf{W}\right), \tag{5.31}$$

where $\frac{d\mathbf{W}_{i,j,k}}{dt^*}$ and $\frac{d\mathbf{W}_{i,j,k}}{dt}$ denote artificially added (pseudo) and physical time derivatives, respectively. The system of equations is written as in a different way

$$\frac{d\mathbf{W}_{i,j,k}}{dt^*} = -\mathbf{R}^*_{i,j,k}\left(\mathbf{W}\right), \tag{5.32}$$

with *unsteady residual*

$$\mathbf{R}^*_{i,j,k}\left(\mathbf{W}\right) = \frac{3}{2\Delta t}\mathbf{W}^{n+1}_{i,j,k} - \frac{2}{\Delta t}\mathbf{W}^{n}_{i,j,k} + \frac{1}{2\Delta t}\mathbf{W}^{n-1}_{i,j,k} + \frac{1}{\Omega_{i,j,k}}\mathbf{R}_{i,j,k}\left(\mathbf{W}\right). \tag{5.33}$$

The unsteady residual $\mathbf{R}^*_{i,j,k}\left(\mathbf{W}\right)$ is formed by contributions of the physical time derivative discretized by use of the second-order backward finite difference method, and the steady residual including convective, diffusive and artificially dissipative flux terms as defined by Equations 5.21 and 5.22.

The advancement in physical time from (t) to $(t + \Delta t)$ is realized by evaluating first the unsteady residual $\mathbf{R}^*_{i,j,k}\left(\mathbf{W}\right)$ and then solving steady-state problem, Equation 5.32, in pseudo-time. Once the steady-state in pseudo time is achieved, the next time so-

lution is found (Kallinderis *et al.*, 2005). The current study exploits $m = 4$ stage, second-order accurate scheme for the solution of steady-state problem in pseudo-time

$$\begin{aligned}
\mathbf{W}_{i,j,k}^{(0)} &= \mathbf{W}_{i,j,k}^{k} \\
\mathbf{W}_{i,j,k}^{(1)} &= \mathbf{W}_{i,j,k}^{(0)} - \alpha_1 \frac{\Delta t_{i,j,k}^{*}}{\Omega_{i,j,k}} \mathbf{R}_{i,j,k}^{*} \left(\mathbf{W}_{i,j,k}^{(0)} \right) \\
\mathbf{W}_{i,j,k}^{(2)} &= \mathbf{W}_{i,j,k}^{(0)} - \alpha_2 \frac{\Delta t_{i,j,k}^{*}}{\Omega_{i,j,k}} \mathbf{R}_{i,j,k}^{*} \left(\mathbf{W}_{i,j,k}^{(1)} \right) \\
&\vdots \\
\mathbf{W}_{i,j,k}^{k+1} = \mathbf{W}_{i,j,k}^{(m)} &= \mathbf{W}_{i,j,k}^{(0)} - \alpha_m \frac{\Delta t_{i,j,k}^{*}}{\Omega_{i,j,k}} \mathbf{R}_{i,j,k}^{*} \left(\mathbf{W}_{i,j,k}^{(m-1)} \right)
\end{aligned} \tag{5.34}$$

where $\Delta t_{i,j,k}^{*}$ is local pseudo-time step and α's are optimized coefficients of the multi-stage scheme given in Table 5.1. The time marching starts from $\mathbf{W}_{i,j,k}^{k} = \mathbf{W}_{i,j,k}^{n}$ and continues until $\mathbf{R}_{i,j,k}^{*}$ is reduced to acceptable order of magnitudes so that $\mathbf{W}_{i,j,k}^{k+1}$ approximates a new physical time solution $\mathbf{W}_{i,j,k}^{n+1}$.

The next section gives results and critics of some simulations by NS and Burnett equations.

5.2.5. Results and Discussions

In this section we will introduce some sample results of NS and Burnett simulations as described below.

The simulations in this section have been performed for Nitrogen gas with the following thermo-physical properties

$$c_p = 1.075 \times 10^3 \quad \frac{\mathrm{J}}{\mathrm{kgK}}, \quad Pr = 0.701, \quad n = 0.67,$$

Table 5.2. Response of maximum u velocity and net mass flux to the grid resolution

number of cells, $n_x \times n_y$	u_{max}	m_{net}
128×128	3.9597×10^{-3}	-2.4135×10^{-6}
81×81	3.9753×10^{-3}	-3.1023×10^{-5}
71×71	3.9749×10^{-3}	-2.5900×10^{-5}
91×91	3.9640×10^{-3}	-9.3963×10^{-5}
81×20	3.9422×10^{-3}	-2.7637×10^{-5}

$$T_r = 273 \quad ^\circ\text{K}, \quad \mu_r = 1.663 \times 10^{-5} \quad \frac{\text{Ns}}{\text{m}^2} \quad \text{for Power-Law viscosity model.}$$

Mean temperature is chosen as $T_0 = 600$ °K in all computations. All simulations are performed for relative residual of

$$\frac{\| \mathbf{R} \|_2}{\| \mathbf{R}_i \|_2} < 10^{-7},$$

where $\mathbf{R}_i$ denotes initial residual of the discretized system. Sensitivity of the developed code to grid resolution is summarized on Table 5.2: According to the sensitivity check, even 71×71 number of cells gives acceptable order of accuracy. The difference between the lowest resolution and the highest one (81×20 vs 128×128) is computed as 4/1000 which guarantees precise calculations. It should be noted that, most of the simulations for Burnett equations are performed for 81×20 cells due to reported numerical instabilities of Burnett equations. Figure 5.3 shows convergence history of NS equations for specified conditions. All simulations of this section are performed for Cercignani model including first- and second-order slip terms mentioned in Table 2.1. Making use of the second-order slip model allows to getting accurate solutions at transition region of the Knudsen regime. The same boundary conditions has also been employed by Stefanov *et al.* (2002a) Since the only difference between the NS and Burnett equations are the higher-order stress terms, the best starting point will be the comparison of the first-order and higher-order stress tensors of the Burnett equations. Note that the gravity effect is neglected in all simulations.

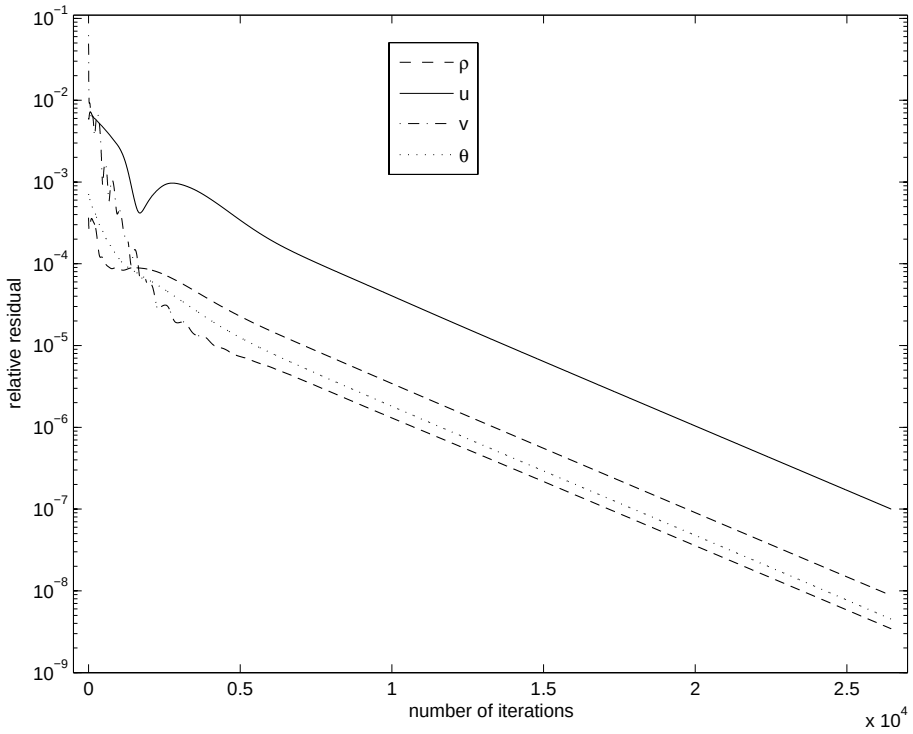

Figure 5.3. Relative residual history of NS for $Kn = 0.1$, $CFL = 0.2$ and 81×20 cells

Some cases studied are summarized as the following:

- **Case 1** Burnett Model $Kn = 0.1$, 81×20 cells, $\epsilon = 0.1$, $r_T = 0.6$, $CFL = 0.02$ and $\epsilon r_T = 0.06$.

- **Case 2** Burnett Model $Kn = 0.2$, 81×20 cells, $\epsilon = 0.1$, $r_T = 0.6$, $CFL = 0.02$ and $\epsilon r_T = 0.06$.

- **Case 3** Burnett Model: $Kn = 0.1$, 81×20 cells, $\epsilon = 0.1$, $r_T = 0.5$, $CFL = 0.02$ and $\epsilon r_T = 0.05$.

- **Case 4** Burnett Model: $Kn = 0.1$, 81×20 cells, $\epsilon = 0.1$, $r_T = 0.7$, $CFL = 0.02$ and $\epsilon r_T = 0.07$.

- **Case 5** Navier-Stokes Model: $Kn = 0.1$, 81×20 cells, $\epsilon = 0.1$, $r_T = 0.6$, $CFL = 0.02$ and $\epsilon r_T = 0.06$.

- **Case 6** Navier-Stokes Model: $Kn = 0.2$, 81×20 cells, $\epsilon = 0.1$, $r_T = 0.6$, $CFL = 0.02$ and $\epsilon r_T = 0.06$.

5.2.5.1. Comparison of Burnett Shear Stresses. Since, the flow is likely to be shear-driven flow we will focus on only shear stresses of Burnett model in this section. Figure 5.4 shows streamlines for Case 1. Subsequently we show first- and second-order stress tensors of Burnett equations in Figures 5.5 and 5.6. Streamline patterns appeared in Figure 5.4 show a small deviation from conservation of mass due to coarse cells. It can be seen that, the flow is only managed by the first-order shear stress of $\tau_{xy}^{(1)}$ compared with its second-order pair. Effect of second-order stress term is only sensible on the corners of the flow domain due to sharp change of the flow characteristic. Figure 5.5 also points out that there is a *shear-layer* in the core regions of the flow. As we can see in the proceeding paragraphs, thermal creep flow of rarefied gases shows close similarity to Couette flow. While $\tau_{xy}^{(1)}$ has negative values on the bottom boundary, it changes to positive values with increasing trend. Let's look shear stresses of Case 2. shown in Figures 5.8 and 5.9. Increase in Kn number leads to variations on the slope of $\tau_{xy}^{(1)} = constant$ curves. Such a behavior can also be seen in Figure 5.7. Figure

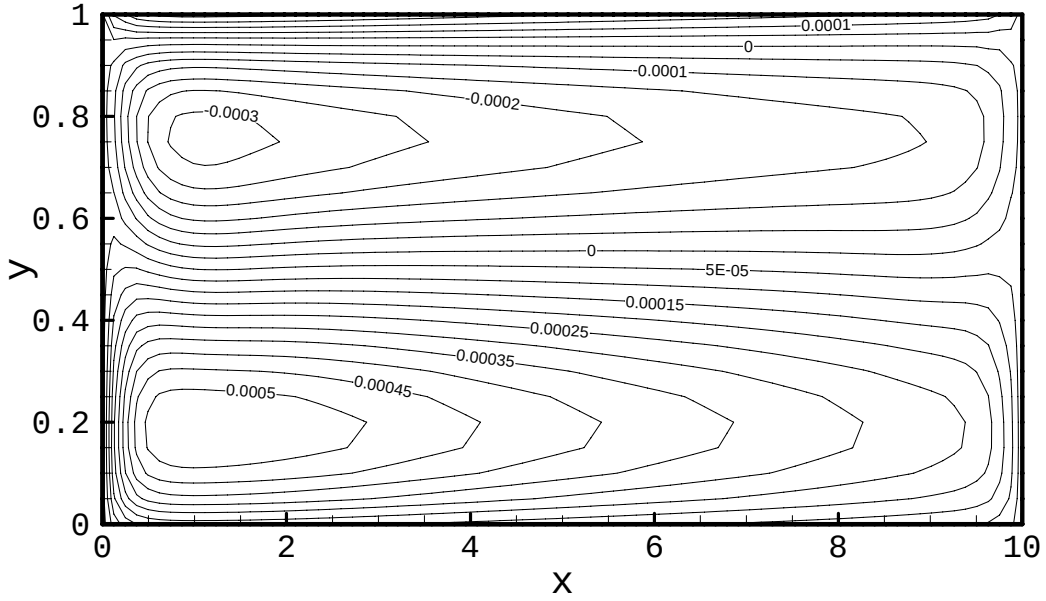

Figure 5.4. Streamlines for $Kn = 0.1$, 81×20 cells, $\epsilon = 0.1$, $r_T = 0.6$, $CFL = 0.02$

5.10 shows wall shear stresses order of one and two. First-order shear stress shows sudden raise as flow develops and goes down in the vicinity of the right vertical wall.

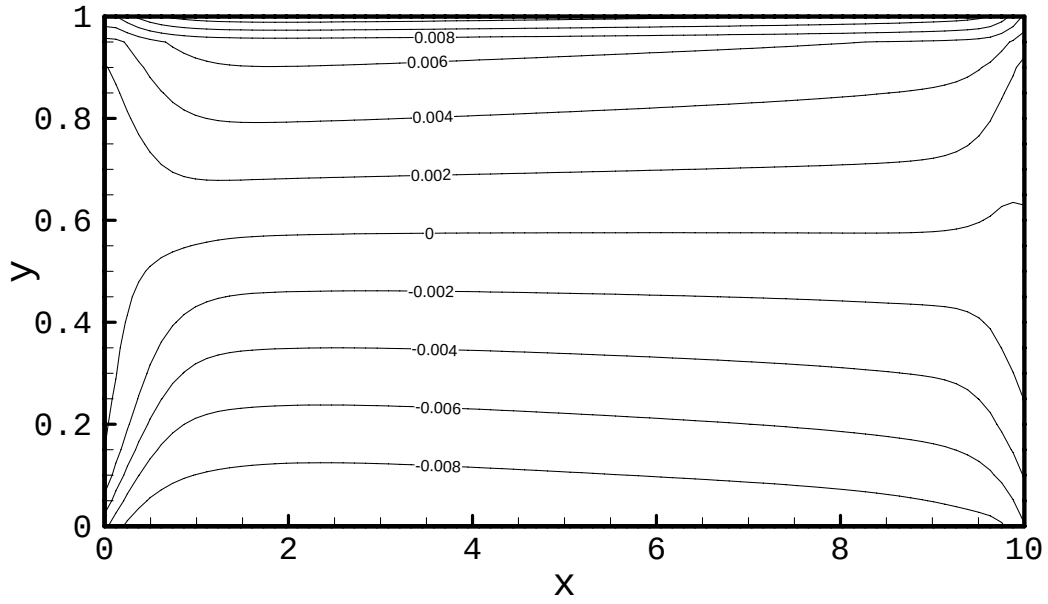

Figure 5.5. First-order shear stress component, $\tau_{xy}^{(1)}$, for $Kn = 0.1$, 81×20 cells, $\epsilon = 0.1$, $r_T = 0.6$, $CFL = 0.02$

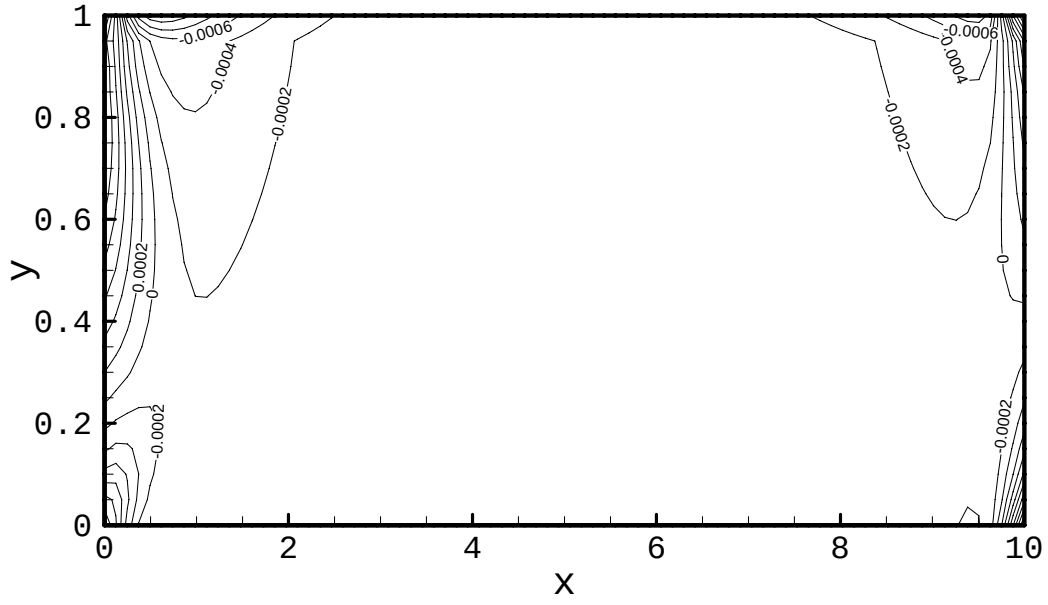

Figure 5.6. Second-order shear stress component, $\tau_{xy}^{(2)}$, for $Kn = 0.1$, 81×20 cells, $\epsilon = 0.1$, $r_T = 0.6$, $CFL = 0.02$

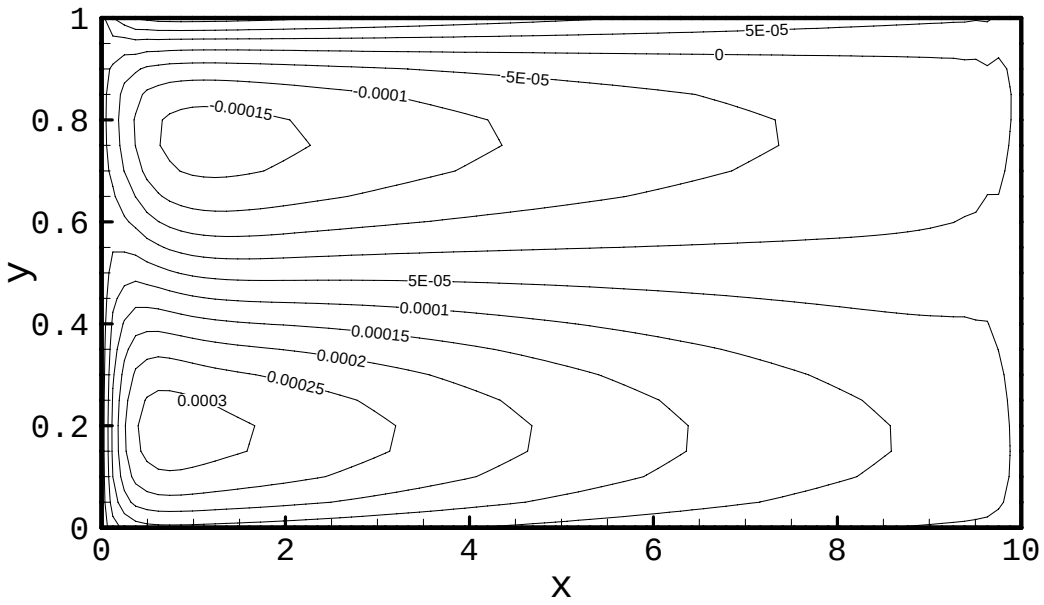

Figure 5.7. Streamlines for Case 2

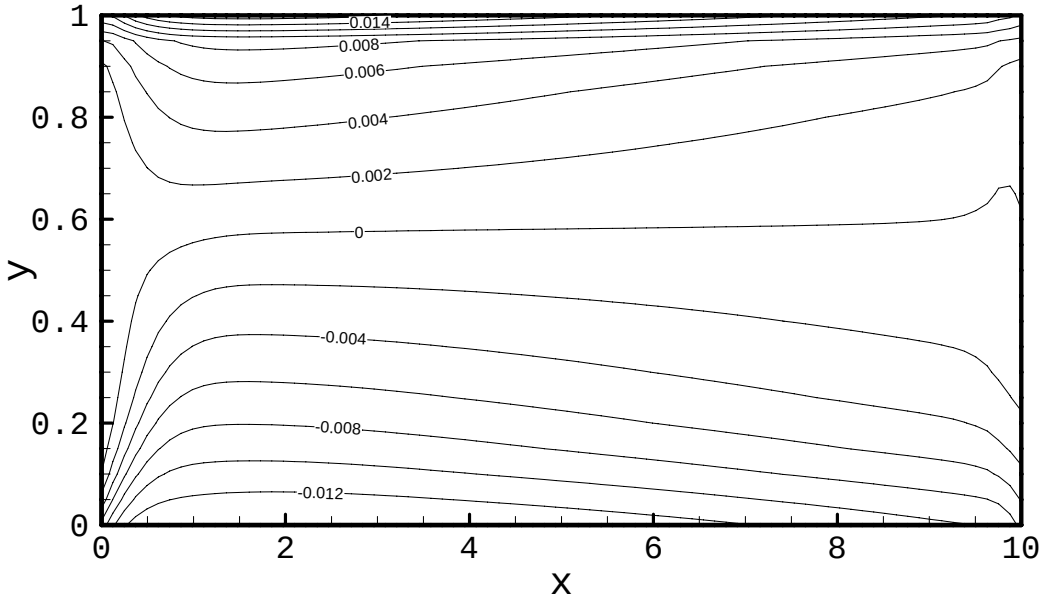

Figure 5.8. First-order shear stress component, $\tau_{xy}^{(1)}$, for Case 2

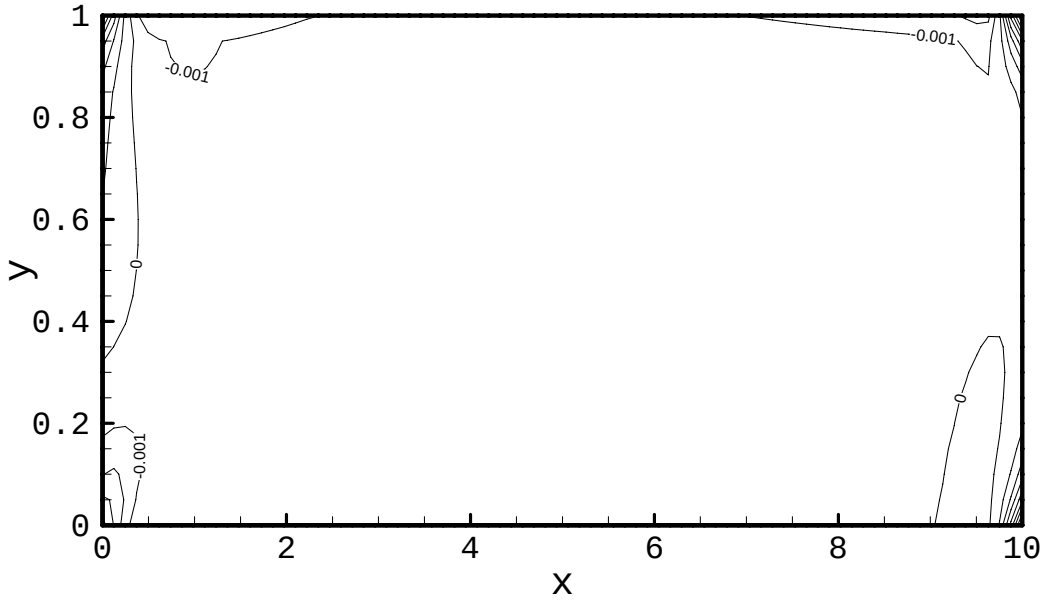

Figure 5.9. Second-order shear stress component, $\tau_{xy}^{(2)}$, for Case 2

On the other hand, second-order wall shear can be ignored in the domain with only one exception, on the corners of the wall. Notice that, the effect of adiabatic BC on the bottom wall leads to different shear values compared with top boundary. Figure 5.11 declares that the current flow can be accounted as purely shear-driven. While, the first order shear stress, τ_{xy}^{1} varies linearly along the y direction of the enclosure, second-order term, τ_{xy}^{2} can be ignored. Temperature field of the Case 1 is shown in Figure 5.12 Let's consider normal stress terms of Burnett equations. shown in Figures 5.13-5.16. Notice, order of magnitudes of Burnett normal stresses which are negligible compared with the shear stresses. Clearly, there is no necessity to go into the details of normal stresses. In the next section, we will make a comparison between the NS and Burnett equations.

5.2.5.2. Comparison of Navier-Stokes and Burnett solutions. In this section we will try to inspect discrepancies between the NS and Burnett equations solutions. For this purpose we consider again Case 1 and Case 5.

In Figure 5.17, streamlines of NS and Burnett equations have been compared. As it can be seen, there is a significant difference introduced by two mathematical model. In order to see the details of the differences we will look at shear stresses

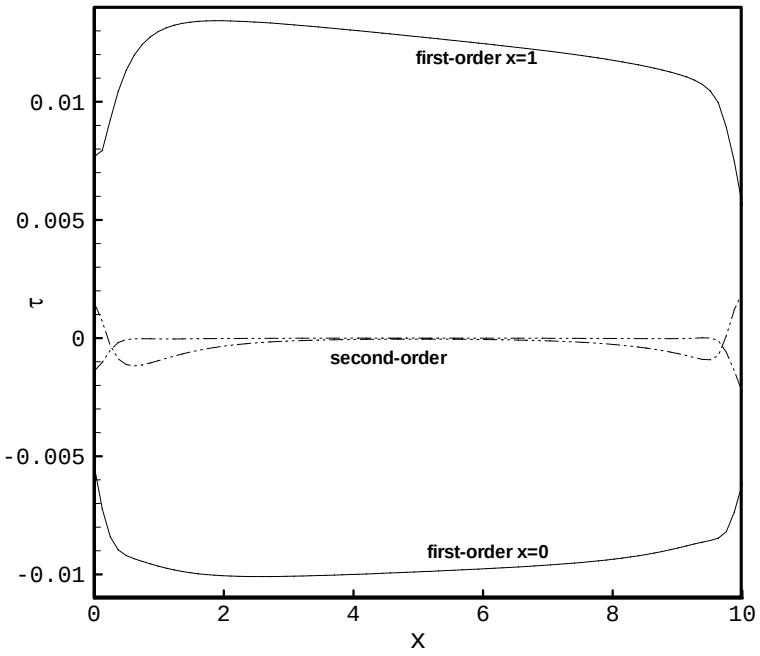

Figure 5.10. Shear components, $\tau_{xy}^{(i)}$, for $i = 1 \ldots 2$ along the bottom and top boundaries, $Kn = 0.1$, 81×20 cells, $\epsilon = 0.1$, $r_T = 0.6$, $CFL = 0.02$

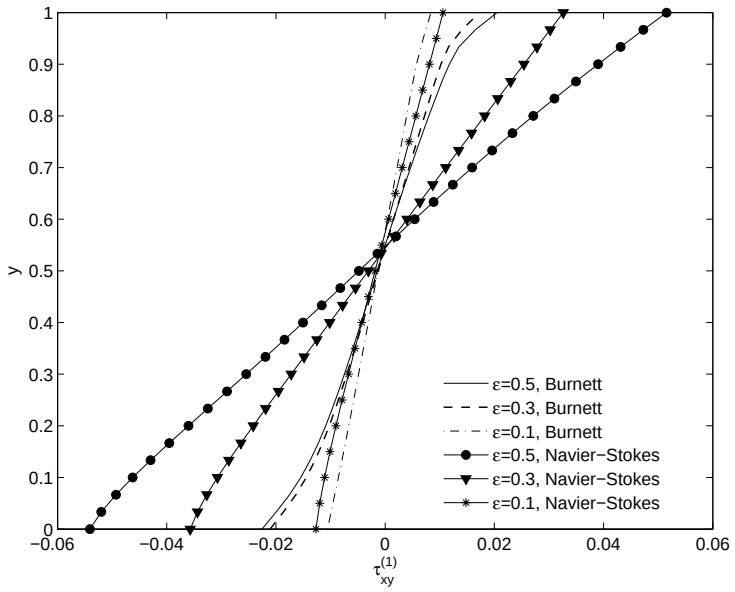

Figure 5.11. The first-order shear stress $\tau_{xy}^{(1)}$ along the depth of the enclosure on the horizontal centers with aspect ratios $\epsilon = 0.5$, $\epsilon = 0.3$ and $\epsilon = 0.1$ for $Kn = 0.11$ and $r_T = 0.5$

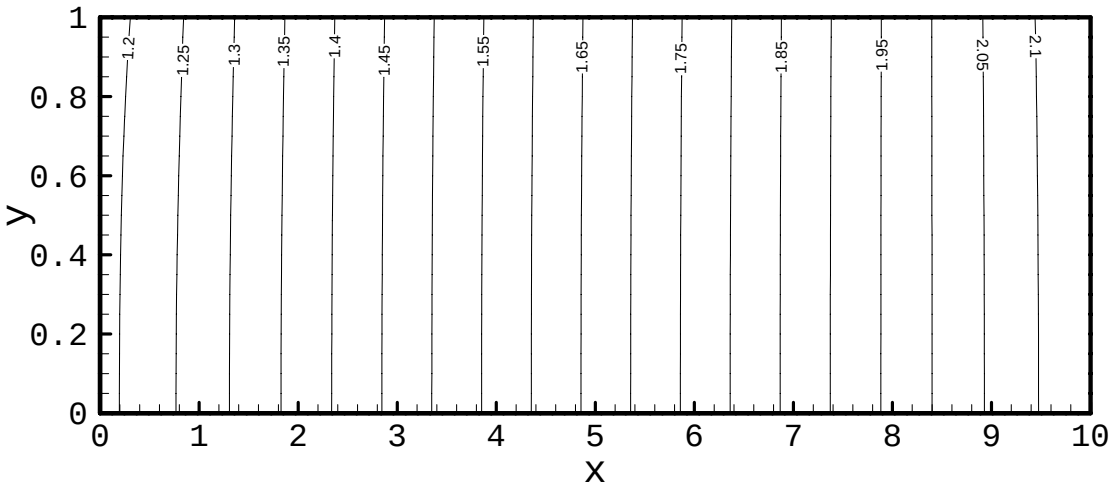

Figure 5.12. Variation of temperature, θ, for $Kn = 0.1$, 81×20 cells, $\epsilon = 0.1$, $r_T = 0.6$, $CFL = 0.02$

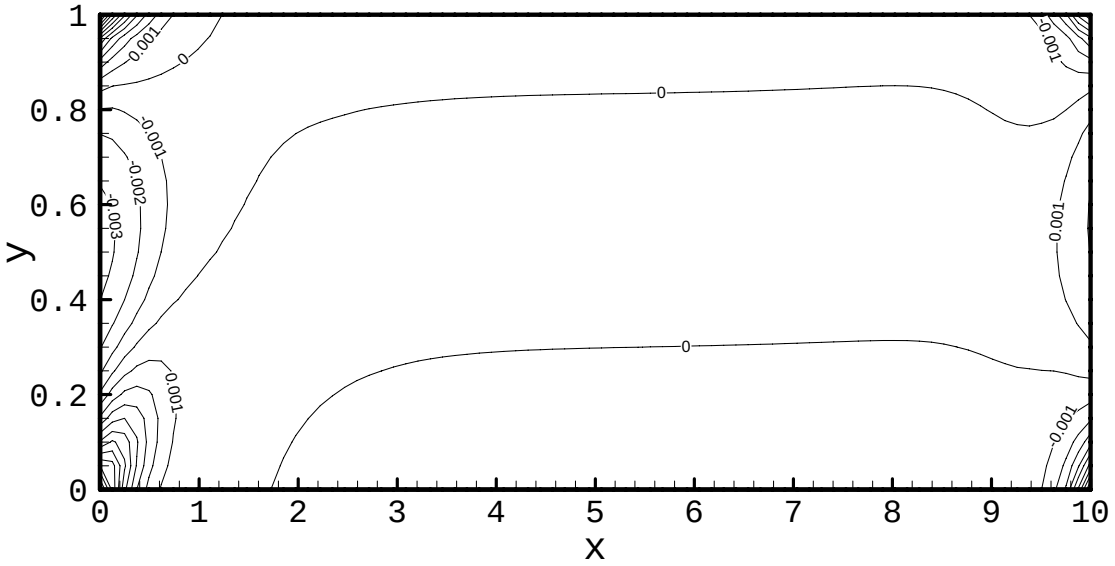

Figure 5.13. First-order x-wise normal stress component,$\tau_{xx}^{(1)}$, for $Kn = 0.1$, 81×20 cells, $\epsilon = 0.1$, $r_T = 0.6$, $CFL = 0.02$

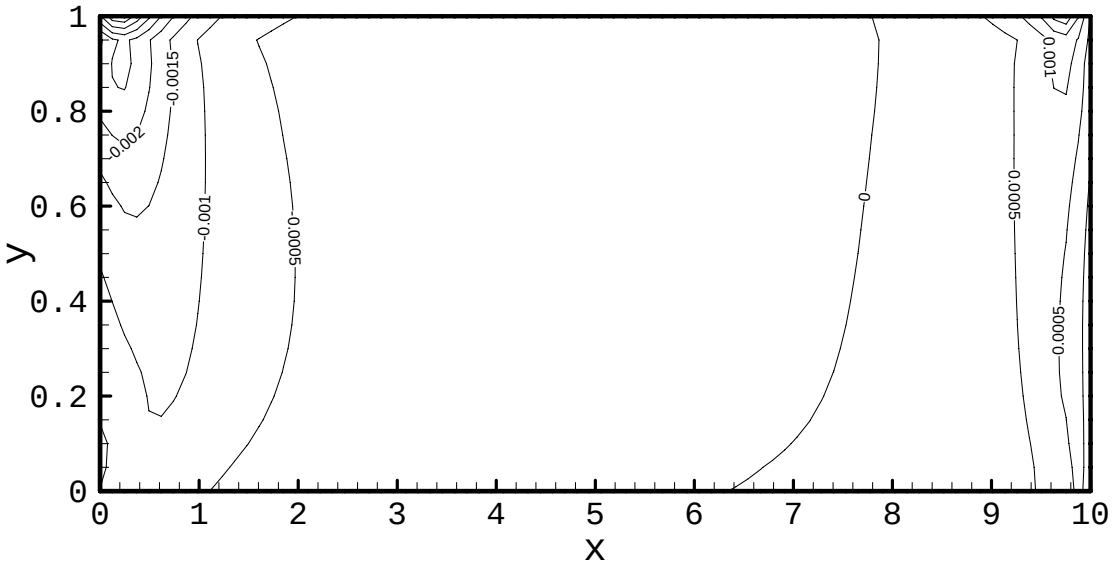

Figure 5.14. Second-order x-wise normal stress component, $\tau_{xx}^{(2)}$, for $Kn = 0.1$, 81×20 cells, $\epsilon = 0.1$, $r_T = 0.6$, $CFL = 0.02$

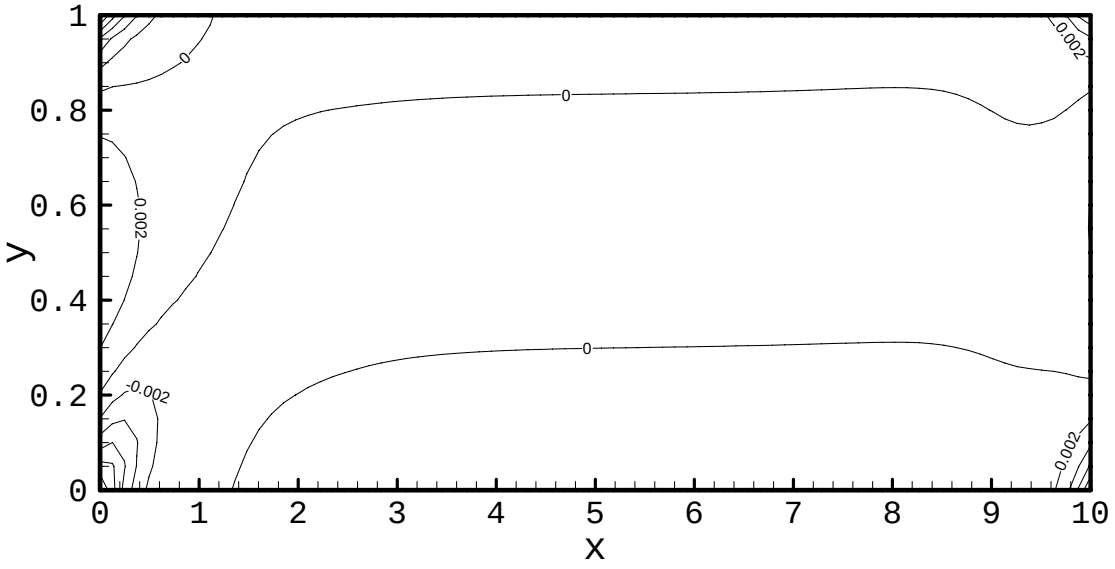

Figure 5.15. First-order y-wise normal stress component, $\tau_{yy}^{(2)}$, for $Kn = 0.1$, 81×20 cells, $\epsilon = 0.1$, $r_T = 0.6$, $CFL = 0.02$

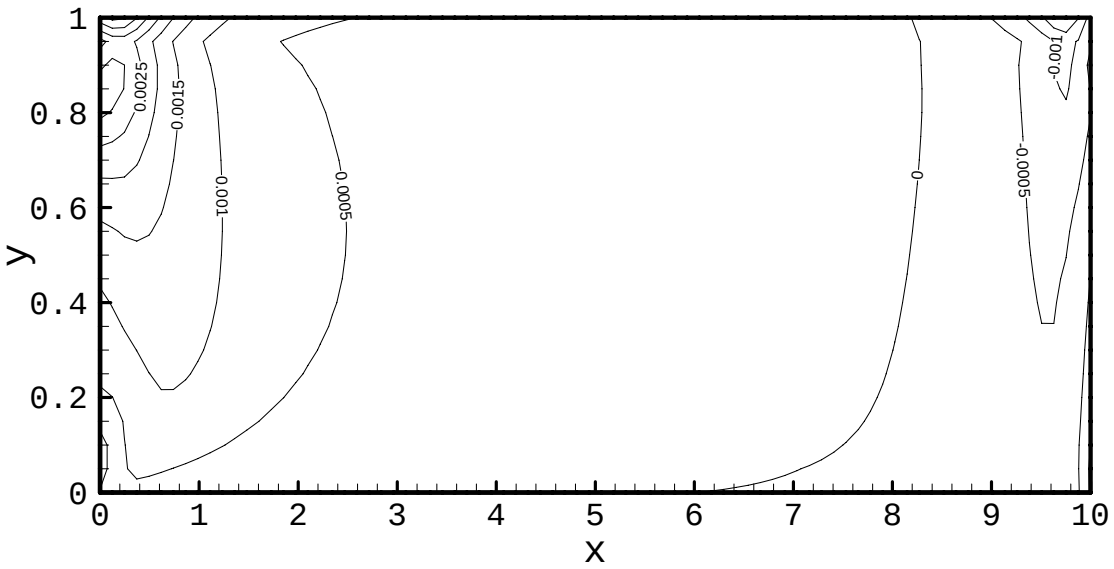

Figure 5.16. Second-order y-wise normal stress component, $\tau_{yy}^{(2)}$, for $Kn = 0.1$, 81×20 cells, $\epsilon = 0.1$, $r_T = 0.6$, $CFL = 0.02$

in two cases. Figure 5.18 compares the first-order shear stresses of NS and Burnett equations. $\tau_{xy}^{(1)} =$ constant curves of both model appears in the different locations of the domain. $\tau_{xy}^{(1)} = 0$ curves of each models are coincides at the same location. In order to see the differences between both model we refer to Figure 5.19. As we can see NS wall shear gives higher magnitudes than Burnett equations and its variation becomes negligible in the core region of the enclosure. However, Burnett model gives rise to tremendous decline in the positive x direction. Apparently, the distinction between the NS and Burnett models are the second and third-order terms of the stress tensors. Due to strong coupling of these terms with the convective terms, there is no any way for getting the correct answer to understand how they affects the flow patterns. As mentioned above, due to thermal jump effects on the top boundary, both wall shears change their values at the same location, as well. Pressure distribution along the center-line of the enclosure is shown in 5.20. Since, the flow is likely to be a creeping flow, compressibility effects do not play any role in the pressure distribution which is almost linear. Due to end effects on the vertical sides where the flow turns around itself very small non-linearity is observed.

Now we introduce u slip on horizontal walls. Velocity slip region can be divided into three distinct region, shown in Figure 5.21:

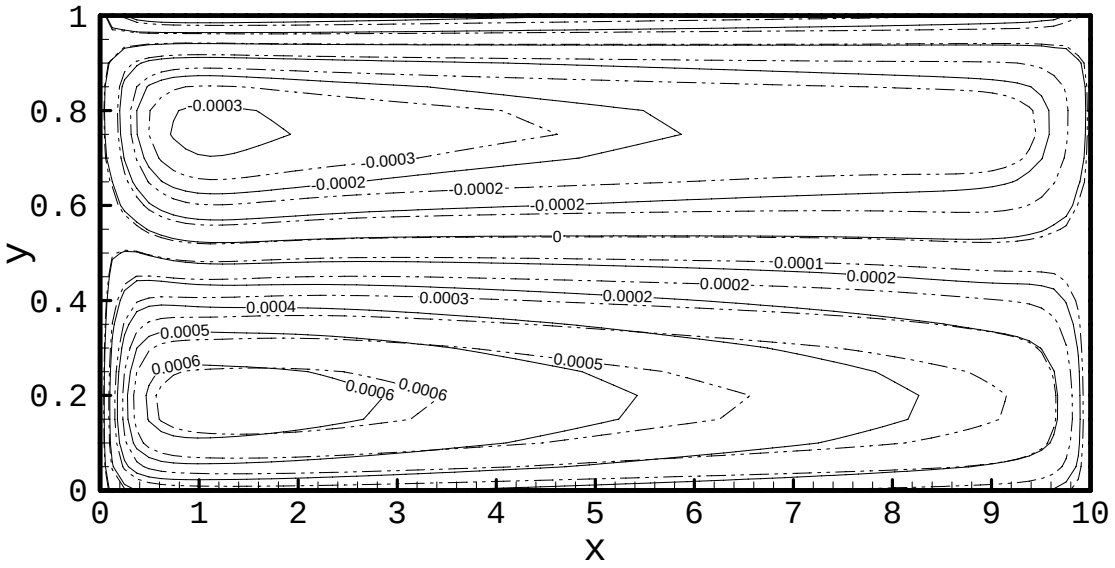

Figure 5.17. Comparison of streamlines for NS and Burnett equations, $Kn = 0.1$, 81×20 cells, $\epsilon = 0.1$, $r_T = 0.6$, $CFL = 0.02$ (dash-dot-dot denotes NS)

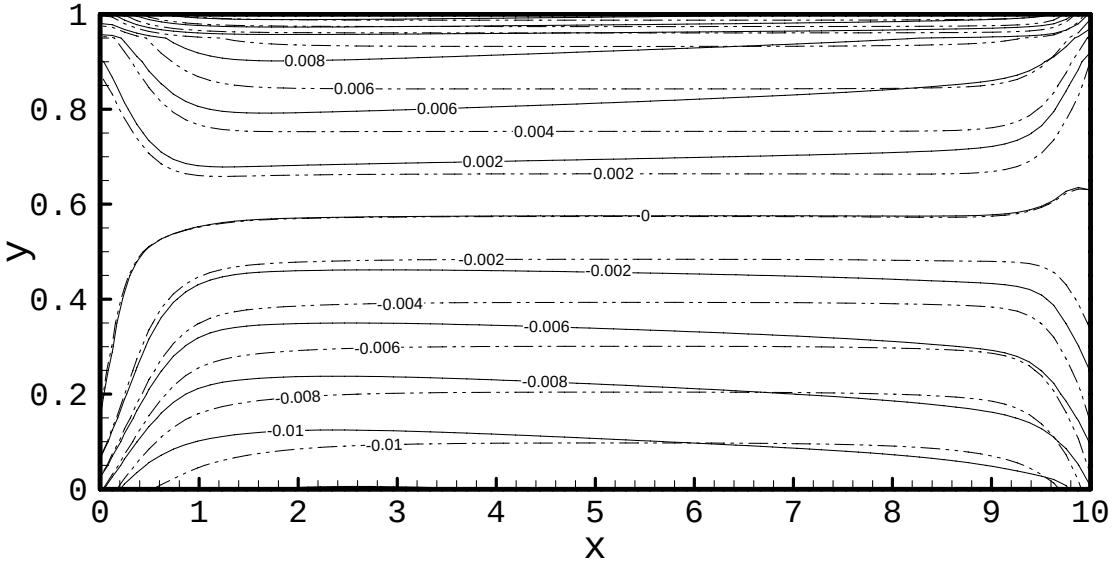

Figure 5.18. Comparison of $\tau_{xy}^{(1)}$ for NS and Burnett equations, $Kn = 0.1$, 81×20 cells, $\epsilon = 0.1$, $r_T = 0.6$, $CFL = 0.02$ (dash-dot-dot denotes NS)

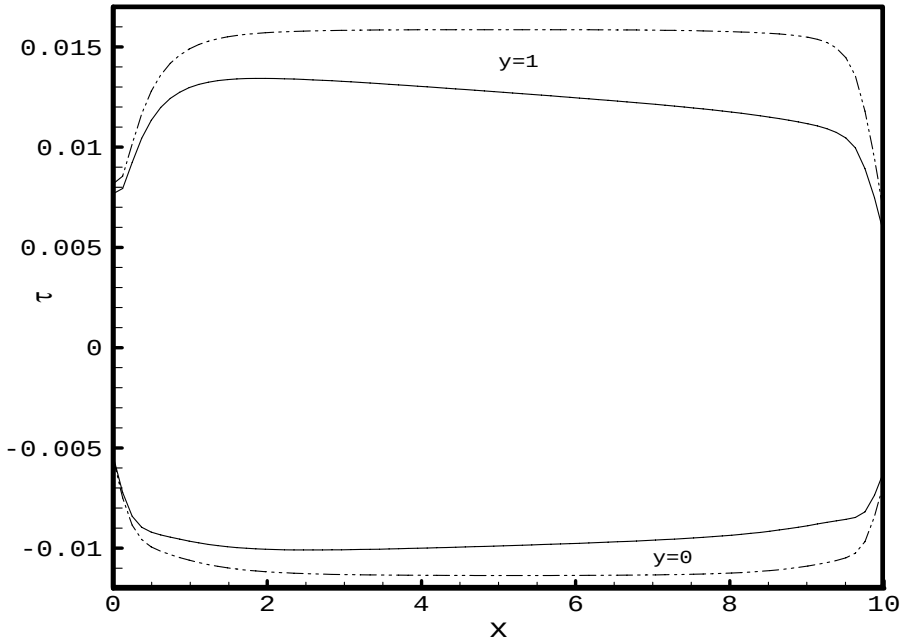

Figure 5.19. Comparison of $\tau_{xy}^{(1)}$ on horizontal boundaries for NS and Burnett equations, $Kn = 0.1$, 81×20 cells, $\epsilon = 0.1$, $r_T = 0.6$, $CFL = 0.02$ (dash-dot-dot denotes NS)

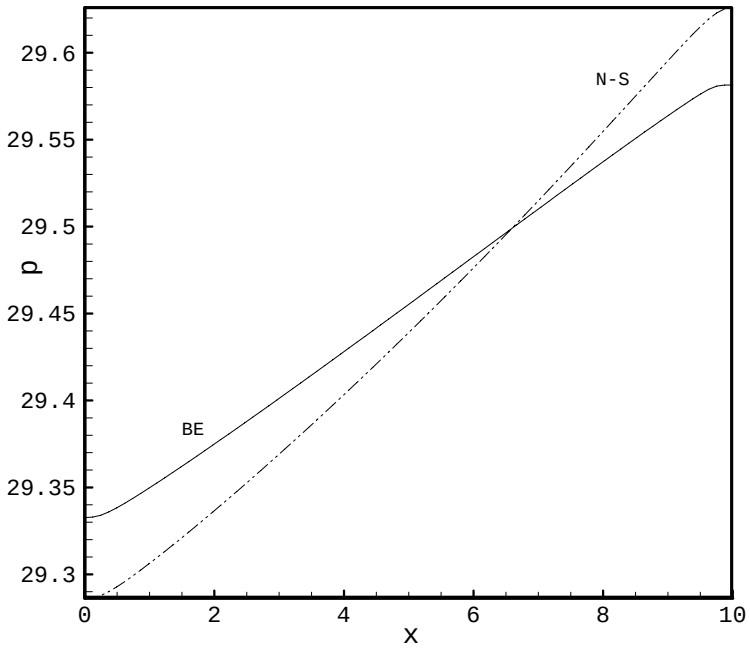

Figure 5.20. Pressure distribution at $y = 0.5$ for NS and Burnett equations, $Kn = 0.1$, 81×20 cells, $\epsilon = 0.1$, $r_T = 0.6$, $CFL = 0.02$ (dash-dot-dot denotes NS)

- hydrodynamic entry region on the left hand side (denoted by I in the figure),
- hydrodynamically fully developed core flow region, and
- a region where the flow is suspended.

As seen from Figure 5.21, slip velocity is governed approximately in region I. Then it shows slightly diminishes until reaches to proximity of right wall and then suppressed tremendously due to mass continuity requirement. Notice that, on the bottom boundary bigger slip velocity takes place than the top wall. This is due to different temperature gradients as mentioned in Section 3.6. On the other hand, note that, the differences between the maximums of slip velocities are 3.10 % and 3.91 % for $Kn = 0.1$ and $Kn = 0.2$, respectively. The effect of horizontal temperature gradient is sketched

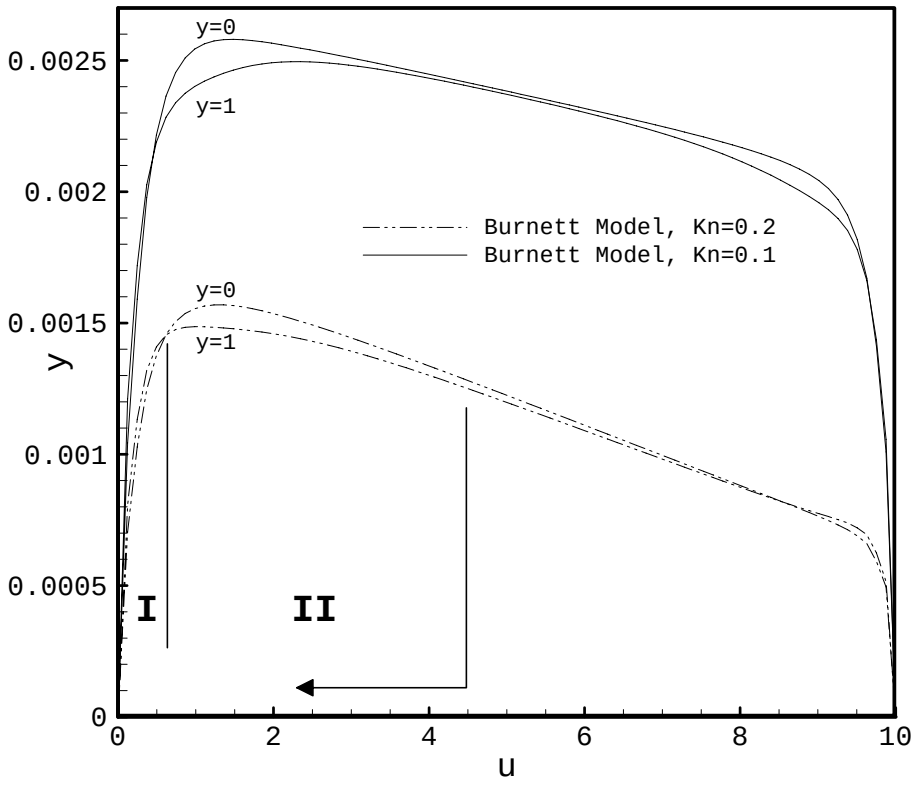

Figure 5.21. Slip of u along the horizontal walls, NS Model, $Kn = 0.1$, $Kn = 0.2$, 81×20 cells, $\epsilon = 0.1$, $r_T = 0.6$, $CFL = 0.02$

in Figure 5.22. As it can be seen from the figure, u velocity increases with temperature gradient proportionally.

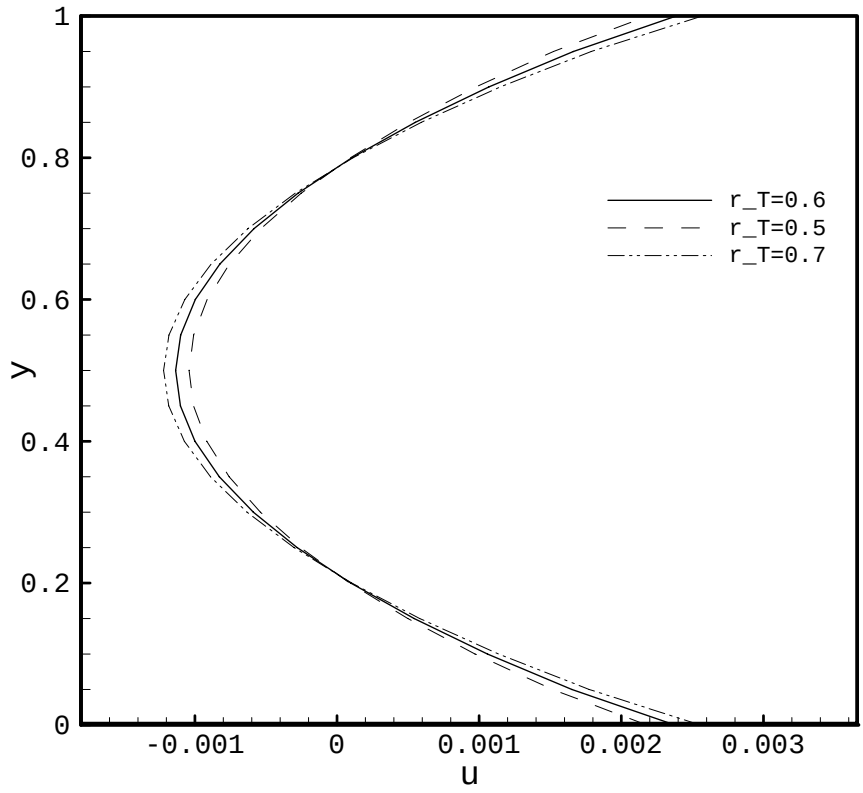

Figure 5.22. u velocity along the y direction at $x = 0.5$ for varying r_T, Burnett model, $Kn = 0.1$, 81×20 cells, $\epsilon = 0.1$, $CFL = 0.02$

Let's illustrate, the u velocity distribution along the vertical direction for $Kn = 0.1$ and $Kn = 0.2$ (Case 1, 2, 5 and 6) in Figure 5.23. The velocity profile is almost parabolic and Burnett model gives smaller values than Navier-Stokes. In case of $Kn = 0.1$ the difference between two models is approximately 26.6 % at $y = 0.5$. On the other hand, for $Kn = 0.2$ the difference between them increases to 72.2 %. As Kn is amplified, such a decline in maximum velocity which takes place on the wall surface; as reported by Papadopoulos *et al.* (1995). They point out confinement effect as the reason of such a velocity decrease. With their words;

"Physically, for Knudsen numbers in the range shown, the kinetic layers are comparable with the dimensions of the cavity and hence there is non-negligible interaction between them and between the kinetic layers and the existing vortex."

Namely, they refers to interaction between the Kn layer (grows with Kn number) and flow vortex. Since, the flow is likely to be shear driven, the chief reason in the drop of velocity is viscous diffusion. Linear variation of first-order shear-stress along the depth

supports this hypothesis. Let's consider the relation between Re and Kn number

$$Re = \frac{\sqrt{r_t}}{Kn}.$$

Absolutely, rise in Kn number make diffusive terms more important than the convection terms in the conservative equations. Both the author of this thesis and Papadopou-

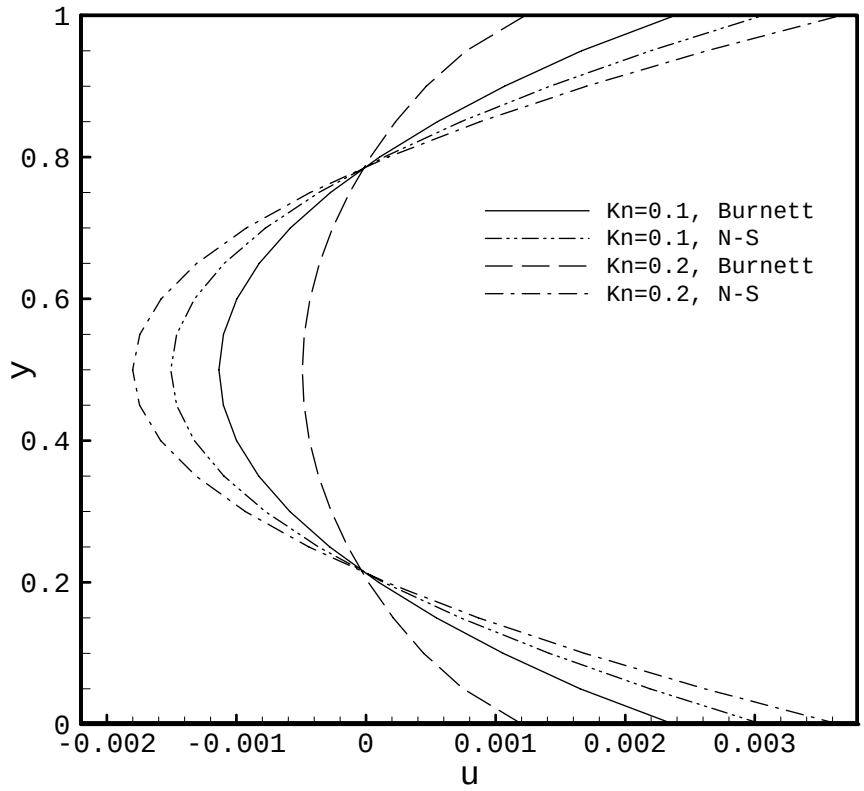

Figure 5.23. u velocity along the y direction at $x = 0.5$ for NS and Burnett equations for $Kn = 0.1$, $Kn = 0.2$, 81×20 cells, $\epsilon = 0.1$, $r_T = 0.6$, $CFL = 0.02$

los *et al.* (1995) question the validity of Navier-Stokes system in thermally-driven flow type. Only, higher-order description of constitutive equations, Burnett equations, can correctly model these creeping flows for larger Kn numbers. Deviations of Navier-Stokes solutions are so large as much as intolerable. From Figures 5.24 and 5.25, we see that, as Kn number increases the maximum u velocity predicted by Navier-Stokes equations also increases nonlinearly up to certain levels and then remains approximately constant. However, the velocity predicted by the Burnett equations decreases continuously in contrast to Navier-Stokes equations. Since, the temperature gradient along the x direction, $\frac{\partial \theta}{\partial x}$, is also affected by the aspect ratio of the enclosure, for the

same overheat ratios and Kn numbers, higher values of aspect ratio ϵ lead to greater slip velocities. Moreover, non-linear increasing trend of the predicted velocity originates from the interaction between the core flow and turning flow at the ends, which is less important for the smaller aspect ratios. It should be noted that for $Kn \geq 0.17$, the velocity u_{max} takes the same value for different overheat ratios (Figure 5.24).

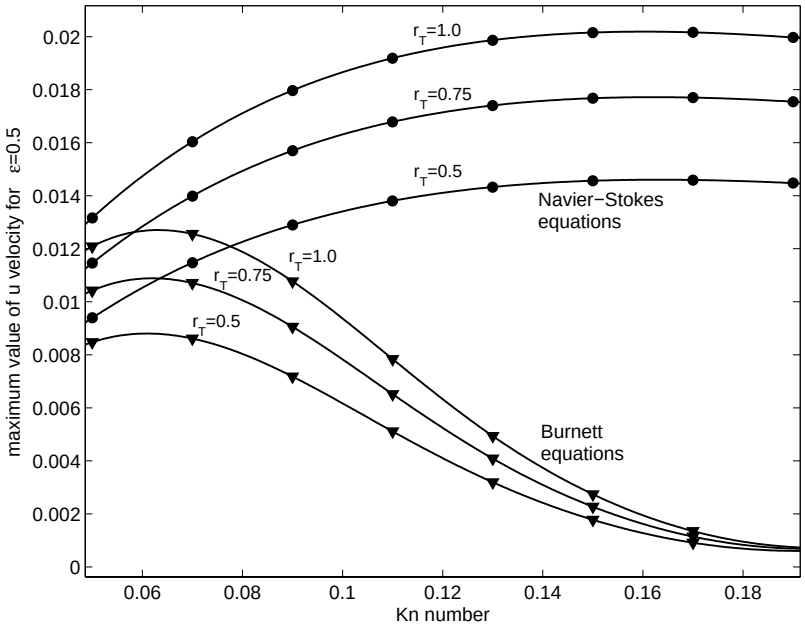

Figure 5.24. Variation of maximum x-wise velocity component with respect to different rarefaction levels and overheat ratios for $\epsilon = 0.5$

Analogous to our findings, the strange behavior of the maximum velocity has also been reported in (Papadopoulos *et al.* 1995). For comparison, we have performed additional simulations with Xenon having the following thermo-physical properties: $c_p = 158.0$ J/kgK, $k = 252.0 \times 10^{-3}$ W/mK, $\mu = 44.0 \times 10^{-6}$ Ns/m^2 (specified at 100 kPa) and $Pr = 0.0322$. Note that, the thermal transpiration velocity $u_c = \omega\sqrt{(2R/T)}dT/dx$ is used as a scaling parameter for the u velocity, where ω is a thermal slip coefficient. From the results, it is observed that not only Navier-Stokes but also Burnett equations have underestimated the maximum velocity with respect to that of DSMC method (Figure 5.26). The "confinement" effect is the principal reason of the unexpected behavior of the velocity change according to Papadopoulos *et al.* (1995). Contrary to their reasoning, we believe that viscous diffusion predicted by Burnett model produces such a reduction in the maximum creep velocity. Momentarily, let's ignore the slip due to momentum accommodation (set A_1 and A_2 to zero); then the flow mechanism is

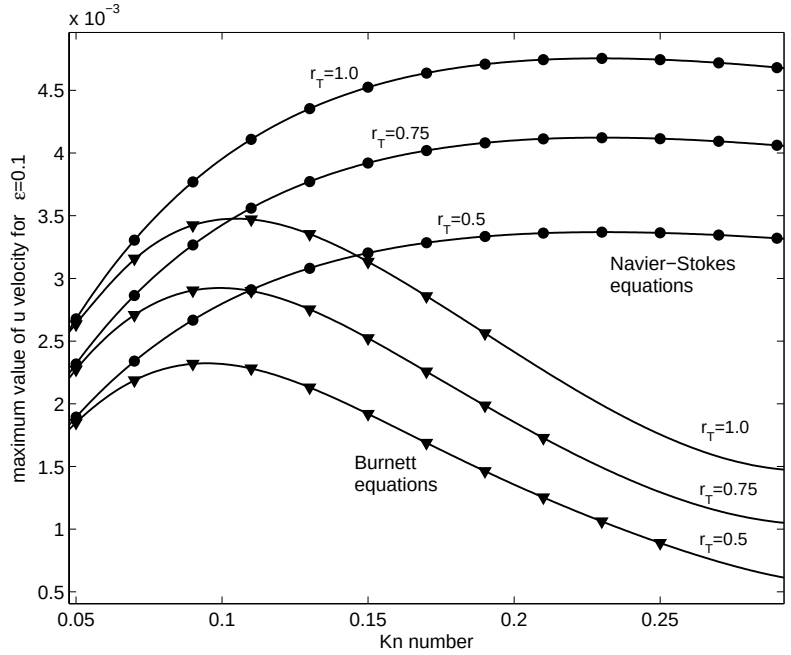

Figure 5.25. Variation of maximum x-wise velocity component with respect to different rarefaction levels and overheat ratios for $\epsilon = 0.1$

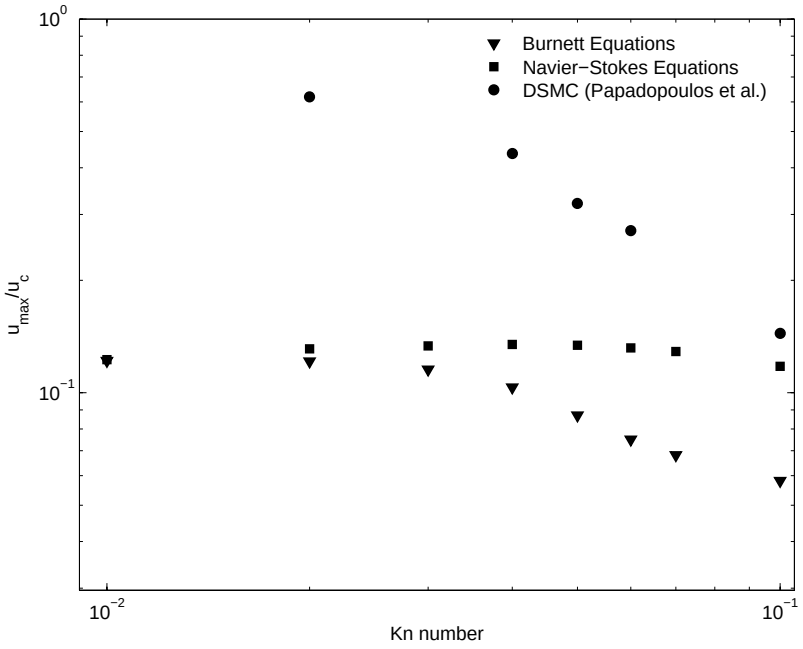

Figure 5.26. Variation of the non-dimensional maximum velocity with Kn number. Xenon was chosen as the working fluid and the gradient of dT/dx was kept constant along the horizontal walls for comparison with some selected DSMC data of Papadoupoulos *et. al.* The computations have been carried out for $Kn \leq 0.1$.

converted to a simple two-sided lid-driven cavity problem with the lid velocity of u_c. In this case, the flow field mainly depends on the magnitude of the Kn number which can be viewed as a parameter adjusting lid velocity. In this case, larger Kn numbers create the stronger velocity field as expected. On the other hand, allowing a velocity slip (equivalent to the slip due to the momentum accommodation) on the lids ends up in the same problem that we have tried to analyze. At this stage, the wall shear stress comes into picture together with the rarefaction effects (represented by Kn number in the slip boundary condition). Therefore, thermal creep flow can be assumed as a shear driven flow in which viscous diffusion becomes more important. This was the reason why Burnett and NS equations could't constitute with each other. Contributions of thermal stress terms available in the second and augmented orders lead to tremendous changes in the behavior of thermal creep flow (Golshtein *et al.* 1996). Because in the vanishing limit of the Kn number both models of hydrodynamics predict the same creep velocity, where the effect of thermal stresses seems to be suspended. On the other hand, there is a significant disagreement between the results of Burnett simulations and DSMC of (Papadopoulos *et al.* 1995) (Figure 5.26). A reason for the deviation can be addressed to the relatively low Pr number of Xenon.

6. CONCLUSIONS AND FUTURE PERSPECTIVES

This thesis contemplates thermal creep driven convection of rarefied gases in enclosures. Studied categories are summarized as

- asymptotic analysis of the convective flow,
- analysis of possible hydrodynamic instabilities by make use of linear stability theory and
- numerical simulations of Navier-Stokes and Burnett models for proposed flow.

In the first part of the thesis, we performed an asymptotic analysis to get analytical solutions in the geometry. For this purpose, the gas has been assumed as an incompressible fluid and a small perturbation parameter, in fact aspect ratio of the enclosure, was introduced and then the solution was expressed in terms of regular asymptotic expansion of this small parameter. The problem was divided into two sub-problems, namely inner and outer expansions due to singularity of the problem. The singularity has been eliminated by making the use of method of asymptotic matches. After joining inner and outer solutions we have obtained a global solution valid in the whole enclosure. We have also found analytical solutions for the flow variable valid on the core region where the flow does not show sharp changes. Asymptotic analysis allows us the following results:

- An hydrodynamic boundary layer has been recognized on both horizontal walls of the enclosure. Kn number is the main parameter affecting the entry length of the boundary layer.
- Temperature jump on the vertical walls due to horizontally applied thermal gradient, bears two different vortexes on the bottom and top halves of the enclosure.
- As Re number increases, temperature jump also increases.

Since the current study also proposes that there may be a convective instability, we have performed linear stability analysis in two and three-dimensions. Assuming

small perturbations to the basic flow, we have employed linear approximation of hydrodynamic stability theory. This was the first accomplishment in searching the limits of proposed instability. Stability of the flow axisymmetric disturbances was studied in two-dimensions. The results in two-dimensions read as:

- Decrease in Pr number leads to slight increases in the limits of the instability.
- Slip models highly affect critical states.
- Instability threshold varies non-linearly with Kn number. Increase of Kn number results in considerable amount of decline in critical Reynolds numbers. The analysis in terms of Kn number is restricted up to the 0.4 due to invalidity of continuum mechanics beyond this limit.

We also studied three dimensional analysis of the possible instabilities. For this purpose, perturbation mode equations are disctretized by making use of the fourth-order finite difference method and artificial compressibility concept, resulting GEP is solved via QZ algorithm. Due to the dominance of the spurious eigenvalues we could not search neutral states. On the other hand, we conclude that, artificial compressibility works well even for moderate artificial $\tilde{M}a$ numbers. Spectral methods are suggested in order to ensure accurate GEP calculations of the problem.

In the last, we have simulated this non-isothermal driven flow mechanism by use of Navier-Stokes and Burnett models. Both governing equations discretized via finite volume methodology and the resulting linear set of algebraic equations are solved under the specified boundary conditions. We end up with the following consequence:

- Linearly varying temperature of the top wall leads to smaller slip velocity due to rarefaction effects compared to the adiabatic bottom wall.
- The velocity slip increases with decreasing aspect ratios. Moreover, increase in overheat ratio also leads to increase in the creep velocity.
- Navier-Stokes and Burnett models have predicted different flow fields. The contradiction between two models becomes more obvious when inspecting the maximum creep velocity that takes place on the horizontal surfaces. The difference

between the predictions of both models enlarges as Kn number increases.

- In contrast to our expectations, for higher rarefaction degrees the maximum slip velocity resulting from Burnett equations decreases gradually with increasing Kn numbers (with the exception of a certain amount of non-linear increase near the continuum limit).
- Such a reduction trend of the maximum slip velocity has also been pointed out by Papadopoulos *et al.* (1995). In contrast to their justifications for the decrease of the maximum slip velocity with increasing Kn number, to the authors' knowledge, totally diffusive nature of the flow is the fundamental reason. There is no doubt that thermal stress terms (especially first order gradient of the temperature $\partial\theta/\partial x$) become effective in the predictions of Burnett model. However, effects of these thermal stresses become negligible in the continuum limit. On the other hand, verification of an intolerable gap between the results of Burnett model and DSMC necessitates more researches on this topic.
- This study demonstrates that Navier-Stokes equations fail to predict the thermal creep flow in the closed geometries for moderately high rarefaction levels.

We aim to extend and identify important aspects of thermal creep flow. At first, we would like to answer the question of whether there exists an instability or not for this flow type. Direct Numerical Simulation should be employed for the search of neutral states. Extending stability analysis by studying different aspects (proof of exchange of stabilities etc.) of the hydrodynamic stability is another alternative for the future works.

APPENDIX A: A FOURTH-ORDER COMPACT FINITE DIFFERENCE SCHEME FOR BIHARMONIC EQUATIONS

Consider a Dirichlet problem for the Biharmonic equation such that

$$\nabla^4 \Psi = s\,(x,y) \qquad (x,y) \in \Omega, \tag{A.1}$$

$$\Psi = f\,(x,y)\,, \quad \frac{\partial \Psi}{\partial n} = f\,(x,y) \qquad (x,y) \in \partial\Omega \tag{A.2}$$

where Ω is a closed convex domain in two dimensions and $\partial\Omega$ is its boundary. Biharmonic equation is discretized using a 25-point stencil with truncation error $O\,(h^4)$, (Altas *et al.*, 1998). The discrete form is given in terms of the unknown functions Ψ, Ψ_x and Ψ_y

$$\begin{aligned}
\Psi_{i,j} \;=\; & +\frac{3}{11}(\Psi_{i+1,j}+\Psi_{i,j+1}+\Psi_{i-1,j}+\Psi_{i,j-1}) \\
& -\frac{1}{44}(\Psi_{i+1,j+1}+\Psi_{i-1,j+1}+\Psi_{i-1,j-1}+\Psi_{i+1,j-1}) \\
& -\frac{7}{66}h(\Psi_{x_{i+1,j}}-\Psi_{x_{i-1,j}}+\Psi_{y_{i,j+1}}-\Psi_{y_{i,j-1}}) \\
& -\frac{1}{264}h(\Psi_{x_{i+1,j+1}}-\Psi_{x_{i-1,j+1}}-\Psi_{x_{i-1,j-1}}+\Psi_{x_{i+1,j-1}} \\
& -\Psi_{y_{i+1,j+1}}+\Psi_{y_{i-1,j+1}}-\Psi_{y_{i-1,j-1}}-\Psi_{y_{i+1,j-1}}) \\
& +\frac{h^4}{792}\left[11s_{i,j}+(s_{i+1,j}+s_{i,j+1}+s_{i-1,j}+s_{i,j-1})\right],
\end{aligned} \tag{A.3}$$

$$\begin{aligned}
h\Psi_{x_{i,j}} \;=\; & \frac{3}{5}(\Psi_{i+1,j}-\Psi_{i-1,j})+\frac{3}{40}(\Psi_{i+1,j+1}-\Psi_{i-1,j+1} \\
& -\Psi_{i-1,j-1}+\Psi_{i+1,j-1})-\frac{h}{5}(\Psi_{x_{i+1,j}}+\Psi_{x_{i-1,j}}) \\
& -\frac{h}{40}(\Psi_{x_{i+1,j+1}}+\Psi_{x_{i-1,j+1}}+\Psi_{x_{i-1,j-1}}+\Psi_{x_{i+1,j-1}} \\
& +\Psi_{y_{i+1,j+1}}-\Psi_{y_{i-1,j+1}}+\Psi_{y_{i-1,j-1}}-\Psi_{y_{i+1,j-1}}) \\
& +\frac{h^4}{240}(s_{i+1,j}-s_{i-1,j}),
\end{aligned} \tag{A.4}$$

$$
\begin{aligned}
h\Psi_{y_{i,j}} &= \frac{3}{5}(\Psi_{i,j+1} - \Psi_{i,j-1}) + \frac{3}{40}(\Psi_{i+1,j+1} + \Psi_{i-1,j+1} \\
&- \Psi_{i-1,j-1} - \Psi_{i+1,j-1}) - \frac{h}{5}(\Psi_{x_{i,j+1}} + \Psi_{x_{i,j-1}}) \\
&- \frac{h}{40}(\Psi_{y_{i+1,j+1}} + \Psi_{y_{i-1,j+1}} + \Psi_{y_{i-1,j-1}} + \Psi_{y_{i+1,j-1}} \\
&+ \Psi_{x_{i+1,j+1}} - \Psi_{x_{i-1,j+1}} + \Psi_{x_{i-1,j-1}} - \Psi_{x_{i+1,j-1}}) \\
&+ \frac{h^4}{240}(s_{i,j+1} - s_{i,j-1}),
\end{aligned}
\tag{A.5}
$$

respectively. Definitely, the advantage of the scheme is that all unknowns, Ψ, Ψ_x and

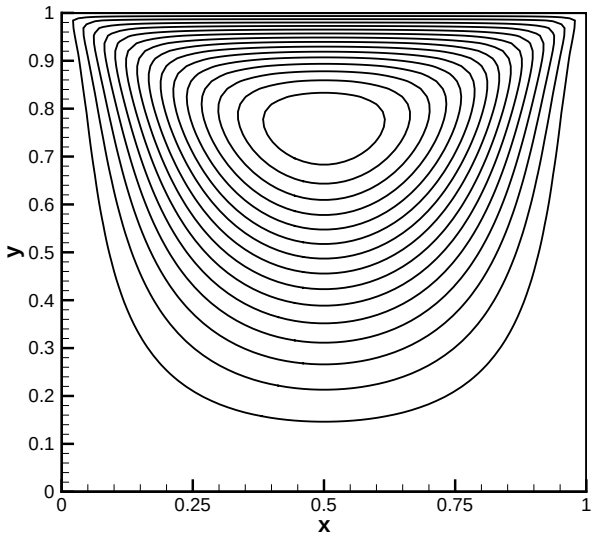

Figure A.1. Stokes flow in the square lid-driven cavity.

Ψ_y are coupled with each other and solving each equation gives directly the stream function; y and x-wise velocities, respectively.

The scheme has been tested for Stokes flow problem in a lid-driven cavity. Boundary conditions of Equation A.2 and Equations A.3 - A.5 are given as

$$\Psi(0,y) = \Psi(1,y) = \Psi(x,0) = \Psi(x,1) = 0$$

$$\Psi_x(0,y) = \Psi_x(1,y) = \Psi_x(x,0), \quad \Psi_x(x,1) = -1$$

According to Altas *et al.* (1998), Kelmanson's study of modified integral equation solution assigns the center of primary vortex with a value of $\Psi = 0.0998$ on $(0.5, 0.76)$. The code, developed for the current study, has been compared with referred values and close constitution was observed as seen Table A.1.

Additionally, graphical representation of the solution is illustrated in Figure A.1.

Table A.1. Comparison of main vortex values and locations.

	Stream function value	**Location of vortex**
Code results	0.10	$(0.5, 0.762)$
Kelmanson's results	0.0998	$(0.5, 0.760)$

APPENDIX B: DENSITY BOUNDARY CONDITIONS FOR THE SLIP FLOW REGIME

B.1. Theoretical Preliminaries

In most applications of fluid dynamics, the value of the density on a wall is treated by setting normal gradient of pressure equal to zero (see pages 204-206 of Ferziger *et al.*, (2002)) for no-slip conditions. However, in the slip flow regime, a suitable density condition should be derived. For this purpose, the following analysis of Poinsot *et al.* (1992) will be temporarily cheated. Let's consider a boundary located at $x = L$ as shown in Figure B.1. Borrowing the characteristic analysis of Thompson (1987) to

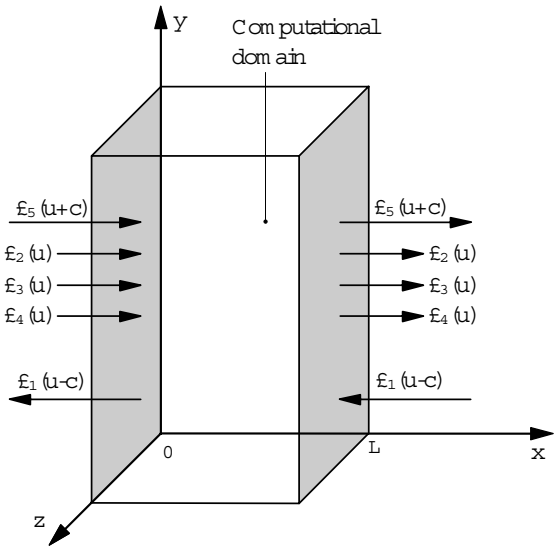

Figure B.1. Waves leaving and entering through an inlet plane ($x = 0$) and an outlet plane ($x = L$) for a subsonic flow (Poinsot *et al.*, 1992).

reorganize the convective (hyperbolic) terms corresponding to waves propagating in the x direction, the conservation equations are written in indicial notations
for continuity

$$\frac{\partial \rho}{\partial t} + d_1 + \frac{\partial m_2}{\partial y} + \frac{\partial m_3}{\partial z} = 0, \tag{B.1}$$

energy

$$\frac{\partial \rho E}{\partial t} + \frac{1}{2}\left(u_k u_k\right) d_1 + \frac{d_2}{\gamma - 1} + m_1 d_3 + m_2 d_4 + m_3 d_5$$
$$+ \frac{\partial\left[\left(\rho E + p\right) v\right]}{\partial y} + \frac{\partial\left[\left(\rho E + p\right) w\right]}{\partial z} = \frac{\partial\left(u_j \tau_{ij}\right)}{\partial x_i} - \frac{\partial q_i}{\partial x_i}, \tag{B.2}$$

x-momentum

$$\frac{\partial m_1}{\partial t} + u_1 d_1 + \rho d_3 + \frac{\left(m_1 u_2\right)}{\partial y} + \frac{\left(m_1 u_3\right)}{\partial z} = \frac{\partial \tau_{1j}}{\partial x_j} \tag{B.3}$$

y-momentum

$$\frac{\partial m_2}{\partial t} + u_2 d_1 + \rho d_4 + \frac{\left(m_2 u_2\right)}{\partial y} + \frac{\left(m_2 u_3\right)}{\partial z} = \frac{\partial \tau_{2j}}{\partial x_j} \tag{B.4}$$

and z-momentum equations

$$\frac{\partial m_3}{\partial t} + u_3 d_1 + \rho d_5 + \frac{\left(m_3 u_2\right)}{\partial y} + \frac{\left(m_3 u_3\right)}{\partial z} = \frac{\partial \tau_{3j}}{\partial x_j} \tag{B.5}$$

where $m_i = \rho u_i$ for $i = 1, 2, 3$ are being mass fluxes. The vector $\mathbf{d}$ is yielded from characteristic analysis of Thompson (1987) and given by

$$\mathbf{d} = \begin{bmatrix} d_1 \\ d_2 \\ d_3 \\ d_4 \\ d_5 \end{bmatrix} = \begin{bmatrix} \frac{1}{c^2}\left[\mathfrak{A}_2 + \frac{1}{2}\left(\mathfrak{A}_5 + \mathfrak{A}_1\right)\right] \\ \frac{1}{2}\left(\mathfrak{A}_5 + \mathfrak{A}_1\right) \\ \frac{1}{2\rho c}\left(\mathfrak{A}_5 - \mathfrak{A}_1\right) \\ \mathfrak{A}_3 \\ \mathfrak{A}_4 \end{bmatrix} = \begin{bmatrix} \frac{\partial m_1}{\partial x_1} \\ \frac{\partial\left(c^2 m_1\right)}{\partial x} + \left(1 - \gamma\right)\mu \frac{\partial p}{\partial x} \\ u\frac{\partial u}{\partial x} + \frac{1}{\rho}\frac{\partial p}{\partial x} \\ u\frac{\partial v}{\partial x} \\ u\frac{\partial w}{\partial x} \end{bmatrix} \tag{B.6}$$

where the $\mathfrak{A}_i$ for $i = 1 \cdots 5$ designate the amplitudes of characteristic waves with each corresponding characteristic velocity λ. These velocities follow as (Thompson, 1987)

$$\lambda_1 = u - c \tag{B.7}$$

$$\lambda_2 = \lambda_3 = \lambda_4 = u \tag{B.8}$$

$$\lambda_5 = u + c \tag{B.9}$$

where c denotes speed of sound and defined as $c = \sqrt{\gamma RT}$. Additionally, amplitudes of characteristic waves are estimated by Poinsot *et al.* (1992) and expressed as

$$\mathfrak{A}_1 = \lambda_1 \left(\frac{\partial p}{\partial x} - \rho c \frac{\partial u}{\partial x} \right), \tag{B.10}$$

$$\mathfrak{A}_2 = \lambda_2 \left(c^2 \frac{\partial \rho}{\partial x} - \frac{\partial p}{\partial x} \right), \tag{B.11}$$

$$\mathfrak{A}_3 = \lambda_3 \frac{\partial v}{\partial x}, \tag{B.12}$$

$$\mathfrak{A}_4 = \lambda_4 \frac{\partial w}{\partial x}, \tag{B.13}$$

$$\mathfrak{A}_5 = \lambda_5 \left(\frac{\partial p}{\partial x} + \rho c \frac{\partial u}{\partial x} \right). \tag{B.14}$$

In the next section, the density BC will be presented for the slip-flow regime.

B.2. Derivation of Density Boundary Conditions in the Slip Flow Regime

Boundary conditions of the density strictly, depend on the thermal status of the walls. As is mentioned earlier, two types of BCs have been enforced in the current study: Dirichlet and Neumann type BCs.

Let us consider the wall at $x = L$ that its temperature specified (Dirichlet BC,

$T(L, y, z, t) = f(y, z, t)$). The normal velocity at this wall will be zero ($u(L, y, z, t) = 0$). Once, we have assigned these conditions, the process follows as

`Stage 1.` Zero wall-normal velocity condition rearranges characteristic velocities such that

$$\lambda_1 = -c, \tag{B.15}$$

$$\lambda_2 = \lambda_3 = \lambda_4 = 0, \tag{B.16}$$

$$\lambda_5 = c. \tag{B.17}$$

`Stage 2.` Thus, the amplitudes of characteristic waves convert to

$$\mathfrak{A}_1 = \lambda_1 \left(\frac{\partial p}{\partial x} - \rho c \frac{\partial u}{\partial x} \right) = -c \left(\frac{\partial p}{\partial x} - \rho c \frac{\partial u}{\partial x} \right), \tag{B.18}$$

$$\mathfrak{A}_2 = \lambda_2 \left(c^2 \frac{\partial \rho}{\partial x} - \frac{\partial p}{\partial x} \right) = 0, \tag{B.19}$$

$$\mathfrak{A}_3 = \lambda_3 \frac{\partial v}{\partial x} = 0, \tag{B.20}$$

$$\mathfrak{A}_4 = \lambda_4 \frac{\partial w}{\partial x} = 0, \tag{B.21}$$

$$\mathfrak{A}_5 = \lambda_5 \left(\frac{\partial p}{\partial x} + \rho c \frac{\partial u}{\partial x} \right) = c \left(\frac{\partial p}{\partial x} + \rho c \frac{\partial u}{\partial x} \right). \tag{B.22}$$

`Stage 3.` Now, let's consider the continuity equation given by Equation B.1. The evaluation of continuity equation requires specification of d_1. From the definition of it, one can conclude from Equation B.19

$$d_1 = \frac{1}{c^2} \left[\mathfrak{A}_2 + \frac{1}{2} \left(\mathfrak{A}_5 + \mathfrak{A}_1 \right) \right] = \frac{1}{2c^2} \left(\mathfrak{A}_5 + \mathfrak{A}_1 \right). \tag{B.23}$$

`Stage 4.`The *Local One-Dimensional Inviscid (LODI)* relation of Thompson (1987)

(see referred article and page 110 of Poinsot *et al.* (1992) for more information) induces

$$\left.\frac{\partial u}{\partial t}\right|_{x=L} + \frac{1}{2\rho c}\left(\mathfrak{A}_5 - \mathfrak{A}_1\right) = 0 \quad \Rightarrow \quad \mathfrak{A}_1 = \mathfrak{A}_5. \tag{B.24}$$

`Stage 5.` Let's recast continuity equation by considering B.22, B.23 and B.24, which results in a suitable boundary condition for the density at $x = L$, such that

$$\frac{\partial \rho}{\partial t} + \frac{1}{c}\left[\frac{\partial p}{\partial x} + \rho c \frac{\partial u}{\partial x}\right] + \frac{\partial(\rho v)}{\partial y} = 0.$$

Newly derived density BC can be reorganized in a general form for two-dimension:

$$\frac{\partial \rho}{\partial \tau} + \frac{1}{c}\left[\frac{\partial p}{\partial n} + \rho c \frac{\partial u_n}{\partial n}\right] + \frac{\partial(\rho u_t)}{\partial t} = 0. \tag{B.25}$$

where τ stands for time only for this formula. Here u_n and u_t refer to the wall normal and the tangential velocity components as well.

Finding a density BC for insulated wall is quite simple by utilizing Equation B.25. Use of equation of state enables us to rewrite the mentioned equation such that the normal gradient of pressure splits into two parts

$$\frac{\partial \rho}{\partial \tau} + \frac{1}{c}\left\{c_v(\gamma - 1)\left[\rho \frac{\partial T}{\partial n} + T \frac{\partial \rho}{\partial n}\right] + \rho c \frac{\partial u_n}{\partial n}\right\} + \frac{\partial(\rho u_t)}{\partial t} = 0. \tag{B.26}$$

Well insulation condition across the wall requires setting the normal gradient of the temperature to zero, $\frac{\partial T}{\partial n} = 0$, and thus the density boundary condition for the adiabatic wall is reformed

$$\frac{\partial \rho}{\partial \tau} + \frac{1}{c}\left[c_v(\gamma - 1) T \frac{\partial \rho}{\partial n} + \rho c \frac{\partial u_n}{\partial n}\right] + \frac{\partial(\rho u_t)}{\partial t} = 0. \tag{B.27}$$

REFERENCES

Altas, I., Dym, J., Gupta, M.M., R.P. Manohar, 1998, "Multigrid Solution of Automatically Generated High-Order Discretizations for the Biharmonic Equation", *SIAM Journal on Scientific Computing*, Vol. 19, No. 5, pp. 1575-1585.

Aqarwal, R.K., Yun, K.Y. and R. Balakrishnan, October 2001,"Beyond Navier-Stokes: Burnet Equations for Flows in the Continuum-Transition Regime", *Physics of Fluids*, Vol. 13, No. 10, pp. 3061-3085.

Arkilic, E.B., Schmidt, M.A., and K.S. Breuer, June 1997, "Gaseous Slip Flow in Long Microchannels", *Journal of Microelectromechanical Systems*, Vol. 6, No. 2, pp. 167-178.

Ayon, A.A., Bayt, R.L. and K.S. Breuer, December 2001, "Deep reactive ion etching: a promising technology for micro- and nanosatellites", *Smart Materials and Structures*, Vol. 10, No. 6, pp. 75-108.

Batchelor, G.K, 1967,"An Introduction to Fluid Dynamics", Cambridge University Press,Cambridge.

Blazek, J., 2001,"Computational Fluid Dynamics: Principles and Applications", Elsevier Science Publishing, Oxford.

Chapman, S. and T.G. Cowling, 1970,"The Mathematical Theory of Nonuniform Gases", Cambridge University Press, Cambridge.

Chorin, A.J., 1967, "A numerical Method for Solving Incompressible Viscous Flow Problems", *Journal of Computational Physics*, Vol. 2, No. 1, pp. 12-26.

Kennedy C.A., Carpenter, M.H. and R.M. Lewis, 2000, "Low-Storage, Explicit RungeKutta Schemes for the Compressible NavierStokes Equations", *Applied Nu-*

merical Mathematics, Vol. 35, No. 3, pp. 177-219.

Colin, S., "Rarefaction and compressibility effects on steady and transient gas flows in microchannels", *Microfluidics and Nanofluidics*, Vol. 1, No. 3, pp. 268-279.

Collatz, L., 1966,"The Numerical Treatment of Differential Equations", Springer-Verlag, New York.

Coronell, D.G. and K.F. Jensen, September 1994, "Simulation of Rarefied Gas Transport and Profile Evolution in Nonplanar Substrate Chemical Vapor Deposition", *Journal of The Electrochemical Society*, Vol. 141, No. 9, pp. 2545-2551.

Deissler, R.G., 1964, "An Analysis of Second-Order Slip Flow and Temperature-Jump Boundary Conditions for Rarefied Gases", *International Journal of Heat and Mass Transfer*, Vol. 7, pp. 681-694.

Ding, Y. and M. Kawahara, 1999, "Three-Dimensional Linear Stability Analysis of Incompressible Viscous Flows Using the Finite Element Method", *International Journal for Numerical Methods in Fluids*, Vol. 31, No. 2, pp. 451-479.

Drazin, P.G. and W.H. Reid, 1993, "Hydrodynamic Stability", Cambridge University Press, Cambridge.

Ehrich, F.F. and S.A. Jacobson, 2003, "Development of High-Speed Gas Bearings for High Power Density Microdevices", *Journal of Engineering for Gas Turbines and Power*, Vol. 125, No. 1, pp. 141-148.

Georgescu, A., 1985,"Hydrodynamic Stability Theory", Martinus Nijhoff Publishers.

Ferziger, J.H. and M. Péric, 2002,"Computational Methods for Fluid Dynamics", Springer, 3rd Edition.

Gad-el-Hak, M., March 1999, "The Fluid Mechanics of Microdevices - The Freeman Scholar Lecture", *Journal of Fluids Engineering*, Vol. 121, No. 1, pp. 5-33.

Golshtein, E. and T. Elperin, April-June 1996, "Convective Instabilities in Rarefied Gases by Direct Simulation Monte Carlo", *Journal of Thermophysics and Heat Transfer*, Vol. 10, No. 2, pp. 250-256.

Gupta, M.M. and R.P. Manohar, 1979, "Direct Solution of the Biharmonic Equation Using Noncoupled Approach", *Journal of Computational Physics*, Vol. 33, No. 2, pp. 236-248.

Gupta, M.M. and R.P. Manohar, 1979, "Boundary Approximation and Accuracy in Viscous Flow Computations", *Journal of Computational Physics*, Vol. 31, No. 2, pp. 265-288.

Hirano, H., Seo, M. and H. Ozoe, 2002, "Two-Dimensional Numerical Computation for RayleighBénard Convection with Both the NavierStokes Equation and the Boltzmann Equation", *Modelling and Simulation in Materials Science and Engineering*, Vol. 10, No. 6, pp. 765-780.

Hobson, J.P. and D.B. Salzman, 2000, "Review of Pumping by Thermal Molecular Pressure", *Journal of Vacuum Science and Technology A*, Vol. 18, No. 4, pp. 1758-1765.

Hu, S., and X.L. Zhong, March 1998, "Linear Stability of Viscous Supersonic Plane Couette Flow", *Physics of Fluids*, Vol. 10, No. 3, pp. 709-729.

Ikegawa, M., and J. Kobayashi, October 1989, "Deposition Profile Simulation Using the Direct Simulation Monte Carlo Method ", *Journal of The Electrochemical Society*, Vol. 136, No. 10, pp. 2982-2986.

Jameson, A., Schmidt, W. and E. Turkel, 1981, "Numerical Solutions of the Euler Equations by Finite Volume Methods Using Runge-Kutta Time-Stepping Schemes", *AIAA Paper*, 81-1259.

Jameson, A., 2001, "A Perspective on Computational Algorithms for Aerodynamic

Analysis and Design", *Progress in Aerospace Sciences*, Vol. 37, No. 2, pp. 197-243.

Jameson, A., 2001, "Analysis and design of numerical schemes for gas dynamics .2. Artificial diffusion and discrete shock structure", *International Journal of Computational Fluid Dynamics*, Vol. 5, No. 1-2, pp. 1-38.

Kallinderis, Y., and H.T. Ahn, 2005, "Incompressible NavierStokes Method with General Hybrid Meshes", *Journal of Computational Physics*, Vol. 210, No. 1, pp. 75-108.

Karniadakis, E.K. and A. Beskok, 2002, "Micro Flows Fundamentals and Simulation", Springer Verlag.

Khorrami, M.R., Malik, M.R. and R.L. Ash, 1989, "Application of Spectral Collocation Techniques to the Stability of Swirling Flows", *Journal of Computational Physics*, Vol. 81, No. 1, pp. 206-229.

Kennard, E.H., 1938, "Kinetic Theory of Gases With an Introduction to Statistical Mechanics", McGraw-Hill Book

Lee, C.J., 1994, "Unique Determination of Solutions to the Burnett Equations", *AIAA Journal*, Vol. 32, No. 5, pp. 985-990.

Lele, S.K., 1992, "Compact Finite Difference Schemes with Spectral-like Resolution", *Journal of Computational Physics*, Vol. 103, No. 1, pp. 16-42.

Mackowski, D.W., Papadopoulos D.H. and D.E. Rosner, 1999, "Comparison of Burnett and DSMC Predictions of Pressure Distributions and Normal Stress in One-Dimensional, Strongly Nonisothermal Gases", *Physics of Fluids*, Vol. 11, No. 8, pp. 2108-2116.

Malik, M.R., 1982, "Accurate Numerical Solution of Compressible, Linear Stability Equations", *Journal of Applied Mathematics and Physics (ZAMP)*, Vol. 33, No. 2, pp. 189-201.

Manela, A., and I. Frankel, 2005, "On the RayleighBnard problem in the Continuum Limit", *Physics of Fluids*, Vol. 17, No. 3, pp. 036101.1-036101.7.

Malik, M.R., 1990, "Numerical Methods for Hypersonic Boundary Layer Stability", *Journal of Computational Physics*, Vol. 86, No. 2, pp. 376-413.

Maxwell, J.C., 1878, "On Stresses in Rarefied Gases Arising from Inequalities of Temperature", *Proceedings of the Royal Society of London*, Vol. 27, pp. 304-308.

Moler, C.B., and G.W. Stewart, April 1973, "An Algorithm for Generalized Matrix Eigenvalue Problems", *SIAM Journal on Numerical Analysis*, Vol. 10, No. 2, pp. 241-256.

Nayfeh A.H., 1993,"Introduction to Perturbation Techniques", John Wiley & Sons.

Pan, P., Kubby, J., Peeters, E., Tran, A.T. and S. Mukherjee, September 1998, "Squeeze film damping effect on the dynamic response of a MEMS torsion mirror", *Journal of Micromechanics and Microengineering*, Vol. 8, No. 3, pp. 200-208.

Papadopoulos, D.H. and D.E. Rosner, November 1995, "Enclosure Gas Flows Driven by Nonisothermal Walls", *Physics of Fluids*, Vol. 7, No. 11, pp. 2535-2537.

Peyret, R., 1976, "Unsteady Evolution of a Horizontal Jet in a Stratified Fluid,", *Journal of Fluid Mechanics*, Vol. 78, pp. 49-63.

Poinsot, T.J. and S.K. Lele, 1992, "Boundary Conditions for Direct Simulations of Compressible Viscous Flows", *Journal of Computational Physics*, Vol. 101, No 1, pp. 104-129.

Present, R.D., 1958,"Kinetic Theory of Gases", McGraw-Hill Book, New York.

Priede, J. and G. Gerbeth, June 1997, "Influence of Thermal Boundary Conditions on the Stability of Thermocapillary-Driven Convection at Low Prandtl Numbers", *Physics of Fluids*, Vol. 9, No. 6, pp. 1621-1634.

Rahman, M.M. and T. Siikonen, 2001, "An Artificial Compressibility Method for Incompressible Flows", *Numerical Heat Transfer, Part B-Fundamentels*, Vol. 40, pp. 391-409.

Rogers, S.E. and D. Kwak, 1990, "Upwind Differencing Scheme for the Time Accurate Incompressible Navier Stokes Equations", *AIAA Journal*, Vol. 28, No. 2, pp. 253-262.

Rogers, S.E., Kwak, D. and C. Kiris, 1991, "Steady and Unsteady Solutions of the Incompressible Navier Stokes Equations", *AIAA Journal*, Vol. 29, No. 4, pp. 603-610.

Scott, M.R., and H.A. Watts, March 1977, "Computational Solution of Linear 2-Point Boundary Value Problems via Orthonormalization", *SIAM Journal on Numerical Analysis*, Vol. 14, No. 1, pp. 40-70.

Setina, J., 1999, "New Approach to Corrections for Thermal Transpiration Effects in Capacitance Diaphragm Gauges", *Metrologia*, Vol. 36, No. 6, pp. 623-626.

Sone, Y., Aoki, K. and H. Sugimoto, December 1997, "The Bénard Problem for a Rarefied Gas: Formation of Steady Flow Patterns and Stability of Array of Rolls", *Physics of Fluids*, Vol. 9, No.12, pp. 3898-3914.

Sone, Y., "Flow Induced by Temperature Fields in a Rarefied Gas and Their Ghost Effect on the Behavior of a Gas in the Continuum Limit", *Annual Review of Fluid Mechanics*, Vol. 32, pp.779-811.

Sone, Y., and T. Doi, June 2003, "Bifurcation of and Ghost Effect on the Temperature Field in the Bénard Problem of a Gas in the Continuum Limit", *Physics of Fluids*, Vol. 15, No. 6, pp. 1405-1423.

Stefanov, S., Roussinov, V. and C. Cercignani, July 2002, "Rayleigh-Bénard Flow of a Rarefied gas and It's Attractors. I. Convection Regime", *Physics of Fluids*, Vol.

14, No. 7, pp. 2255-2269.

Stefanov, S., Roussinov, V., and C. Cercignani, 2002, "Rayleigh-Bénard Flow of a Rarefied Gas and Its Attractors. II. Chaotic and Periodic Convective Regimes", *Physics of Fluids*, Vol. 14, No. 7, pp. 2270-2288.

Stephenson, J.W., 1984, "Single Cell Discretizations of Order Two and Four for Biharmonic Problems", *Journal of Computational Physics*, Vol. 55, No. 1, pp. 65-80.

Stoer, J. and R. Bulirsch 1992,"Introduction to Numerical Analysis", Springer Verlag, New York.

Tannehill J.C., Anderson, D.A. and R.H. Pletcher 1997,"Computational Fluid Mechanics and Heat Transfer", Taylor& Francis.

Teasdale, D., Milanovic, V., Chang, P. and K.S.J. Pister, 2001, "Microrockets for Smart Dust", *Smart Materials and Structures*, Vol. 10, No. 6, pp. 1145-1155.

Thompson, K.W., 1987, "Time Dependent Boundary Conditions for Hyperbolic Systems", *Journal of Computational Physics*, Vol. 68, No. 1, pp. 1-24.

Wesseling, P., 2001,"Principles of Computational Fluid Dynamics ", Springer Verlag.

White, F.M., 2005,"Viscous Fluid Flow", McGraw-Hill Book, New York.

Williamson, J.H., 1980, "Low-Storage Runge-Kutta Schemes", *Journal of Computational Physics*, Vol. 35, No. 1, pp. 48-56.

Wilkinson, J.H., 1965,"The algebraic eigenvalue problem ", Clarendon Press, London.

Van Dyke M., 1964,"Perturbation Methods in Fluid Mechanics", Academic Press.

Vargo, S.E., Muntz, E.P., Shiflett, GR., and W.C. Tang, July-August 1999, "Knudsen Compressor as a Micro- and Macroscale Vacuum Pump without Moving Parts

or Fluids", *Journal of Vacuum Science and Technology A-Vacuum Surfaces and Films*, Vol. 17, No. 4, pp. 2308-2313.

Veijola, T. and M. Turowski, June 2001, "Compact Damping Models for Laterally Moving Moving Microstructures with Gas-Rarefaction Effects", *Journal of Micro-electromechanical Systems*, Vol. 10, No. 2, pp. 263-273.

Vincenti W.G. and C.H. Kruger, 1965,"Introduction to Physical Gas Dynamics", John Wiley & Sons.